

Geochemical Reactions in Unsaturated Mine Wastes

Jeanette K. Jerz

Dissertation submitted to the Faculty of the Virginia Polytechnic Institute and State University in partial fulfillment of the requirements for the degree of

*Doctor of Philosophy
in
Geological Sciences*

Committee in charge:
J. Donald Rimstidt, Chair
James R. Craig
W. Lee Daniels
Patricia Dove
D. Kirk Nordstrom

*April 22, 2002
Blacksburg, Virginia*

Keywords: Acid Mine Drainage, Pyrite, Oxidation Rate, Efflorescent Sulfate Salt, Paragenesis,

Copyright 2002, Jeanette K. Jerz

GEOCHEMICAL REACTIONS IN UNSATURATED MINE WASTES

JEANETTE K. JERZ

ABSTRACT

Although mining is essential to life in our modern society, it generates huge amounts of waste that can lead to acid mine drainage (AMD). Most of these mine wastes occur as large piles that are open to the atmosphere so that air and water vapor can circulate through them. This study addresses the reactions and transformations of the minerals that occur in humid air in the pore spaces in the waste piles.

The rate of pyrite oxidation in moist air was determined by measuring over time the change in pressure between a sealed chamber containing pyrite plus oxygen and a control. The experiments carried out at 25°C, 96.8% fixed relative humidity, and oxygen partial pressures of 0.21, 0.61, and 1.00 showed that the rate of oxygen consumption is a function of oxygen partial pressure and time. The rates of oxygen consumption fit the expression

$$\frac{dn_{O_2}}{dt} = 10^{-6.48} P_{O_2}^{0.5} t^{-0.5}.$$

It appears that the rate slows with time because a thin layer of ferrous sulfate + sulfuric acid solution grows on pyrite and retards oxygen transport to the pyrite surface.

The transformation of efflorescent sulfate minerals (the reaction products of iron sulfide oxidation) from a pyrrhotite-rich massive sulfide is explained using a systematic analysis of their stoichiometry and thermodynamics. Their stabilities are controlled by oxygen partial pressure, relative humidity, and activity of sulfuric acid and can be visualized using $\log a_{O_2} - \log a_{H_2O}$ and $\log a_{H_2SO_4} - \log a_{H_2O}$ diagrams developed during this study.

Samples from the field site were analyzed in the laboratory to determine mineralogy, equilibrium relative humidity, chemical composition, and acid generation potential. Dissolution experiments showed that fibroferrite-rich samples had the highest acid producing potential, followed by copiapite-rich samples and then halotrichite-rich samples. The most abundant metals in solutions produced by dissolving the salts were magnesium, aluminum, zinc, copper, calcium, and lead. The molar concentrations of the metals varied with mineralogy. However, all of these minerals release metals and acid when they dissolve and therefore represent a significant environmental threat.

*“All Things are Poisonous and yet there is Nothing that is Poisonous;
it is only the Dose that makes a Thing Poisonous”*

--P.A. Paracelsus

GRANT INFORMATION

This project was made possible by funding from the following:

- The National Science Foundation (Grant EAR-0003364)
- The Waste Policy Institute
- The Department of Geological Sciences
- The David Wones Geologic Scholarship Fund
- The Graduate Student Assembly

ACKNOWLEDGEMENTS

First and foremost, I would like to thank my advisor, Don Rimstidt, for his assistance, advice, and support during my Ph.D. Don has always been available to help me, not only with this project, but also with all other areas of my profession development. I will always be indebted to him for the time and attention he has given me. I would like also like to thank the other members of my committee: James Craig, Lee Daniels, Patricia Dove, and Kirk Nordstrom. Over the years, all of my committee members have provided me a great deal of technical assistance, scientific perspective, and personal guidance. I feel truly fortunate to have such a contributive and invaluable committee.

In addition, I would like to thank several people who helped me with this project:

- Dan Smith for building the Barcroft apparatus and stand and for generally contributing his skills and knowledge;
- Heather Shannon for help in the field and lab, especially with the sulfate mineral relative humidity and acid production experiments;
- Jane Hammarstrom and Nadine Piatak (USGS) and Ross Angel (VT) for help with identifying the sulfate minerals;
- Rob Weaver for his time and microscopy skills;
- Treavor Kendall and Steven Lower for analyzing my samples for bacteria and general discussions of microbes;
- All the present and past faculty and graduate students of the Geochemistry Research Group (Don, Mike, Chris, Trish, Nancy, Ross, Maddy, John, Russ, Kevin, Jody, Barry, Eric, Steven, Rob, Erin, Treavor, Tracy, Stacy, Jackson, Andy, Collin, Kevin, Brenda, Mariano, and Darren), who have provided great amounts of scientific discourse and generally support during my tenure at Virginia Tech.

I would also like to thank the faculty and staff of the Department of Geological Science at Virginia Tech for providing me with an excellent education and an opportunity to pursue my professional goals. Specifically, I am grateful to Cahit Coruh for his vision and leadership of the department while I was here. Also, I appreciate Linda Bland, Mary McMurry, Connie Lowe, Carolyn Williams for always being available and helpful and for making everything go as smoothly as possible.

Finally I would like to thank my friends and family who have loved and supported me through out this project. Specifically, I would like to thank my Mom, Dad, brother Jim, and Jason; without them this never would have happened.

TABLE OF CONTENTS

Abstract	ii
Grant Information	v
Acknowledgements.....	vi
Table of Contents.....	viii
List of Figures.....	x
List of Tables.....	xi
Chapter 1 : Introduction	1
Chapter 2 : Pyrite oxidation in moist air	1
Abstract	1
Introduction	2
Materials and Methods.....	5
Reactor Design.....	6
Experimental Procedure	9
Rate calculation.....	12
Results	14
Discussion	14
Data analysis.....	19
Comparison with other rates.....	27
Application of data.....	27
Conclusions	31
Acknowledgements.....	32
References	32
Appendix 1: Data from all Successful Experiments.....	38
Appendix 2: Pitzer Equations.....	43
Chapter 3 : Efflorescent iron sulfate minerals:	
Paragenesis, relative stability, and environmental impact.....	46
Abstract	46
Introduction	47
Name and Abbreviation	49
Methods.....	54
Field Methods	54
Laboratory Methods.....	58

Buffered Relative Humidity	60
Results	64
Field Observations	64
Mineralogy	67
Relative humidity data	67
Dissolution of minerals	68
Discussion	72
Paragenesis of Sulfate Phases	72
Log a_{O_2} -log $a_{\text{H}_2\text{O}}$ Diagram	75
Field Reaction Path	87
Water Quality Effects.....	88
Conclusions	89
Acknowledgements.....	90
References	90
Appendix 3 Data from the dissolution experiments	94

LIST OF FIGURES

Figure 2-1. Modified Barcroft apparatus used in pyrite oxidation experiments..	7
Figure 2-2. Diagram of reaction and control chamber assembly.	10
Figure 2-3. Data from experiment PY 43 plotted against the square root of time.	13
Figure 2-4. Oxygen consumption graphs from all experiments.	15
Figure 2-5. Rate graphs from all experiments.	16
Figure 2-6. FESEM image of pyrite surface after oxidation in humid air.	17
Figure 2-7. Normal distribution of the rate constant	21
Figure 2-8. Comparison of the rate in air and aqueous oxidation rate	24
Figure 2-9. Physical model of pyrite oxidation in humid air.	26
Figure 2-10. Data and modeled rate	28
Figure 2-11. Change in water activity with increasing ferrous sulfate + sulfuric acid solution.	30
Figure 3-1. The stoichiometry of iron sulfate and iron oxide minerals.	52
Figure 3-2. Hydrograph of Contrary Creek, VA	53
Figure 3-3. Location of the Gossan Lead in Southwestern Virginia.	55
Figure 3-4. Map of a portion of the Bambarger-Iron King mines	57
Figure 3-5. Schematic of humidity buffer method.	62
Figure 3-6. Example of the data collected with the humidity buffer method.	63
Figure 3-7. Large pile of predominantly sulfate minerals from field site.	66
Figure 3-8. Results from humidity buffer method.	69
Figure 3-9. Acid production potential of samples.	70
Figure 3-10. Metal composition of samples.	71
Figure 3-11. Physical setting and paragenetic sequence of field site.	73
Figure 3-12. Log a_{O_2} -log $a_{\text{H}_2\text{O}}$ diagram.	76
Figure 3-13. Log $a_{\text{H}_2\text{SO}_4}$ -log $a_{\text{H}_2\text{O}}$ diagram.	85

LIST OF TABLES

Table 2-1. Atmospheric oxidation rate of pyrite in humid air reported by other authors.....	4
Table 3-1. AMD minerals that occur in the system Fe-S-O-H	49
Table 3-2. Observed paragenesis of sulfate minerals	51
Table 3-3. Salts used to make saturated solution for humidity buffer method.	60
Table 3-4. Description of the minerals found at the Bumbarger-Iron King mine.....	67
Table 3-5. Chemical reactions and equations for Figures 12 & 13.	77
Table 3-6. Osmotic and mean activity coefficients for ferrous sulfate solutions.....	79
Table 3-7. The activity of oxygen and activity of water in ferrous sulfate solutions.....	80

Chapter 1 : INTRODUCTION

“If it can't be grown it must be mined”--Anonymous

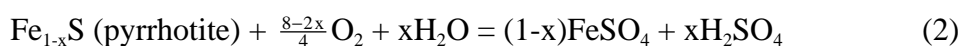
Essentially all of the resources that we use in modern society come from the earth, either from agriculture, hydrogeological, or geological sources. Since the industrial revolution, there has been an increasing demand on the earth's finite resources by the growing population. Associated with the increase in resource production is a large increase in the amount of wastes that are generated. These wastes are problematic because their disposal is costly and frequently the wastes are toxic to humans or other organisms. Agriculture produces the largest amount of waste, but almost all of that material is biodegradable and is recycled back to the soil in one way or another. Mining, on the other hand, produces large amounts of wastes that are not recycled and are frequently difficult to reclaim.

The U.S. Bureau of Mines (Anon, 1994) and U.S. Geological Survey (Moore, 2000) estimate that there are approximately 60 billion tons of mine wastes in the United States from the production of non-fuel resources, and more is produced at a rate of approximately 1.9 billion tons per year. Coal production also produces mine waste, but there are no current estimates on the tonnage generated. Significant quantities of these wastes contain sulfide minerals that react with oxygen and water to generate acid mine drainage (AMD).

Several studies have estimated the environmental and financial impact of AMD in the United States. Kim et al. (1982) estimate that more than 7,000 kilometers of streams in the eastern U.S. are affected by acid drainage from coal mines. The U.S. Forest Service estimates that 20,000 to 50,000 mines on Forest Service lands are releasing acidic drainage to between 8,000 and 16,000 kilometers of streams (U.S. Forest Service, 1993). The U.S. Water Reports (Anon., 1993) has estimated that the remediation of abandoned mines in the U.S. will cost a total of \$71 billion.

Most of these mine wastes occur as large piles that are open to the atmosphere. In this setting, air and water readily permeate them to create an enormous environment where minerals react with humid air in the pore spaces of waste pile. This study addresses these mineral-water vapor reactions and their accompanying transformation.

In waste piles, the oxidation of iron-bearing sulfides, primarily pyrrhotite, pyrite, and marcasite, creates ferrous sulfate and sulfuric acid by the overall reactions:



These reactions comprise the first steps in the complex, overall AMD-generating process. In some cases, their rates limit the overall amount of AMD production, so knowing the rates of these oxidative reactions is important. The next step in the AMD process is the transformation of the ferrous sulfate to mixed ferrous-ferric sulfate. Eventually the ferric iron hydrolyzes and precipitates as iron hydroxide phases leaving a solution that is further enriched in sulfuric acid. Much of the ferrous to ferric iron transformation occurs in the waste piles, either in solution films on mineral grains or in iron sulfate minerals. The iron sulfate minerals that occur in the wastes are reservoirs for sulfuric acid, soluble iron and aluminum (latent acidity), and for trace elements. These soluble salts are often rapidly released to nearby receiving waters during rain events, causing significant shifts in water positions, which can sicken and kill aquatic biota. The extent of this effect depends on which sulfate mineral phases are present in the waste pile, their acid-generating potential, and their trace element contents.

The second chapter of this dissertation addresses the rate of pyrite oxidation in humid air. A new reactor was designed and built to measure pressure mineral oxidation rates in air as a function of oxygen partial pressure, relative humidity, and temperature. In this study the reactor was used to determine pressure differences between a chamber containing pyrite in contact with air of a fixed humidity (96.8%) and known oxygen partial pressure and a control chamber with

the same internal volume. As pyrite consumed oxygen (equation 1), the partial pressure of the oxygen inside the chamber containing pyrite decreased relative to the control chamber. Pressure readings were collected over periods of days to weeks and converted to moles of oxygen consumed by means of a calibration factor. These data were analyzed to generate a rate law for the consumption of oxygen by pyrite in humid air as a function of oxygen pressure and time.

The third chapter analyzes the transformation of the iron sulfate minerals, which are the reaction products of the iron sulfide oxidation reactions (equations 1 and 2). This is the first study of the paragenesis of efflorescent sulfate minerals from a pyrrhotite dominant system where the mineral transformations are explained using a systematic approach to stoichiometry and thermodynamics. The stability of these minerals is explained in terms of oxygen partial pressure, relative humidity, and activity of sulfuric acid. In addition, dissolution experiments were used to determine the relative contribution of acidity and metals that can be expected from assemblages of selected sulfate minerals during rain events.

REFERENCES

- Anon. (1993) With or without reform, mining cleanup could cost \$71 billion. *U.S. Water News*. 10.
- Anon. (1994) *Minerals Today*, U.S. DOI, Bureau of Mines, p. 9.
- Kim, A.G., B. Heisey, R. Kleinmann, and M. Duel (1982) *Acid Mine Drainage: Control and Abatement Research*. U.S. DOI, Bureau of Mines IC 8905,.22.
- Moore, J. K. (2000) Mineral Industrial Surveys Mining and Quarring Trends 1998 Annual Review. U.S. Geological Survey
- USDA Forest Service (1993) Acid Mine Drainage From Mines on the National Forests, A Management Challenge. Program Aid 1505, 12.

Chapter 2: PYRITE OXIDATION IN MOIST AIR

ABSTRACT

The rate of pyrite oxidation in moist air was determined by measuring over time the change in pressure between a sealed chamber containing pyrite plus oxygen and a control. The experiments carried out at 25°C, 96.8% fixed relative humidity, and oxygen partial pressures of 0.21, 0.61, and 1.00 showed that the rate of oxygen consumption is a function of oxygen partial pressure and time. The rates of oxygen consumption fit the expression

$$\frac{dn_{O_2}}{dt} = 10^{-6.48} P_{O_2}^{0.5} t^{-0.5}.$$

It appears that the rate slows with time because a thin layer of ferrous sulfate + sulfuric acid solution grows on pyrite and retards oxygen transport to the pyrite surface.

At very short reaction times, the rate of pyrite oxidation in air is slightly faster than the aqueous oxidation rate at the same oxygen partial pressure and temperature. At greater extents of reaction, the rate slows significantly and approaches the rates reported by humidity cell studies. This slower rate of oxidation in air appears to be more appropriate than the aqueous oxidation rate for modeling pyrite oxidation in unsaturated waste piles.

At relative humidities less than 95%, a solid ferrous sulfate phase (melanterite or szolmonokite) becomes saturated and will precipitate from the ferrous sulfate + sulfuric acid solution in cracks and on the reacting surface. These solids have the potential to wedge apart the sample leading to physical disaggregation of the pyrite as is often seen in museum samples.

Notation used in this paper

Symbol	Definition, units
t	Time, sec
n	Oxygen consumed, mol
A	Surface area, m ²
r	Rate of oxygen consumption, $\frac{1}{A} \frac{dn}{dt}$, mol/m ² sec
k	Rate constant, units vary depending on the rate expression
J	Flux of oxygen through film, mol/m ² sec
C_a	Concentration of oxygen at the solution/air interface, mol/m ³
C_p	Concentration of oxygen at the pyrite/solution interface, mol/m ³
K_H'	Apparent Henry's law constant, mol/m ³ atm
P	Oxygen partial pressure, atm
P_a	Partial pressure of oxygen at the solution/air interface, atm
P_p	Partial pressure of oxygen at the pyrite/solution interface, atm
L	Layer thickness of ferrous sulfate + sulfuric acid solution, m
k_l	Layer thickness constant, m/mol
D	Diffusion constant for oxygen in film, m ² /sec

INTRODUCTION

The oxidation of pyrite at or near the earth's surface creates acidic drainage that can have a serious, negative impact on the biota and water quality in nearby receiving waters (Smith and Huyck, 1999; Kelly, 1999). For this reason, much effort has gone into studying pyrite oxidation in order to understand the chemistry of the process with the goal of reducing its impact. Plumlee and Logsdon (1999) have presented an excellent recent review of the chemical, physical, and biological processes involved in acid mine drainage.

There have been several studies of the rate of pyrite oxidation under subaqueous conditions (Williamson and Rimstidt, 1994 and references within). However, pyrite exists frequently in unsaturated waste piles where it oxidizes subaerially. Ritchie, (1994), Elberling et al.(1994); Elberling and Nicholson (1996) developed models that consider the air oxidation of pyrite in waste piles where they conclude that the rates are limited by oxygen diffusion through

the wastes. We have developed a method of measuring the rate of pyrite oxidation in humid air as a function of oxygen partial pressure that allows a quantitative determination of the rate of the chemical reaction that occurs at the pyrite surface.

Anecdotal evidence for significant rates of pyrite oxidation in humid air comes from museum curators who have found that pyrite samples often crumble to fragments during storage (Howie, 1992). Curators, concerned with the preservation of their samples, refer to this process as “pyrite disease,” and great care is taken to minimize the damaging effects. This includes keeping the samples in low humidity environments, coating the samples with clear resins that act as protective barriers to oxygen and water, and removing the products of oxidation (Bannister, 1933; Bannister, 1937). While these efforts may be cost effective for rare and expensive museum samples, they are impractical at a field scale, where pyrite grains in waste piles oxidize in a similar manner to untreated museum samples.

The few studies that have determine the rates of pyrite oxidation are listed in Table 1. Morth and Smith (1966) published the results of Birle (1963) and Kim (1964) who used Warburg manometry, described by Umbreit et al. (1972) to study the rate of oxygen consumption due to pyrite oxidation in vapor as a function of relative humidity, oxygen pressure, and temperature. They report a constant rate over long time periods (several days to weeks). At 25°C and 96% relative humidity, this rate is $10^{-7.23}$ (mol O₂/m²sec) in 100% oxygen and $10^{-7.66}$ (mol O₂/m²sec) in air (21% oxygen). Morth and Smith (1966) found “significantly faster rates when pyrite oxidizes in air as compared to solution.” Based on their results, they concluded that the reaction order of oxygen was fractional and the rate-limiting step of pyrite oxidation was the physical adsorption of dissociated oxygen on the surface of pyrite. We are unaware of any other study in which the authors directly measured oxygen consumption and controlled humidity.

Other studies of pyrite oxidation in air have used humidity cells. Note that humidity cell experiments, which use flooded then drained columns of pyritic material to determine the rate of

pyrite oxidation in air, probably measure a mixed rate that includes pyrite oxidation in air, pyrite oxidation in solution, and transport of oxygen. This method first calls for the saturation of the sample with water, which is later drained, to create a partially saturated mass with a humid environment. It is likely that liquid water is still present in the pore spaces between the grains and as a coating on the grains' surfaces. Although oxygen partial pressure and temperature can be controlled in these experiments, relative humidity is not. The interpretation of the rate data is difficult because the activity of water is variable over the course of an experiment. Although the rates generated by the Morth and Smith (1966) and those from humidity cells can not be compared directly, they provide useful insight for comparison to of our results. The rates reported by humidity cell studies range between $10^{-6.5}$ and $10^{-8.7}$ mol O₂/m²sec (Table 1).

Table 2-1. Atmospheric oxidation rate of pyrite in humid air reported by other authors (recalculated from Hammack and Watzlaf (1990)). Morth and Smith (1966) directly measured oxygen consumption rates to measure the rate of pyrite oxidation, other authors used humidity cells and monitored sulfate production to determine the rate of pyrite oxidation

Study	Rate (mol O₂/m²sec)	T	O₂ Dependence	Species Monitored
Morth and Smith (1966)*	10 ^{-7.7} in air 10 ^{-7.2} in 100% O ₂	25	Fractional order	Oxygen
Brayley (1960)	10 ^{-6.5}	N/A	1 st order	Sulfate
Rogowski and Pionke (1984)	10 ^{-7.4}	25	Not determined	Sulfate
Nicholson et al. (1988)	10 ^{-8.7}	23	Fractional	Sulfate
Hammack & Watzlaf (1990)	10 ^{-5.7} surface rate (XPS) 10 ^{-8.7} bulk rate	25	0 order >10% 1 st order > 5%	Sulfate

*Includes two unpublished M.S. theses (Birle, 1963 and Kim, 1964)

Borek (1994) investigated pyrite oxidation in the vapor phase using both hydrothermal and sedimentary pyrite samples, but did not report a rate law. This study provides helpful information about the products generated by pyrite oxidation in humid air. Borek (1994) found

that liquid water condensed on certain types of pyrite at relative humidities greater than 70%. In addition, ferrous sulfate salts ($\text{FeSO}_4 \cdot n\text{H}_2\text{O}$; $n = 7$ for melanterite; $n = 4$ for rozenite; $n = 1$ for szomolnokite) and hematite were detected using Mössbauer spectroscopy as reaction products on pyrite samples that had oxidized under a range of relative humidities (34% - 79%). The type of and amount of reaction product varied with pyrite source, although both hydrothermal and sedimentary pyrites were found to oxidize in the study. The Borek's results are consistent with the idea that pyrite oxidizes and produces ferrous sulfate and sulfuric acid in air by the same reaction that is used to describe the aqueous process:



The purpose of this paper is to determine the rate of pyrite oxidation in humid air as a function of oxygen partial pressure. The findings of this study will link those studies that investigate very short extents of pyrite reaction, generated by X-ray photon spectroscopy (XPS) studies (Nesbitt and Muir, 1994; Knipe et al., 1995; Nesbitt et al., 1998; Guevremont et al., 1998a; Guevremont et al., 1998b; Elsetinow et al., 2000; Nesbitt et al., 2000), and those using longer term humidity cell studies.

MATERIALS AND METHODS

Coarse-grained pyrite from Peru was used in all experiments. The pyrite was crushed and sieved to recover the 40-60 mesh size. Foust et al. (1980) provides a graph that shows the relationship between surface area and grain size, which we used to estimate that the surface area of pyrite in each experiment was 0.051 m^2 . The pyrite was washed with ethyl alcohol 3-5 times until the supernatant was clear. The samples were then sonicated in ethyl alcohol to removed adhering fine particles and dismember any bacteria. This procedure was repeated at least three times until the supernatant was clear. The grains were dried at 70°C for 12 hours. This method of sample preparation produced predominantly freshly fractured surfaces, similar to those found in tailings. After cleaning, 5.1 g aliquots of pyrite were placed in glass ampoules that were

evacuated and sealed. The pyrite was stored at room temperature in the evacuated ampoules until use.

Reactor Design

The rate of oxygen consumption by a pyrite sample was measured using a modified Barcroft apparatus. Barcroft manometry has been used extensively by biologists to determine respiration rates (Umbreit et al., 1972). The design of our modified system is shown in Figure 1. The apparatus consists of two chambers joined by a manometer. The chambers are sealed during an experiment and the pressure change in one chamber relative to the other is documented by a change in oil height in the arms of the manometer. The reaction chamber (right) holds the pyrite and the control chamber containing quartz (left) is used as a pressure reference so that once the chambers are sealed changes in external (atmospheric) pressure do not affect the measurements. During an experiment, 2.65 g of quartz, which occupies the same volume as the pyrite used in the experiment, is placed in the control chamber so that the volumes of the two chambers are equal. The manometer is made from a 300 mm long, 0.5 mm I.D. glass tube that was bent into the shape of the letter U. It is approximately half filled with an oil that contains a red dye that makes it easily visible. The oil has a density of 0.869 g/mL. This fluid is approximately 15 times less dense and therefore approximately 15 times more sensitive to pressure change than mercury. Pressure measurements are made by measuring the difference in height (in mm) between the oil levels in the two arms of the manometer. With this manometer, we are able to measure pressure differences on the order of 8.4×10^{-5} atm. This translates into changes due to the consumption of as little as 1×10^{-7} moles of oxygen. Vinyl tubes are secured to the end of each arm of the manometer with metal ties and then attached to the reaction and control chambers with luer lock fittings that attach to a stopcock.

The acrylic chambers are cylindrical with a total volume of 28.96 cm^3 . At the top of each chamber are two holes that are sealed with silicone rubber. One is used as a septum that is used

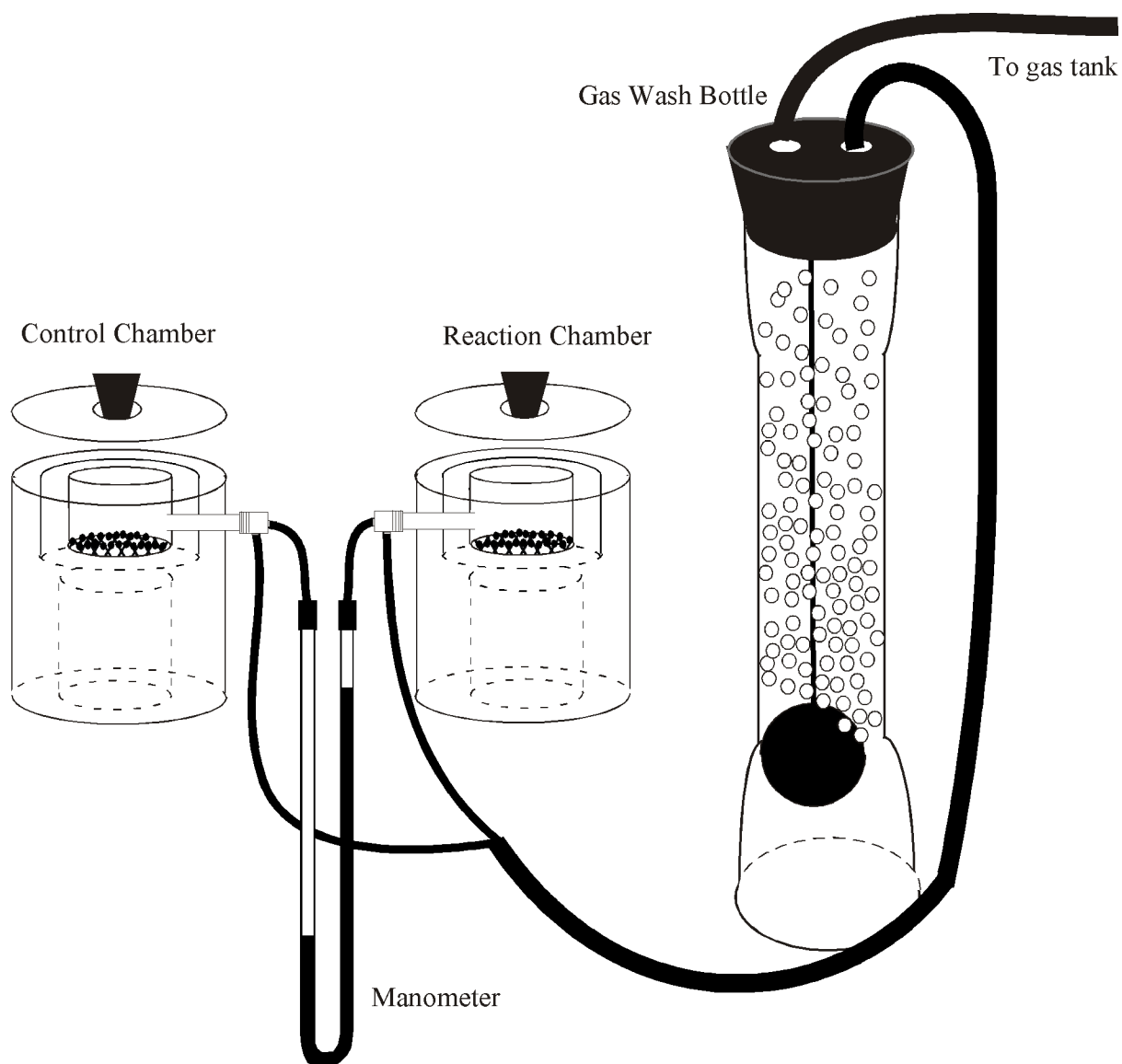


Figure 2-1. Modified Barcroft apparatus used in pyrite oxidation experiments. The reactor consists of two chambers connected by a manometer filled with a low density fluid. The reaction chamber (right) holds pyrite and the control chamber (left) is used as a pressure reference throughout the experiment. The manometer is attached to each chamber via a stopcock. Partial pressure of oxygen is controlled with gas mixtures of known oxygen content. Prior to each experiment, the gas flows from the tank through a gas wash bottle and copper coil into a tee that splits the gas flow into the chambers through the stopcocks. During the experiments, the chambers are sealed and the stopcocks are used to turn off the gas. All change in pressure is due to oxygen consumption by pyrite oxidation.

to withdraw gas samples for calibration purposes. The other holds a glass funnel that is used to place the minerals into the chambers and can be sealed with a silicon stopper. On the side of each chamber is a threaded port that accepts a NPT fitting that attaches to a 3-way stopcock. One position opens to the chamber, one to the manometer, and one to the gas source. The manometer and the gas source are attached to tubing that attaches to the stopcock with luer-fittings. Inside each chamber is a sample holder that is supported by an internal ledge. The holder is a 1.3 cm high by 3.12 cm diameter acrylic ring with 0.32 cm thick walls. Nylon mesh glued to the bottom of the ring supports the sample. Figure 2 shows a schematic representation of the chamber with fittings.

The initial partial pressure of oxygen inside the reactors is set by flowing a gas mixture (O_2-N_2) of known oxygen content through in each chamber. It enters through the 3-way stopcock and exits through the sample funnel. For the $P_{O_2} = 0.21$ experiments, the chambers were flushed with air. A 60.6% O_2 (balance N_2) mixtures was used to set the $P_{O_2} = 0.61$ atm and pure oxygen was used to set the $P_{O_2} = 1.0$ atm. In order to adjust the gas to the relative humidity and temperature of the experiment, the gas flowed from the tank through a gas wash bottle containing a 0.968 m NaCl solution with a $a_{H_2O} = 0.968$ (Robinson and Stokes, 1959) and then through a copper coil immersed in the constant temperature bath that contains the experiment. The output from the copper coil is split with a reducing tee-junction. The two gas streams then flow through the luer fittings that are attached to the stopcocks of each chamber.

The gas-wash bottle, chambers, the stopcocks, and all connections except the manometer are completely immersed in a 25°C water bath during the experiment. The chambers are supported in the bath by an acrylic stand. The manometer is attached to the reactor stand immediately outside the bath.

Experimental Procedure

Experiments were performed at $25 \pm 1^\circ\text{C}$, 96.8% relative humidity, and P_{O_2} values of 0.21, 0.60, and 1.00. Each chamber was filled with 18.00 mL of a 0.968 m NaCl solution that controls relative humidity at 96.8% (Robinson and Stokes, 1959). Once filled, the chambers have a head-space of approximately 10 cm^3 . The apparatus was assembled as shown in Figure 2.

The apparatus is sensitive to even very small pressure leaks. To assure that none were present, prior each experiment, the chambers were sealed and the stopcocks were opened to allow gas to flow in from the tank. The chambers were pressurized to 5 psi and all joints observed for between 6 and 12 hours. If gas bubbles appeared, the chamber was removed and resealed. The apparatus was pressure-tested again after each experiment to assure that leaks did not develop during the experiment.

At the beginning of each experiment the reactors were assembled and the stopcocks opened to allow pressure to equalize between each chamber, the atmosphere, and the gas source. The chambers and manometer were secured to the reactor stand and it was placed in the constant temperature bath. Sealed pyrite ampoules and a test tube containing quartz for the control chamber were also immersed in the bath. All parts of the system remained in the constant temperature bath for 12 hours so they came to thermal equilibrium before an experiment was started.

After the apparatus was thermally equilibrated, quartz sand was poured through the funnel in the control chamber and the regulator on the gas tank was turned down to 1 psi so that there was a small amount of positive pressure to prevent back flow of air into the head-space of the chambers. The pyrite ampoule was opened and pyrite was immediately poured into reaction chamber. Each sample funnel was sealed with a silicone stopper that was held in place by a teflon screw. The gas source to the chambers was closed, first the reaction chamber and then the

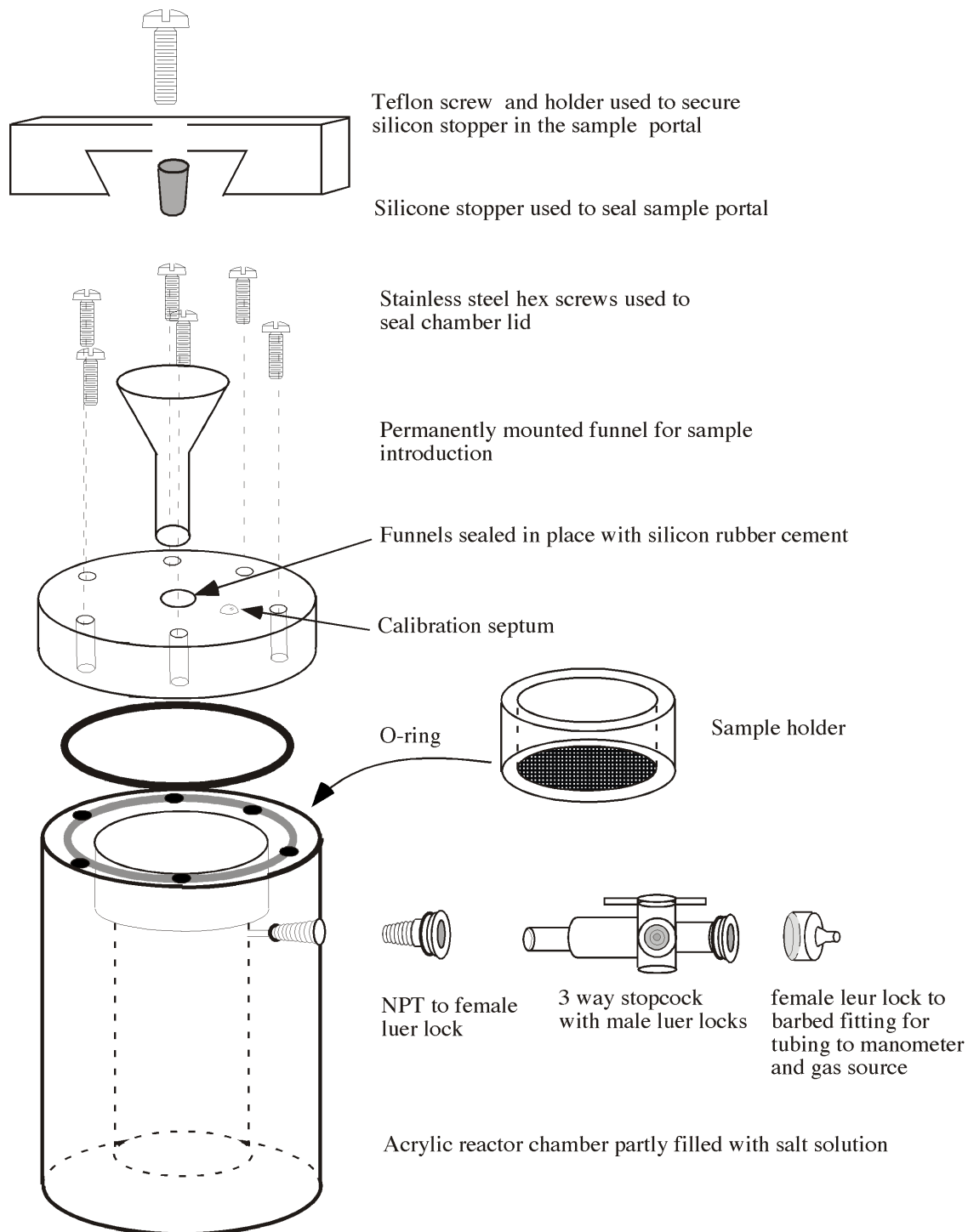


Figure 2-2. Diagram of reaction and control chamber assembly.

control, and the timer was started marking the beginning of the experiment. Both chambers were then fully immersed in the bath.

As the pyrite oxidation reaction consumed oxygen, the pressure inside the reaction chamber decreased and the oil in that arm of the manometer rose. During the experiment, time, the difference in oil height (in mm), bath temperature, room temperature, and atmospheric pressure were recorded. The experiment was stopped when the oil level in the reactor arm reached the top of the manometer. Thus, all experiments proceeded to approximately the same extent of reaction. Four or five duplicate experiments were performed at each partial pressure of oxygen. Experiments were numbered sequentially, regardless of initial oxygen pressure. Several experiments failed, usually due to leaks, and their numbers are not reported in the data table.

The volume/pressure relationship of the reactor was calibrated after each experiment by extracting known volumes of gas from the reaction chamber with a gas syringe and measuring the corresponding change in oil height in the manometer. The ideal gas law was used to calculate the number of moles of oxygen that correspond to this volume. The relationship between the number of moles of oxygen in a volume of gas removed from the chambers and the corresponding change in pressure (measured in mm of oil height) was used to generate a calibration constant that was used to convert raw data (mm of oil height) into moles of oxygen consumed at each time measurement. The calibration procedure was done after each experiment to account for the small changes in head-space that may result from different chambers and manometers.

The concentration of oxygen (mol/m^3) in the reaction chamber at each time was determined by subtracting the number of moles of oxygen consumed divided by the headspace in the chambers ($\sim 10 \text{ cm}^3$) from the initial oxygen concentration in the gas phase. These values were converted to partial pressure of oxygen using the ideal gas law.

After reactor calibration, the chambers were opened and the samples were removed. The quartz was discarded and the pyrite was preserved in a glass jar in a dessicator for later analyses with Field Emission Scanning Electron Microscopy (FESEM) and Energy Dispersive Spectroscopy (EDS).

Rate calculation

The experimental data are reported as of moles of oxygen consumed (n , moles) versus time (t , seconds). The rate of reaction for each duplicate experiment was determined by numerical differentiation of these data. Preliminary analysis of the data showed that they approximately fit a power law of the form:

$$n = k\sqrt{t} \quad (2)$$

(Fig. 3). By taking the derivative of equation 2, the rate could be estimated with an equation of the form

$$r = \frac{dn}{dt} = \frac{k}{2\sqrt{t}} \quad (3)$$

The rate, r_o at each data point (n_o, t_o) was estimated by calculating the slope of the line between the data points prior (n_{-1}, t_{-1}) and following (n_{+1}, t_{+1}):

$$\text{slope}(n_o, t_o) = \frac{n_{+1} - n_{-1}}{\sqrt{t_{+1}} - \sqrt{t_{-1}}}. \quad (4)$$

The slope, which is equal to the rate constant divided by 2, was substituted into equation 3 to find the rate at each time using the equation:

$$r_o = \frac{\text{slope}}{\sqrt{t_o}}. \quad (5)$$

Data points that yielded negative rates were discarded. These numerically determined rates were used to develop the rate models, discussed later.

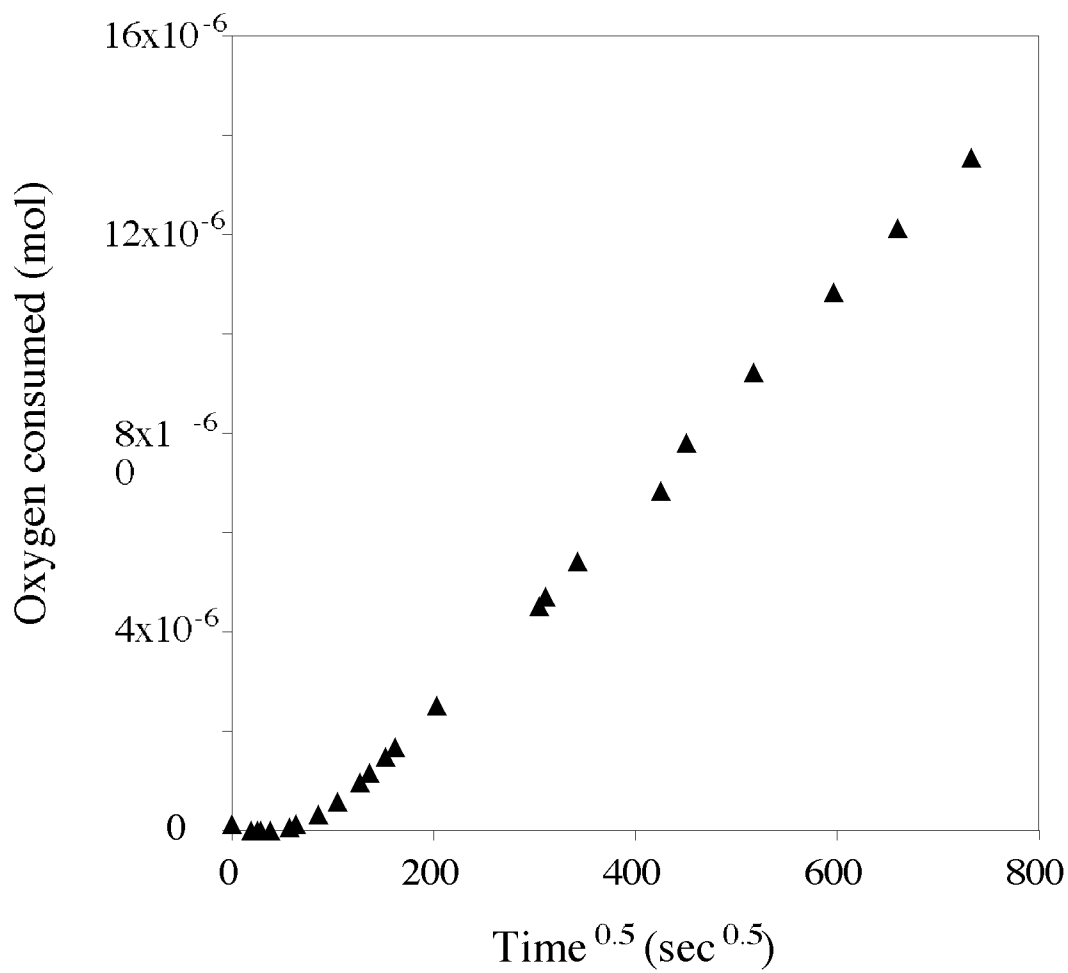


Figure 2-3. Data from experiment PY 43 plotted against the square root of time. The number of moles of oxygen consumed is a linear function of the square root of time over most of the reaction time.

RESULTS

The results of the pyrite oxidation experiments are tabulated in Appendix 1 and shown in Figure 4. The duplicate experiments are represented as different symbols on the graphs at each partial pressure of oxygen.

The numerically determined rates of oxygen consumption at each partial pressure of oxygen (Appendix 1) are shown in Figure 5. The rates slow by approximately two orders of magnitude over the course of each experiment. Oxygen was consumed fastest in the 100% P_{O_2} experiments, and slowest in the 21% P_{O_2} experiments. Note that these results show that $\log r$ is a linear function of $\log t$ and the slopes of these lines are approximately -0.5 .

The pyrite grains adhered together in small clumps when they were removed from the chamber after the experiment, indicating that a solution had formed on the surfaces during oxidation. Field Emission Scanning Electron Microscopy (FESEM) was used to observe dried surface of reacted pyrite grains. Figure 6 shows the anhedral to subhedral crystals that formed by the rapid evaporation of the solution when the pyrite grains were placed in a dessicator. Iron and sulfur were identified in the salts using energy dispersive spectroscopy (EDS), which we interpret to mean that the crystals are iron sulfates that formed from an evaporating ferrous sulfate + sulfuric acid solution. This result is consistent with the observations of Borek (1994) and the chemical reaction that describes pyrite oxidation (equation 1).

DISCUSSION

Our experimental results show that the rate of oxygen consumption by pyrite is a function of time and oxygen partial pressure. The rate at which oxygen was consumed slowed with time and initial rates of reaction increased as the partial pressure of oxygen increased. Our objective is to develop a rate law that is consistent with a physical model and the overall chemical reaction.

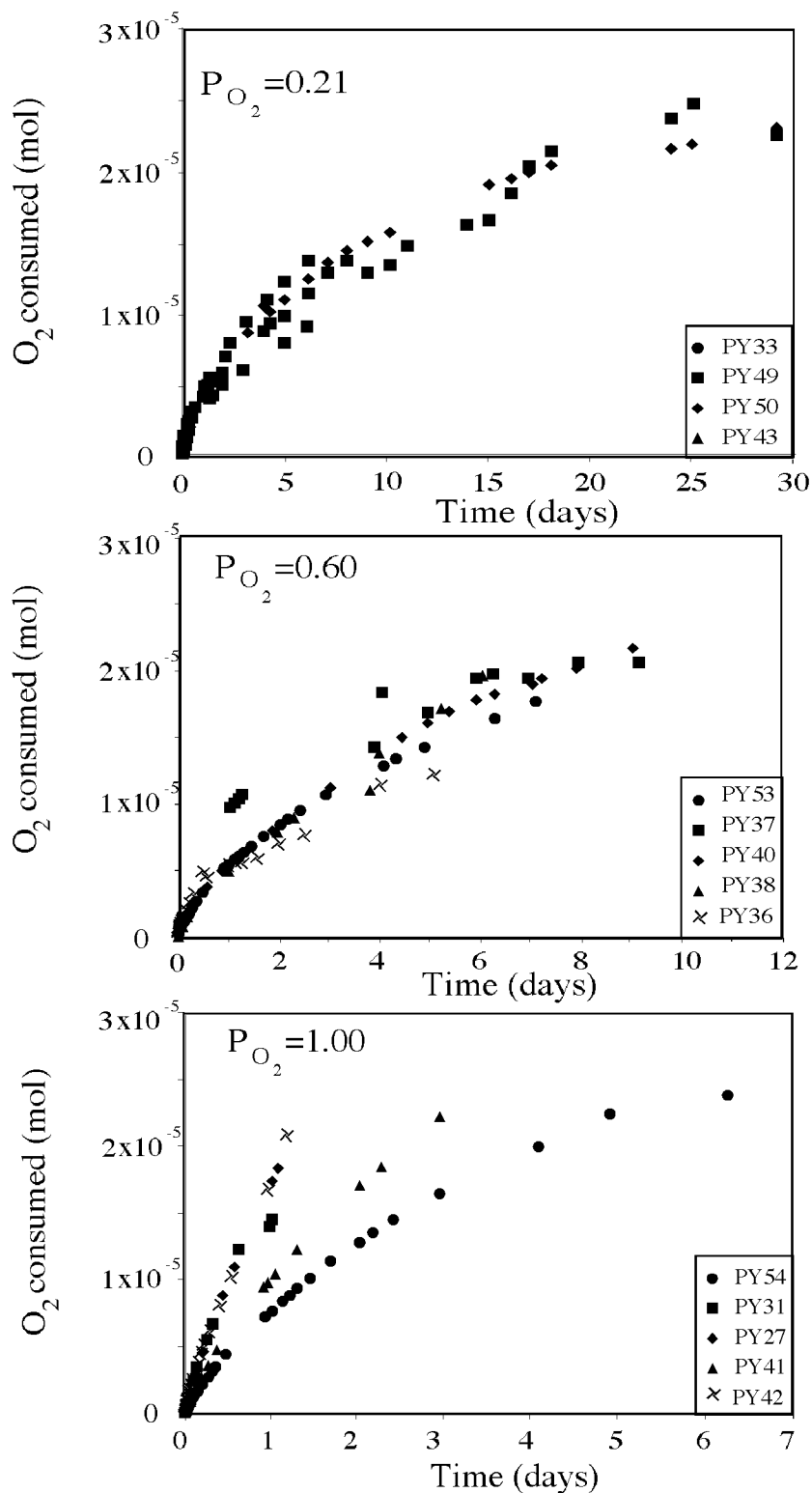


Figure 2-4. Graphs of moles of oxygen consumed versus time at each oxygen partial pressure. Duplicate experiments are shown in different symbols, as indicated in the legend of each graph. The original data are in Appendix I.

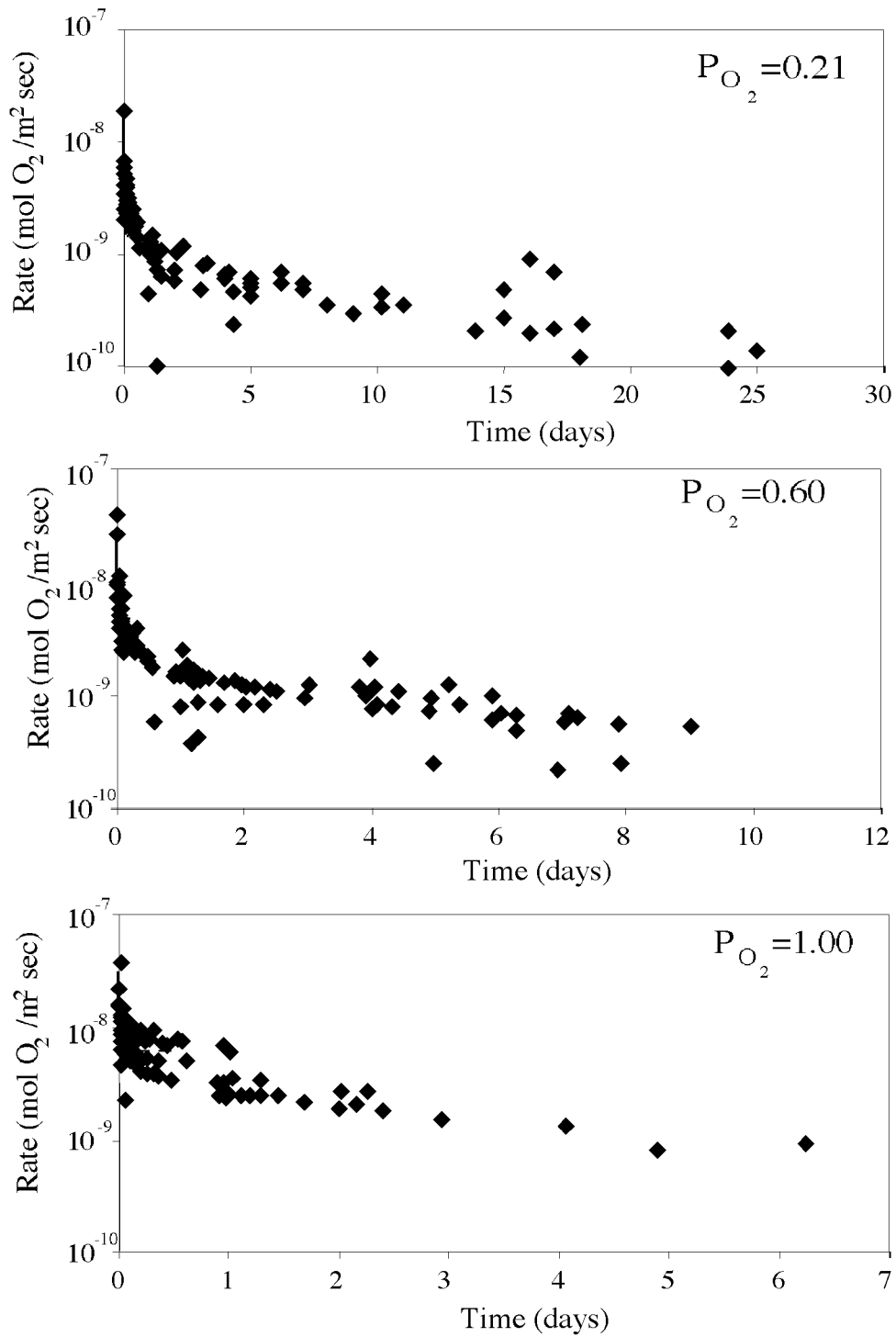


Figure 2-5. Graphs of the numerically determined rate of oxygen consumption versus time. The values for the rate at each measurement are listed in Appendix I.

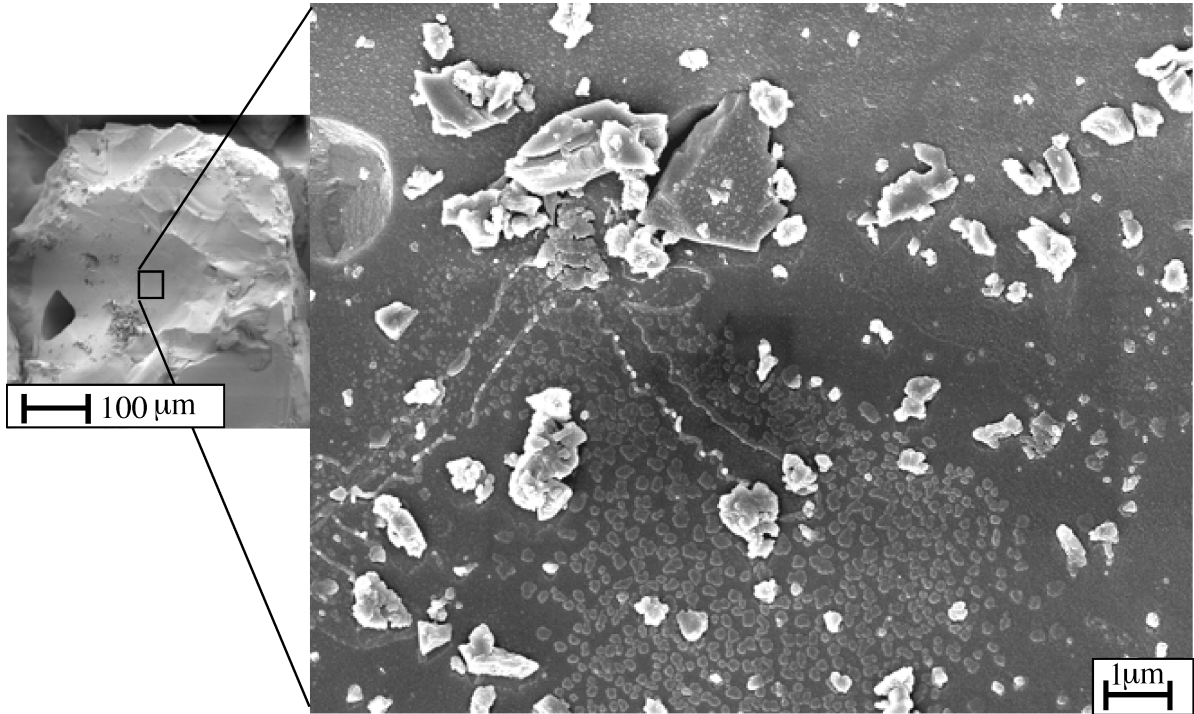


Figure 2-6. FESEM image of pyrite surface after oxidation in humid air. The precipitates contained iron and sulfur as determined by with EDS.

The development of a thin film of solution on the surface of the oxidizing pyrite grains is an important physical process that we must consider. The film is too thin to be seen visually, but we conclude that it must be present because its surface tension caused the reacted pyrite grains to adhere together in small clusters after reaction. In addition, we observed iron sulfate salts that had developed and crystallized on reacted pyrite surfaces after the solution evaporated. Borek (1994) reported a similar wetting of pyrite grains oxidized in moist air. We believe that this solution develops due to the hygroscopic nature of the ferrous sulfate and sulfuric acid reaction products (equation 1).

The thickness of the solution was estimated by calculating the number of mole of ferrous sulfate and sulfuric that are produced as pyrite oxidizes and then estimating the properties of ferrous sulfate + sulfuric acid solutions. For every 3.5 moles of oxygen consumed by pyrite, 1 mole of ferrous sulfate and 1 mole of sulfuric acid are produced (equation 1). Ferrous sulfate and sulfuric acid are hygroscopic and react with the water in vapor phase, which was buffered at by the sodium chloride solution in the bottom of the reactor at 96.8% relative humidity. We used Pitzer equations to calculate the concentration of an equal molar ferrous sulfate + sulfuric acid solution in equilibrium with this relative humidity (approximately 0.5 m, see Appendix 2). In order to maintain a 0.5 m concentration, the reactants must absorb 2 kg (approximately 2 L) of water from the atmosphere for every mole of pyrite oxidized or 0.572 L for every mole of oxygen consumed. Spread over 1 square meter of pyrite surface, the thickness of a solution film produced by this water absorption is 5.72×10^{-5} m/mol O₂ consumed. Therefore, the layer thickness (L) at any extent of reaction can be expressed as the thickness constant (k_l) (5.72×10^{-5} m/mol) multiplied by the number of moles of oxygen consumed.

$$L = k_l n \quad (6)$$

We estimated the solubility of oxygen in a ferrous sulfate + sulfuric acid solution using the methods of Tromans (2000), who developed an empirical function for the solubility of oxygen as a function of solute concentration. The function can be used to determine an apparent Henry's law constant for the solution that formed in our experiments. Although Tromans (2000) did not determine empirical constants for ferrous sulfate + sulfuric acid solutions, he did determine them for magnesium sulfate, copper sulfate, and sodium sulfate. The apparent Henry's law constants of 0.5 m solution of $MgSO_4$, $CuSO_4$, and Na_2SO_4 are 9.60×10^{-4} , 1.09×10^{-3} , and 8.81×10^{-4} , respectively. We chose to model the solubility of oxygen in ferrous sulfate + sulfuric acid solutions with the average (0.985×10^{-3}) of the K_H' of copper sulfate and sodium sulfate because they represent a 2:2 and 1:2 electrolyte solution. The Henry's Law constant of oxygen in pure water is 1.26×10^{-3} , for comparison (Langmuir, 1997). Using an apparent K_H' we can describe the solubility of oxygen in ferrous sulfate + sulfuric acid solution as a function of oxygen partial pressure.

$$C_a = K_H' P \quad (7)$$

It is important to know the solubility of oxygen in the film because once it forms, it is the source of oxygen for the oxidation reaction.

Data analysis.

Data Fitting. There are several ways to derive an empirical rate law from our data. The simplest is to determine the relationship between the measured rates, the elapsed time, and the oxygen partial pressure:

$$r = aP^b t^c \quad (8)$$

where a is a rate constant, b is the reaction order of oxygen, and c is the power exponent of time.

This equation can be linearized by taking the logarithm of both sides.

$$\log r = \log a + b \log P + c \log t. \quad (9)$$

Multilinear regression of the modeled log transformed data was used to determine the approximate values of b ($0.58 \pm .06$), c (-0.42 ± 0.01), and a ($10^{-6.57 \pm 0.07}$). The log transformation changes the weighting of the data, so nonlinear regression is normally a better method to estimate a , b , and c . However, with our data, the NLR model did not converge.

A disadvantage to these methods is they use numerically differentiated rate values and numerical differentiation magnifies minor errors in the original data. Therefore, we fit our data to a generalized integrated form of equation 8 using nonlinear regression:

$$n = dP^e t^f \quad (10)$$

This method of analysis finds values of both e (0.46 ± 0.02) and f (0.54 ± 0.01) that are very close to 0.5, which is consistent with the heuristic model of a process discussed in the next section. If $e = f = 0.5$, equation 10 can be recast to

$$d = \frac{n}{P^{0.5} t^{0.5}} \quad (10)$$

to find a value of d for each measurement. Values of d range from 13.3×10^{-7} to 0.56×10^{-7} with a mean value of $5.49 \pm 0.13 \times 10^{-7}$ (Fig. 7). We believe that the best description of the data is given by

$$n = 10^{-6.3} P^{0.5} t^{0.5}, \quad (11)$$

which can be differentiated to find the rate

$$r = \frac{dn}{dt} = \frac{10^{-6.6} P^{0.5}}{t^{0.5}}. \quad (12)$$

Factors that do not explain the results The rate was observed to slow with time at all partial pressures of oxygen. We considered a number of hypotheses to determine what might cause this decrease in rate. These factors are potential explanations for the slowing of the rate, but do not appear to fully explain our results.

The rate does not slow because of to consumption of a monolayer of reactive sites on the surface of pyrite. There are approximately 1×10^{-7} moles of pyrite in one monolayer on 0.051 m^2 of exposed pyrite surface used in these experiments. For comparison, at least 1×10^{-5} moles of

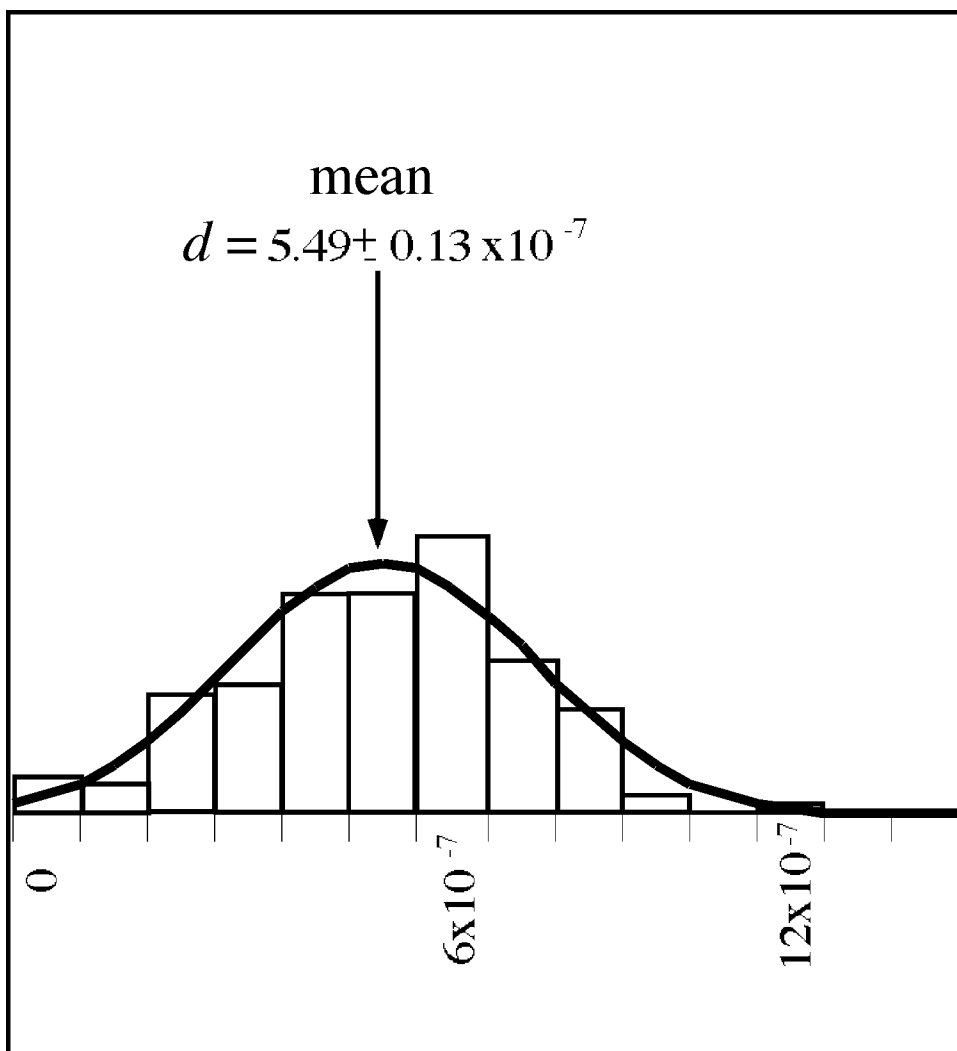


Figure 2-7. Normal distribution of d , the rate constant, calculated from the slope at each data

pyrite were consumed during the experiment. Therefore, if the surface reacted homogeneously, approximately 100 monolayers of pyrite were oxidized in the experiment. It is unlikely that the rate slows due to armoring of the pyrite surface by a solid product. The most likely reaction products are iron sulfate minerals or iron oxide minerals. The sulfuric acid produced by pyrite oxidation will inhibit the oxidation of ferrous to ferric iron because this rate is slow at low pH (Singer and Stumm, 1970) and the low pH will also prevent the hydrolysis and precipitation of any ferric iron that might form. In addition, we did not observe a discoloration of the pyrite surface that would be expected if iron oxyhydroxides had formed. We observed iron sulfate salts on the surface of dried grains, but even then extensive areas of the surface were uncoated.

A great deal of attention has gone to the role of microorganisms in pyrite oxidation. Iron oxidizers such as *Thiobacillus ferrooxidans* and *Leptospirillum ferrooxidans* are known to increase pyrite oxidation rates (Nordstrom and Southam, 1997; Schrenk et al., 1998). However, we do not believe that microbes influenced the rates observed in this study for the following reasons. First, great care was taken in the cleaning and preparation of the chambers and pyrite samples to eliminate microbes. This included washing and sonicating everything in ethyl alcohol and drying at 60°C. Furthermore, the samples were stored in evacuated containers prior to use in the experiments. *T. ferrooxidans* and *L. ferrooxidans* are not known to have a stasis (spore) phase and therefore could not survive this vacuum storage (Staley et al., 1984). Second, the $P_{O_2} = 0.61$ and 1.00 experiments contained no CO_2 , which these species need as their carbon source to grow. Third, if viable bacteria were present and growing in this system, the oxygen consumption rate should increase with time as the microbial population increased rather than decrease as we observed. Finally, we examined the reacted pyrite grains for the presence of bacteria using microscopy. *Thiobacillus ferrooxidans* are known to consume oxygen at a rate of 1.56×10^{-13} mol O_2 /cell day (Lau et al., 1970). If the observed rate of oxygen consumption was due to microbes,

there would have to be $\sim 5 \times 10^7$ cells present in each experiment, or approximately one in every $10 \mu\text{m}^2$. Using FESEM and conventional SEM, we did not observe any bacterial cells. Reacted samples were treated with a fluorescent dye that stains bacteria and observed with a fluorescent confocal microscope. No bacteria were observed with this method either. Finally, unreacted and reacted pyrite samples were rinsed in deionized water and these solutions were measured on an plate prepared with Luria-Bertani agar using the method in Gerhardt et al. (1994) to see if bacteria would grow, but no colonies were observed.

The results of aqueous pyrite oxidation studies were presented in Mckibben and Barnes, (1986) and Williamson and Rimstidt (1994). The aqueous oxidation rate is a function of oxygen concentration to the one half power but does not contain a time component. Our initial observed rate of reaction is approximately the same as the rates reported from aqueous studies, but these rates diverge with increasing time (Fig. 8). We have corrected for the decrease in partial pressure due to oxygen consumption by pyrite, but even with this correction the aqueous rate model does not fit our data for long reaction times.

Explanation of observed rates. Our best explanation for why the rate slowed with time in our experiments is that a film of ferrous sulfate + sulfuric acid grew on the surface as oxidation proceeded, and this film inhibited the transport of oxygen to the surface in direct proportion to the film thickness. We have observed that the rate of pyrite oxidation in air closely matches the rate of oxidation in solution at small values of t . At longer values of t , the rate slows in proportion to the negative square root of time. Based on these behaviors, we believe that the rate of pyrite oxidation in air is a function of oxygen diffusion through a film of ferrous sulfate + sulfuric acid solution, which can be described with Fick's first law of diffusion (Crank, 1975)

$$J = \frac{D}{L}(C_a - C_p). \quad (13)$$

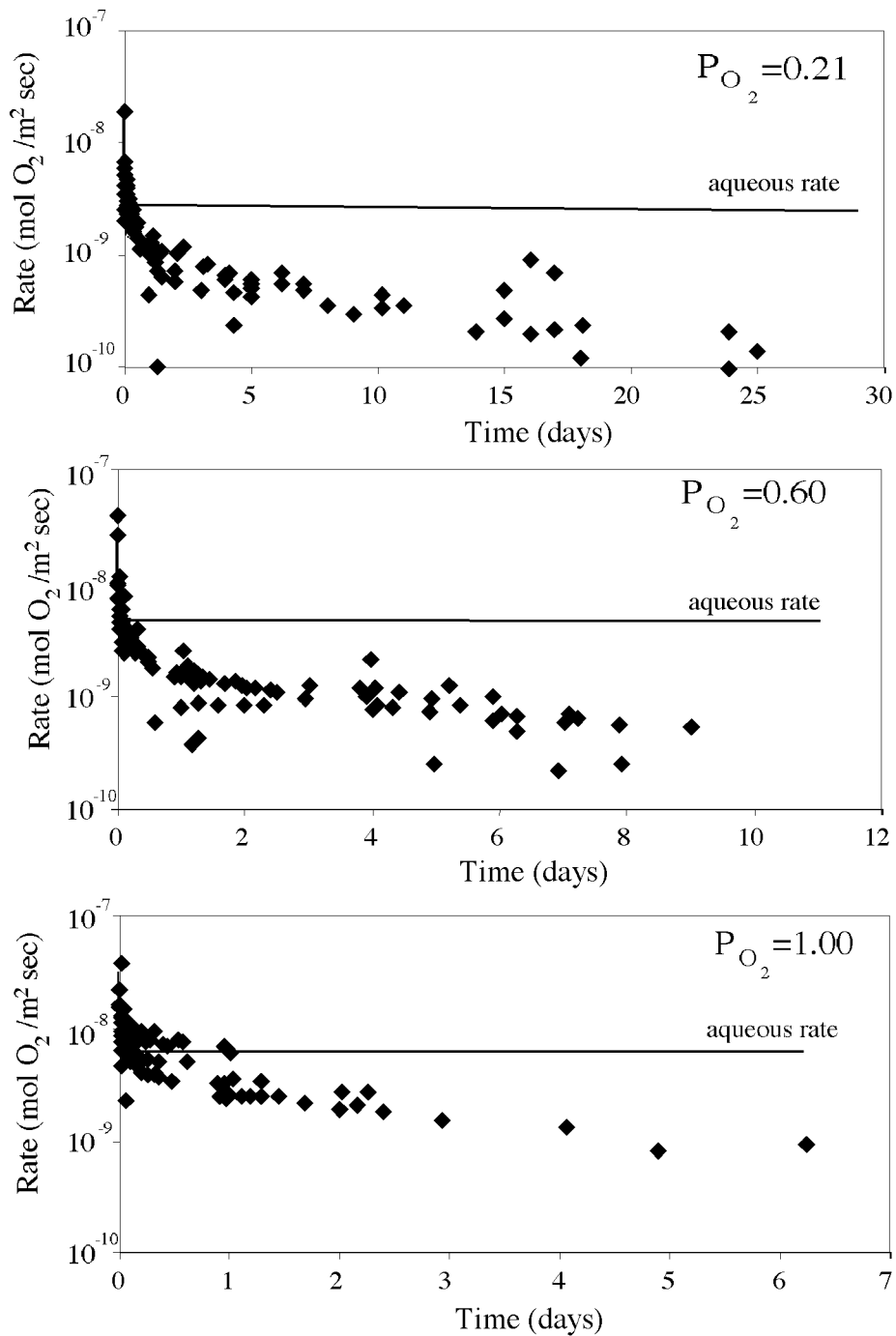


Figure 2-8. Comparison of the rate of oxygen consumption versus time from our experiments (diamonds) and the aqueous oxidation rate (line) adjusted for the declining oxygen partial pressure (Williamson and Rimstidt, 1994).

At steady state, the flux of oxygen through the film is equal to the observed rate of reaction (Fig. 9). If the rate is transport limited it must be a function of film thickness, which is a function of extent of reaction (equation 6), so

$$\frac{dn}{dt} = J = \frac{D}{k_l n} (C_a - C_p). \quad (14)$$

The concentration of oxygen in the solution at the air interface and at the pyrite surface can be recast to partial pressures with the apparent Henry's law constant. Making this substitution, equation 14 becomes

$$\frac{dn}{dt} = \frac{DK'_H}{k_l n} (P_a - P_p), \quad (15)$$

which can be rearranged to

$$\int n dn = \frac{DK'_H}{k_l} (P_a - P_p) \int dt. \quad (16)$$

Integrating equation 16 and solving for n yield the relationship

$$n = \sqrt{\frac{2DK'_H}{k_l} \Delta P^{0.5} t^{0.5}} \quad (17)$$

Assuming P_p is small relative to P_a and $\Delta P^{0.5}$ becomes $P_a^{0.5}$, so equation 17 becomes

$$n = \sqrt{\frac{2DK'_H}{k_l} P_a^{0.5} t^{0.5}} \quad (18)$$

Equation 18 is of the same form as the integrated empirical rate (equation 11) and the so rate constant, d , is equal to $(2DK'_H/k_l n)^{0.5}$. The assumption that P_p is small relative to P_a is only true after a sufficient amount of pyrite has oxidized and the film has had time to develop. We found that after approximately 24 hours, P_p became small with respect to P_a ($\leq 5\%$). We discarded all data for measurements prior to 24 hours and found that value of d , the rate constant, is $6.68 \pm 0.15 \times 10^{-7}$.

The values of the diffusion constant and the Henry's law constant in thin films are likely to be different than the values of those constants in bulk solution because the properties of water

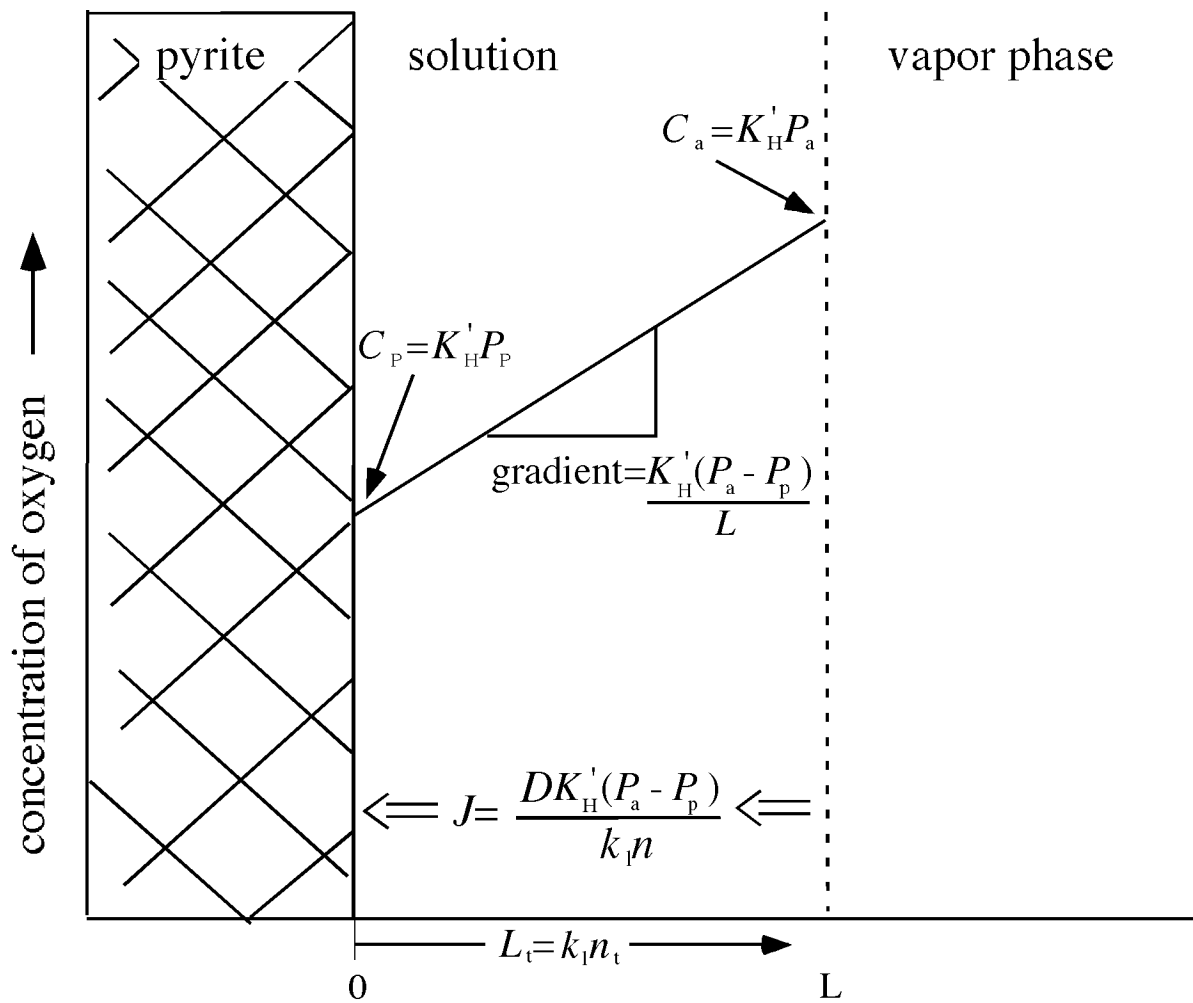


Figure 2-9. Physical model of pyrite oxidation in humid air. At steady state, the rate of oxidation is limited by the transport of oxygen through the film of ferrous sulfate + sulfuric acid solution.

are different (Derjaguin and Churaev, 1986). Using calculated values for d and k_l , we can determine that the apparent value of DK_H' is 1×10^{-16} , which is 7 orders of magnitude less than the value of DK_H in bulk, pure water. Inspection of equation 18 shows that no reasonable range of P , t , or k_l , could provide a range of DK_H' that could close this gap. The difference may be because diffusion through thin films is much slower than in bulk solution, because oxygen is much less soluble in thin films than bulk solution, or both.

Our model fits oxygen consumption for our experiments quite well (Fig. 10). The model was developed to fit the data after 24 hours of reaction, but also does a good job of predicting oxygen consumption at short reaction times.

Comparison with other rates

The initial rates found in this study agree reasonably well with the initial rates of pyrite oxidation in air found by Morth and Smith (1966) (Table 1). Morth and Smith reported that the rate was zero order with respect to time, but inspection of their data, presented in Birle (1963), shows that oxygen consumption slowed in their experiments in a manner similar to ours. The rate law presented by Morth and Smith may be valid for only very short time intervals.

The rates we found using the modified Barcroft apparatus at times longer than 1-10 days approach the rates found using humidity cells, although the humidity cells rates are reported to be zeroth order with respect to time. Humidity cells, which probably represent an average of air oxidation, aqueous oxidation, and oxygen diffusion through gas and liquid filled void spaces, may approximate the rate of oxidation in air after a thick film of aqueous solution develops on the surface of pyrite grains.

Application of data

Implications for field sites. The models by Ritchie (1994), Elberling, et. al (1994), and Elberling and Nicholson (1996) indicate that the rate of pyrite oxidation in the field is limited by oxygen diffusion through the waste pile. Nevertheless, these models require an appropriate

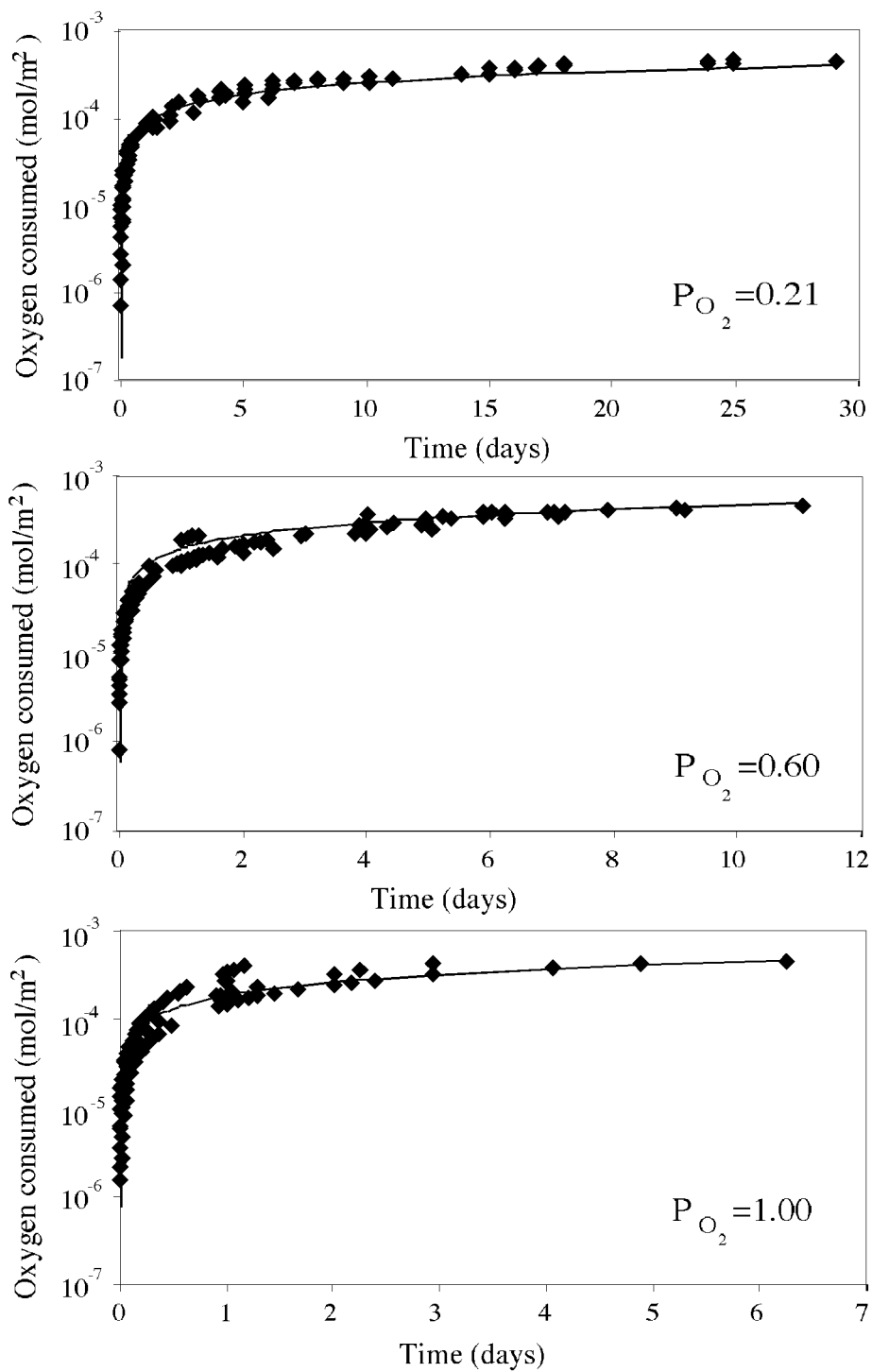


Figure 2-10. Comparison of the number of moles of oxygen consumed versus time from our experiments (diamonds) and the amounts predicted by our transport model (lines).

expression of the oxidation rate at the pyrite surface. The diffusion models assume that the reaction order of oxygen is first order at low oxygen concentrations. Our results suggest that the reaction order of 0.5 may be more appropriate. However, at low oxygen partial pressures, the difference between $P^{0.5}$ and $P^{1.0}$ may be within experimental error.

Our study measures abiotic oxidation rates, but in natural environments microbes could also contribute to the production of acid mine drainage. For example, *Leptospirillum ferrooxidans* have been found in waste piles, and are known to increase the rate of pyrite oxidation (Nordstrom and Southam, 1997; Schrenk et. al, 1998). Thin films of solution associated with oxidizing pyrite may provide an environment for *L. ferrooxidans* growth even in the absence of a bulk aqueous phase.

Implications for museum samples. Museum pyrites probably disaggregate due to the precipitation, in surface cracks, of ferrous sulfates, which have a much larger molar volume than pyrite (V_m pyrite = 23.94 cm³/mol; V_m melanterite = 146.50 cm³/mol; V_m szomolnokite = 55.90 cm³/mol; Robie and Hemmingway, 1995). We know the solubility of ferrous sulfate in sulfuric acid from Linke (1958) and we can use Pitzer equations to predict the activity of water in equilibrium with these solutions (Pitzer, 1991). Using these two pieces of information, we can determine the activity of water (and thus the relative humidity) of ferrous sulfate + sulfuric acid solutions (Fig. 11). During the initial oxidation stage, pyrite produces equal molar quantities of ferrous sulfate and sulfuric acid and these hygroscopic species absorb water from the surrounding vapor. The concentration of ferrous sulfate and sulfuric acid in the solution film that forms on the pyrite surface depends on relative humidity in the air surrounding the samples. dependence is shown graphically as the steeper sloped solid line on Figure 11. At relative humidities between 100 and 95%, the solutions that form are undersaturated with respect to ferrous sulfate phases. Below approximately 95% relative humidity and a molality of

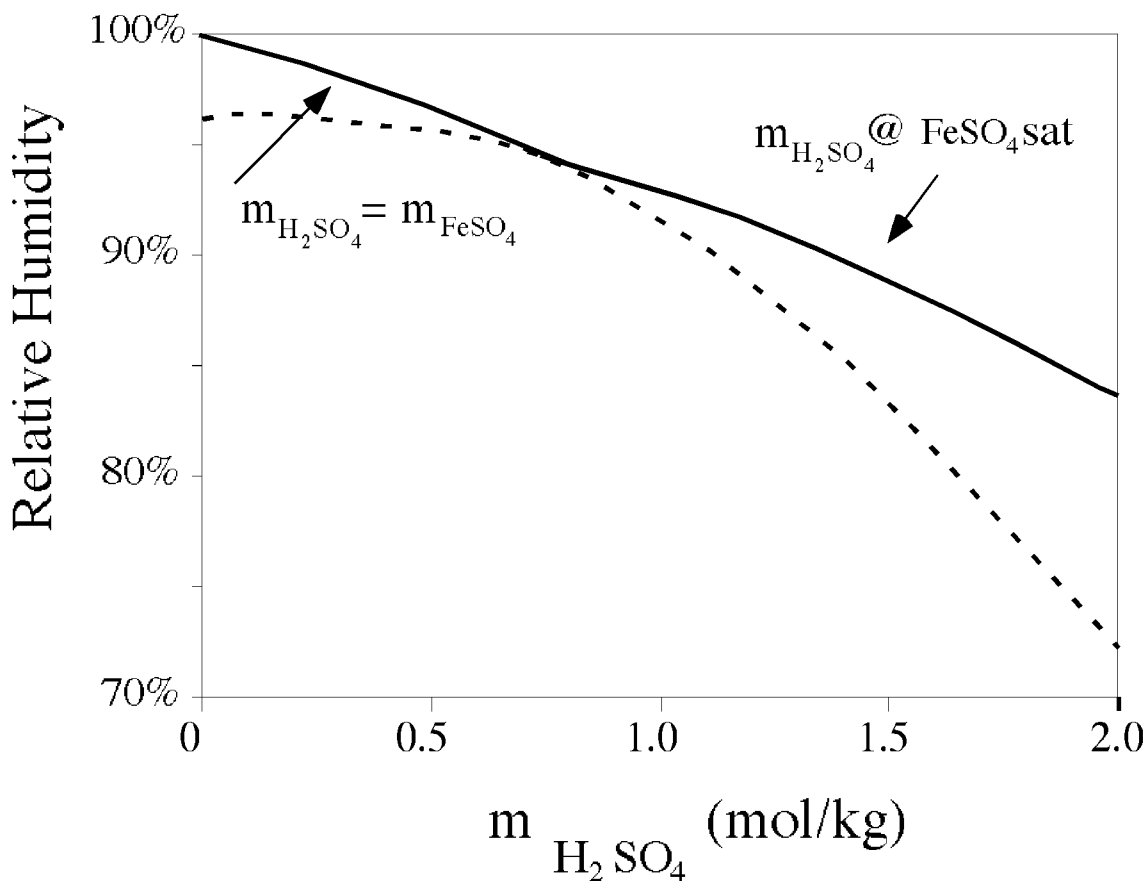


Figure 2-11. Graph showing the concentrations in ferrous sulfate+sulfuric acid solutions in equilibrium with a vapor phase with varying relative humidity. At low concentrations of ferrous sulfate-sulfuric acid, relative humidity decreases with the equal molar increase of the ferrous sulfate and sulfuric acid components of the solution. At approximately 95% relative humidity, a ferrous sulfate solid becomes saturated and further decreases in relative humidity causes solid ferrous sulfate to form while concentration of the sulfuric acid continues to increase.

approximately 0.6, the solution is saturated with ferrous sulfate solid, which coexists with the solution. According to the solubility studies summarized by Linke (1958), szomolnokite is the stable ferrous sulfate at this acidity, but Borek (1994) reported the occurrence of melanterite and rozenite on the surface of pyrite that oxidized in relative humidities between 70% and 79%, so there may be a kinetic barrier to the formation of szomolnokite. All three ferrous sulfates have a larger molar volume than pyrite and should be capable of widening fractures as they crystallize. Pyrite oxidation at relative humidities below 95% relative humidity produces ferrous sulfate solid and ferrous sulfate + sulfuric acid solutions. The solutions that form at moderate relative humidities (70-80%) becomes quite concentrated in H₂SO₄ and the solubility of ferrous sulfate solubility in these solutions is very low.

The formation of ferrous sulfate salts in cracks or void spaces in and between pyrite grains can wedge the sample apart. In addition, the high sulfuric acid concentrations can lead to the dissolution of phases intergrown with the pyrite, leading to disintegration of the entire sample. Our results indicate that at high relative humidities (greater than 96%), the sample may be protected from disaggregation because ferrous sulfate remains undersaturated. The most “dangerous” conditions for pyrite samples is mid-range relative humidities where there is sufficient water present to react with pyrite and form a solution on the surface, but not enough to dissolve ferrous sulfate. At low relative humidities, we presume that the rates become limited by a lack of water.

CONCLUSIONS

We have designed and built a reactor to measure the rate of oxygen consumption by pyrite oxidation in humid air. The rate is:

$$\frac{dn}{dt} = 10^{-6.17} P^{0.5} t^{-0.5}$$

The initial rate of oxidation is equal to or greater than the rate of oxidation in solution at the same partial pressure of oxygen, but slows as a ferrous sulfate + sulfuric acid solution builds on the pyrite surface and the transport of oxygen through the film limits the rate of oxygen delivery to the pyrite surface. At long times, the rate becomes similar to the rates reported using humidity cells.

This rate law can be used to predict the behavior of oxidizing pyrite in waste piles, which is an important factor in acid prediction models. In addition, the results of this study suggest humid environments with relative humidities less than 95% can promote the disintegration of museum pyrite samples because ferrous sulfate phases precipitate. At moderate relative humidities (~70%), the solution that develops on oxidizing pyrite surfaces can become very acidic ($m_{\text{H}_2\text{SO}_4} > 2.0$).

ACKNOWLEDGEMENTS

We appreciate several colleagues at Virginia Tech who helped with this study and the generation of this manuscript. The Barcroft apparatuses and stands were made by Dan Smith. The FESEM photomicrographs were collected with the microscopy skills of Rob Weaver. The search for bacteria was performed with the aid of Steven Lower and Treavor Kendall. This manuscript was improved through the suggestions of James Craig, Patricia Dove, Lee Daniels, and D. Kirk Nordstrom. Funding for this project was provided by a grant from the NSF (EAR-0003364), the Waste Policy Institute at Virginia Tech, and the Graduate Student Assembly at Virginia Tech.

REFERENCES

Bannister F. A. (1933) The preservation of pyrites and marcasite. *The Museums Journal* **33**, 72-75.

- Bannister F. A. (1937) Preservation of Minerals and Meteorites. *The Museums Journal* **36**, 465-476.
- Birle H. D. (1963) Sulfide to Sulfate Reaction Mechanism in Pyritic Materials. M.S., The Ohio State University.
- Borek S. L. (1994) Effect of Humidity on Pyrite Oxidation. *204th National Meeting of the American Chemical Society*, 31-44.
- Brayley S. A. (1960) The oxidation of pyritic conglomerates, pp. 32. Special Report to the Coal Industry Advisory Committee to Ohio River Valley Water Sanit. Comm.
- Crank J. (1975) *The Mathematics of Diffusion*. Clarendon Press.
- Debye P. and Hückel E. (1923) Zur theorie der electrolyte. I. *Zeitschrift für Physik* **24**, 185.
- Derjaguin, B.V., and Churaev, N.V. (1886) Properties of water layers adjacent to interfaces. In Croxton, C.A. (ed) *Fluid Interfacial Phenomena*. Wiley, New York, p 663-738
- Elberling B. and Nicholson R. V. (1996) Field determination of sulphide oxidation rates in mine tailings. *Water Resources Research* **32**(6), 1773-1784.
- Elberling B., Nicholson R. V., and Scharer J. M. (1994) A combined kinetic and diffusion model of pyrite oxidation in tailings: a change in controls with time. *Journal of Hydrology* **157**, 47-60.
- Elsetinow A. R., Guevremont J. M., Strongin D. R., Schoonen M. A. A., and Strongin M. (2000) Oxidation of {100} and {111} surfaces of pyrite: Effects of preparation method. *American Mineralogist* **85**(3-4), 623-626.
- Foust A. S., Wenzel L. A., Clump C. W., Maus L., and Andersen L. B. (1980) *Principles of Unit Operations*. John Wiley & Sons.
- Gerhardt P., Murray R. G. E., Wood W. A., and Krieg N. R. (1994) Methods for General and Molecular Bacteriology, pp. 791. American Society for Microbiology.

- Guevremont J. M., Bebie J., Elsetinow A. R., Strongin D. R., and Schoonen M. A. A. (1998a) Reactivity of the (100) Plane of Pyrite in Oxidizing Gaseous and Aqueous Environments: Effects of Surface Imperfections. *Environmental Science and Technology* **32**, 3743-3748.
- Guevremont J. M., Strongin D. R., and Schoonen M. A. A. (1998b) Thermal chemistry of H₂S and H₂O on the (001) plane of pyrite: Unique reactivity of defects sites. *American Mineralogist* **83**, 1246-1255.
- Hammack R. W. and Watzlaf G. R. (1990) The Effect of Oxygen of Pyrite Oxidation. *Proceedings of the 1990 Mining and Reclamation Conference and Exhibition*, 19 - 25.
- Harvie C. E., Møller N., and Weare J. H. (1984) The prediction of mineral solubilities in natural waters: The Na-K-Mg-Ca-H-Cl-SO₄-OH-HCO₃-CO₂-H₂O system to high ionic strengths at 25°C. *Geochimica et Cosmochimica Acta* **48**(4), 723-751.
- Howie F. M. (1992) Pyrite and marcasite. In *Care and Conservation of Geological Material: Minerals, Rocks, Meteorites and Lunar Finds* (ed. F. M. Howie), pp. 70-84. Butterworth.
- Kelly M. G. (1999) Effects of Heavy Metals on the Aquatic Biota. In *The Environmental Geochemistry of Minerals Deposits*, Vol. 6A (ed. G. S. Plumlee and M. J. Logsdon), pp. 363-371. Society of Economic Geologist.
- Kim H. W. (1964) The effect of water concentration on vapor phase oxidation of pyrite. M.S., The Ohio State University.
- Knipe S. W., Mycroft J. R., Pratt A. R., Nesbitt H. W., and Bancroft G. M. (1995) X-ray photoelectron spectroscopic study of water adsorption on iron sulphide minerals. *Geochimica et Cosmochimica Acta* **59**, 1079-1090.
- Langmuir D. (1997) *Aqueous Environmental Geochemistry*. Prentice Hall.
- Lau C. M., Shumate K. S., and Smith E. E. (1970) The role of bacteria in pyritic oxidation kinetics. *Third Symposium on Coal Mine Drainage Research*, 114-122.
- Linke W. F. (1958) Ferrous Sulfate FeSO₄. In *Solubilities: Inorganic and Metal-Organic Compounds*, Vol. 1, pp. 1046-1053. D. Van Nostrand Company, Inc.

- McKibben M. A. and Barnes H. L. (1986) Oxidation of pyrite in low temperature acidic solutions: rate laws and surface textures. *Geochimica et Cosmochimica Acta* **50**, 1509-1520.
- Morth A. H. and Smith E. E. (1966) Kinetics of the sulfide-to-sulfate reaction. *Am. Chem. Soc. Div. Fuel Chem. Preprints* **10**, 83.
- Nesbitt H. W., Bancroft G. M., Pratt A. R., and Scaini M. J. (1998) Sulfur and iron surface states of fractured pyrite surfaces. *American Mineralogist* **83**(9-10), 1067-1076.
- Nesbitt H. W. and Muir I. J. (1994) X-ray photoelectron spectroscopic study of a pristine pyrite surface reacted with water vapour and air. *Geochimica et Cosmochimica Acta* **58**(21), 4667-4679.
- Nesbitt H. W., Scaini M., Hoechst H., Bancroft G. M., Schaufuss A. G., and Szargan R. (2000) Synchrotron XPS evidence for Fe(II)-S and Fe(III)-S surface species on pyrite fracture-surfaces, and their 3D electronic states. *American Mineralogist* **85**(5-6), 850-857.
- Nicholson R. V., Gillham R. W., and Reardon E. J. (1988) Pyrite oxidation in Carbonate-Buffered Solution. *Geochimica et Cosmochimica Acta* **52**(5), 1077-1085.
- Nordstrom, D. K. and Munoz, J. L. (1994) *Geochemical Thermodynamics*, Blackwell Scientific Publications, 493 p.
- Nordstrom D. K. and Southam G. (1997) Geomicrobiology of Sulfide Mineral Oxidation. In *Geomicrobiology: Interactions Between Microbes and Minerals*, Vol. 35 (ed. J. F. Banfield and K. H. Nealson), pp. 361-390. Reviews in Mineralogy.
- Pitzer K. S. (1973) Thermodynamics of electrolytes. I. Theoretical basis and general equations. *Journal of Physical Chemistry* **77**, 268-277.
- Pitzer K. S. (1991) Ion Interaction Approach: Theory and Data Correlation. In *Activity Coefficients in Electrolyte Solutions* (ed. K. S. Pitzer), pp. 75-153. CRC Press.
- Pitzer K. S., Roy R. N., and Silvester L. F. (1977) Thermodynamics of Electrolytes. 7. Sulfuric Acid. *Journal of the American Chemical Society* **99**, 4930-4936.

- Plumlee G. S. and Logsdon M. J. (1999) The Environmental Geochemistry of Mineral Deposits. In *Reviews in Economic Geology*, Vol. 6A, pp. 369. Society of Economic Geologists, Inc.
- Reardon E. J. and Beckie R. D. (1987) Modeling chemical equilibria of acid mine-drainage: The $\text{FeSO}_4\text{-H}_2\text{SO}_4\text{-H}_2\text{O}$ system. *Geochimica et Cosmochimica Acta* **51**, 2355-2368.
- Ritchie A. I. M. (1994) Rates if Mechanism that Govern Pollutant Generation from Pyritic Wastes. In *Environmental Geochemistry of Sulfide Oxidation* (ed. C. N. Alpers and D. W. Blowes), pp. 108-122. American Chemical Society.
- Robie R. A. and Hemmingway B. S. (1995) Thermodynamic Properties of Minerals and Related Substances at 298.15 K and 1 Bar (10^5 Pascals) Pressure and at Higher Temperatures. U.S. Geological Survey.
- Robinson R. A. and Stokes R. H. (1959) *Electrolyte Solutions: The Measurement and Interpretation of Conductance, Chemical Potential and Diffusion in Solutions of Simple Electrolytes*. Academic Press Inc., Publishers.
- Rogowski A. S. and Pionke H. B. (1984) Hydrology and Water Quality on Strip-mined Lands, pp. 183. U.S. Environmental Protection Agency.
- Schrenk M. O., Edwards K. J., Goodman R. M., Hamers R. J., and Banfield J. F. (1998) Distribution of *Thiobacillus ferrooxidans* and *Leptosprillum ferrooxidans*: Implications for Generation of Acid Mine Drainage. *Science* **279**, 1519-1522.
- Singer P. C. and Stumm W. (1970) Acidic mine drainage: The rate-determining step. *Science* **163**, 1121-123.
- Smith K. S. and Huyck H. L. O. (1999) An Overview of the Abundance, Relative Mobility, Bioavailability, and Human Toxicity of Metals. In *The Environmental Geochemistry of Minerals Deposits*, Vol. 6A (ed. G. S. Plumlee and M. J. Logsdon), pp. 29-70. Society of Economic Geologist.
- Staley J. T., Bryant M. P., Pfenning N., and Holt J. G. (1984) Bergey's Manual of Systematic Bacteriology, Vol. 3, pp. 1842-1858. Williams & Wilkins.
- Tromans D. (2000) Modeling Oxygen Solubility in Water and Electrolyte Solutions. *Industrial and Engineering Chemistry Research* **39**(3), 805-812.

Umbreit W. W., Burris R. H., and Stauffer J. F. (1972) *Manometric and Biochemical Techniques*. Burgess Publishing Company.

Williamson M. A. and Rimstidt J. D. (1994) The kinetics and electrochemical rate-determining step of aqueous pyrite oxidation. *Geochimica et Cosmochimica Acta* **58**, 5443-5454.

APPENDIX 1: DATA FROM ALL SUCCESSFUL EXPERIMENTS

PY33			
<i>t</i>	<i>n</i>	<i>P</i>	<i>r</i>
min	mol	atm	mol/m ² sec
23	2.97x10 ⁻⁷	0.209	
38	3.71x10 ⁻⁷	0.209	5.14x10 ⁻⁹
103	8.16x10 ⁻⁷	0.208	4.05x10 ⁻⁹
183	1.30x10 ⁻⁶	0.207	3.43x10 ⁻⁹
382	2.15x10 ⁻⁶	0.205	2.05x10 ⁻⁹
856	3.23x10 ⁻⁶	0.202	1.12x10 ⁻⁹
1418	3.97x10 ⁻⁶	0.200	4.33x10 ⁻¹⁰
1880	3.93x10 ⁻⁶	0.200	9.97x10 ⁻¹¹
2122	4.08x10 ⁻⁶	0.200	6.21x10 ⁻¹⁰
2865	4.82x10 ⁻⁶	0.198	5.77x10 ⁻¹⁰
4315	5.93x10 ⁻⁶	0.196	4.72x10 ⁻¹⁰
7187	7.78x10 ⁻⁶	0.191	4.23x10 ⁻¹⁰
8722	8.97x10 ⁻⁶	0.188	

PY49			
<i>t</i>	<i>n</i>	<i>P</i>	<i>r</i>
min	mol	atm	mol/m ² sec
6	3.67x10 ⁻⁸	0.210	
10	2.20x10 ⁻⁷	0.209	1.86x10 ⁻⁸
15	2.93x10 ⁻⁷	0.209	6.73x10 ⁻⁹
25	3.67x10 ⁻⁷	0.209	2.56x10 ⁻⁹
33	3.67x10 ⁻⁷	0.209	4.17x10 ⁻⁹
49	5.13x10 ⁻⁷	0.209	5.78x10 ⁻⁹
92	8.43x10 ⁻⁷	0.208	4.78x10 ⁻⁹
131	1.14x10 ⁻⁶	0.207	3.96x10 ⁻⁹
163	1.28x10 ⁻⁶	0.207	3.42x10 ⁻⁹
335	2.05x10 ⁻⁶	0.205	2.24x10 ⁻⁹
452	2.35x10 ⁻⁶	0.204	1.64x10 ⁻⁹
518	2.53x10 ⁻⁶	0.204	1.62x10 ⁻⁹
683	2.90x10 ⁻⁶	0.203	1.41x10 ⁻⁹
1524	4.36x10 ⁻⁶	0.199	9.64x10 ⁻¹⁰
1715	4.66x10 ⁻⁶	0.199	8.74x10 ⁻¹⁰
1850	4.80x10 ⁻⁶	0.198	6.99x10 ⁻¹⁰
2061	5.02x10 ⁻⁶	0.198	6.26x10 ⁻¹⁰
2868	5.72x10 ⁻⁶	0.196	7.28x10 ⁻¹⁰
5749	8.65x10 ⁻⁶	0.189	5.96x10 ⁻¹⁰
6156	9.17x10 ⁻⁶	0.188	4.48x10 ⁻¹⁰
7231	9.64x10 ⁻⁶	0.186	5.09x10 ⁻¹⁰
8883	1.13x10 ⁻⁵	0.183	6.69x10 ⁻¹⁰
10198	1.27x10 ⁻⁵	0.179	5.45x10 ⁻¹⁰
11608	1.35x10 ⁻⁵	0.177	
13065	1.27x10 ⁻⁵	0.179	
14604	1.33x10 ⁻⁵	0.178	4.36x10 ⁻¹⁰
15911	1.46x10 ⁻⁵	0.174	3.50x10 ⁻¹⁰
20017	1.61x10 ⁻⁵	0.171	2.06x10 ⁻¹⁰
21651	1.65x10 ⁻⁵	0.170	4.74x10 ⁻¹⁰
23141	1.83x10 ⁻⁵	0.165	8.78x10 ⁻¹⁰
24427	2.02x10 ⁻⁵	0.161	6.79x10 ⁻¹⁰
26008	2.13x10 ⁻⁵	0.158	2.31x10 ⁻¹⁰
34440	2.35x10 ⁻⁵	0.153	2.07x10 ⁻¹⁰
35945	2.46x10 ⁻⁵	0.150	
41888	2.24x10 ⁻⁵	0.155	

PY43			
<i>t</i>	<i>n</i>	<i>P</i>	<i>r</i>
min	mol	atm	mol/m ² sec
52	7.33x10 ⁻⁸	0.210	
70	1.10x10 ⁻⁷	0.210	2.60x10 ⁻⁹
125	3.37x10 ⁻⁷	0.209	2.62x10 ⁻⁹
187	5.87x10 ⁻⁷	0.209	2.84x10 ⁻⁹
268	9.53x10 ⁻⁷	0.208	3.11x10 ⁻⁹
304	1.17x10 ⁻⁶	0.207	3.12x10 ⁻⁹
387	1.50x10 ⁻⁶	0.206	2.35x10 ⁻⁹
444	1.69x10 ⁻⁶	0.206	2.46x10 ⁻⁹
684	2.53x10 ⁻⁶	0.204	1.94x10 ⁻⁹
1542	4.51x10 ⁻⁶	0.199	1.30x10 ⁻⁹
1620	4.74x10 ⁻⁶	0.198	1.49x10 ⁻⁹
1942	5.39x10 ⁻⁶	0.197	1.04x10 ⁻⁹
3036	6.82x10 ⁻⁶	0.193	1.01x10 ⁻⁹
3390	7.81x10 ⁻⁶	0.191	1.15x10 ⁻⁹
4483	9.24x10 ⁻⁶	0.187	7.82x10 ⁻¹⁰
5927	1.08x10 ⁻⁵	0.184	6.69x10 ⁻¹⁰
7244	1.21x10 ⁻⁵	0.180	5.93x10 ⁻¹⁰
8943	1.35x10 ⁻⁵	0.177	

PY50			
<i>t</i> min	<i>n</i> mol	<i>P</i> atm	<i>r</i> mol/m ² sec
1	4.74x10 ⁻⁷	0.209	
5	7.18x10 ⁻⁸	0.210	
20	7.18x10 ⁻⁸	0.210	
28	7.18x10 ⁻⁸	0.210	2.05x10 ⁻⁹
44	1.44x10 ⁻⁷	0.210	3.50x10 ⁻⁹
87	3.59x10 ⁻⁷	0.209	2.74x10 ⁻⁹
126	5.02x10 ⁻⁷	0.209	2.26x10 ⁻⁹
158	6.10x10 ⁻⁷	0.209	2.96x10 ⁻⁹
330	1.29x10 ⁻⁶	0.207	2.33x10 ⁻⁹
447	1.72x10 ⁻⁶	0.206	2.10x10 ⁻⁹
513	1.90x10 ⁻⁶	0.205	1.90x10 ⁻⁹
678	2.37x10 ⁻⁶	0.204	1.74x10 ⁻⁹
1519	4.16x10 ⁻⁶	0.200	1.18x10 ⁻⁹
1710	4.52x10 ⁻⁶	0.199	1.14x10 ⁻⁹
1845	4.74x10 ⁻⁶	0.198	1.03x10 ⁻⁹
2056	5.06x10 ⁻⁶	0.198	1.07x10 ⁻⁹
4664	8.51x10 ⁻⁶	0.189	8.35x10 ⁻¹⁰
5744	1.04x10 ⁻⁵	0.185	6.41x10 ⁻¹⁰
6151	1.00x10 ⁻⁵	0.186	2.27x10 ⁻¹⁰
7226	1.09x10 ⁻⁵	0.183	5.50x10 ⁻¹⁰
8878	1.23x10 ⁻⁵	0.180	5.54x10 ⁻¹⁰
10193	1.34x10 ⁻⁵	0.177	4.82x10 ⁻¹⁰
11603	1.43x10 ⁻⁵	0.175	3.43x10 ⁻¹⁰
13060	1.49x10 ⁻⁵	0.174	2.90x10 ⁻¹⁰
14599	1.56x10 ⁻⁵	0.172	3.31x10 ⁻¹⁰
21646	1.89x10 ⁻⁵	0.164	2.68x10 ⁻¹⁰
23136	1.94x10 ⁻⁵	0.163	1.94x10 ⁻¹⁰
24422	1.98x10 ⁻⁵	0.162	2.13x10 ⁻¹⁰
26003	2.03x10 ⁻⁵	0.160	1.17x10 ⁻¹⁰
34435	2.15x10 ⁻⁵	0.158	9.37x10 ⁻¹¹
35940	2.18x10 ⁻⁵	0.157	1.36x10 ⁻¹⁰
41883	2.30x10 ⁻⁵	0.154	

PY36			
<i>t</i> min	<i>n</i> mol	<i>P</i> atm	<i>r</i> mol/m ² sec
3	2.72x10 ⁻⁷	0.599	
5	4.27x10 ⁻⁷	0.599	2.67x10 ⁻⁸
13	6.13x10 ⁻⁷	0.599	9.46x10 ⁻⁹
50	9.32x10 ⁻⁷	0.598	4.41x10 ⁻⁹
88	1.16x10 ⁻⁶	0.597	4.42x10 ⁻⁹
122	1.44x10 ⁻⁶	0.596	4.72x10 ⁻⁹
210	1.98x10 ⁻⁶	0.595	3.72x10 ⁻⁹
311	2.52x10 ⁻⁶	0.594	3.28x10 ⁻⁹
453	3.18x10 ⁻⁶	0.592	4.02x10 ⁻⁹
696	4.81x10 ⁻⁶	0.588	2.05x10 ⁻⁹
843	4.47x10 ⁻⁶	0.589	5.83x10 ⁻¹⁰
1438	5.41x10 ⁻⁶	0.587	7.98x10 ⁻¹⁰
1663	5.55x10 ⁻⁶	0.586	3.72x10 ⁻¹⁰
1815	5.63x10 ⁻⁶	0.586	4.29x10 ⁻¹⁰
2278	5.94x10 ⁻⁶	0.586	8.23x10 ⁻¹⁰
2886	6.97x10 ⁻⁶	0.583	8.32x10 ⁻¹⁰
3597	7.62x10 ⁻⁶	0.581	1.08x10 ⁻⁹
5758	1.14x10 ⁻⁵	0.572	7.74x10 ⁻¹⁰
7298	1.22x10 ⁻⁵	0.570	

PY37			
<i>t</i> min	<i>n</i> mol	<i>P</i> atm	<i>r</i> mol/m ² sec
33	8.18x10 ⁻⁷	0.598	
132	1.36x10 ⁻⁶	0.597	7.68x10 ⁻⁹
1472	9.63x10 ⁻⁶	0.577	2.59x10 ⁻⁹
1603	1.00x10 ⁻⁵	0.576	1.83x10 ⁻⁹
1715	1.03x10 ⁻⁵	0.575	1.71x10 ⁻⁹
1829	1.06x10 ⁻⁵	0.574	8.82x10 ⁻¹⁰
5607	1.42x10 ⁻⁵	0.565	9.97x10 ⁻¹⁰
5803	1.83x10 ⁻⁵	0.555	1.18x10 ⁻⁹
7135	1.68x10 ⁻⁵	0.559	2.52x10 ⁻¹⁰
8507	1.93x10 ⁻⁵	0.553	1.00x10 ⁻⁹
8981	1.97x10 ⁻⁵	0.552	
9978	1.93x10 ⁻⁵	0.553	2.23x10 ⁻¹⁰
11404	2.05x10 ⁻⁵	0.550	2.52x10 ⁻¹⁰
13172	2.05x10 ⁻⁵	0.550	

PY38			
<i>t</i> min	<i>n</i> mol	<i>P</i> atm	<i>r</i> mol/m ² sec
2	4.14x10 ⁻⁸	0.600	
112	7.45x10 ⁻⁷	0.598	3.00x10 ⁻⁹
281	1.53x10 ⁻⁶	0.596	2.98x10 ⁻⁹
1440	4.92x10 ⁻⁶	0.588	1.51x10 ⁻⁹
2818	7.90x10 ⁻⁶	0.581	1.26x10 ⁻⁹
3290	8.90x10 ⁻⁶	0.578	8.30x10 ⁻¹⁰
5490	1.10x10 ⁻⁵	0.573	1.18x10 ⁻⁹
5713	1.38x10 ⁻⁵	0.566	2.08x10 ⁻⁹
7522	1.70x10 ⁻⁵	0.558	1.23x10 ⁻⁹
8687	1.95x10 ⁻⁵	0.552	

PY40			
<i>t</i> min	<i>n</i> mol	<i>P</i> atm	<i>r</i> mol/m ² sec
4	1.41x10 ⁻⁷	0.600	
6.5	1.76x10 ⁻⁷	0.600	7.40x10 ⁻⁹
12	2.25x10 ⁻⁷	0.599	7.48x10 ⁻⁹
32	4.22x10 ⁻⁷	0.599	6.90x10 ⁻⁹
65	7.75x10 ⁻⁷	0.598	5.80x10 ⁻⁹
128	1.23x10 ⁻⁶	0.597	4.08x10 ⁻⁹
219	1.73x10 ⁻⁶	0.596	3.22x10 ⁻⁹
381	2.43x10 ⁻⁶	0.594	2.46x10 ⁻⁹
811	3.73x10 ⁻⁶	0.591	1.77x10 ⁻⁹
1260	4.89x10 ⁻⁶	0.588	1.51x10 ⁻⁹
1694	5.81x10 ⁻⁶	0.586	1.45x10 ⁻⁹
1949	6.48x10 ⁻⁶	0.584	1.51x10 ⁻⁹
2690	7.99x10 ⁻⁶	0.581	1.36x10 ⁻⁹
4337	1.12x10 ⁻⁵	0.573	1.23x10 ⁻⁹
6371	1.49x10 ⁻⁵	0.564	1.07x10 ⁻⁹
7132	1.60x10 ⁻⁵	0.561	9.42x10 ⁻¹⁰
7730	1.69x10 ⁻⁵	0.559	8.30x10 ⁻¹⁰
8496	1.77x10 ⁻⁵	0.557	6.08x10 ⁻¹⁰
9045	1.81x10 ⁻⁵	0.556	4.87x10 ⁻¹⁰
10126	1.89x10 ⁻⁵	0.554	6.00x10 ⁻¹⁰
10397	1.94x10 ⁻⁵	0.553	6.37x10 ⁻¹⁰
11375	2.01x10 ⁻⁵	0.551	5.59x10 ⁻¹⁰
12978	2.16x10 ⁻⁵	0.547	

PY53			
<i>t</i> min	<i>n</i> mol	<i>P</i> atm	<i>r</i> mol/m ² sec
7	1.81x10 ⁻⁷	0.600	
10	2.53x10 ⁻⁷	0.599	1.02x10 ⁻⁸
40	5.42x10 ⁻⁷	0.599	3.96x10 ⁻⁹
62	6.15x10 ⁻⁷	0.599	5.05x10 ⁻⁹
81	8.68x10 ⁻⁷	0.598	5.77x10 ⁻⁹
103	9.76x10 ⁻⁷	0.598	2.55x10 ⁻⁹
160	1.16x10 ⁻⁶	0.597	2.39x10 ⁻⁹
220	1.41x10 ⁻⁶	0.597	2.83x10 ⁻⁹
304	1.77x10 ⁻⁶	0.596	2.89x10 ⁻⁹
390	2.17x10 ⁻⁶	0.595	2.88x10 ⁻⁹
452	2.44x10 ⁻⁶	0.594	2.73x10 ⁻⁹
520	2.71x10 ⁻⁶	0.593	2.47x10 ⁻⁹
687	3.29x10 ⁻⁶	0.592	2.22x10 ⁻⁹
1324	5.13x10 ⁻⁶	0.587	1.63x10 ⁻⁹
1440	5.42x10 ⁻⁶	0.587	1.57x10 ⁻⁹
1612	5.82x10 ⁻⁶	0.586	1.45x10 ⁻⁹
1730	6.07x10 ⁻⁶	0.585	1.33x10 ⁻⁹
1861	6.33x10 ⁻⁶	0.585	1.35x10 ⁻⁹
2084	6.80x10 ⁻⁶	0.583	1.42x10 ⁻⁹
2418	7.52x10 ⁻⁶	0.582	1.33x10 ⁻⁹
2893	8.42x10 ⁻⁶	0.579	1.18x10 ⁻⁹
3122	8.82x10 ⁻⁶	0.578	1.19x10 ⁻⁹
3454	9.44x10 ⁻⁶	0.577	1.12x10 ⁻⁹
4230	1.07x10 ⁻⁵	0.574	9.58x10 ⁻¹⁰
5867	1.28x10 ⁻⁵	0.569	8.25x10 ⁻¹⁰
6221	1.33x10 ⁻⁵	0.567	7.97x10 ⁻¹⁰
7044	1.42x10 ⁻⁵	0.565	7.37x10 ⁻¹⁰
9011	1.64x10 ⁻⁵	0.560	6.74x10 ⁻¹⁰
10222	1.76x10 ⁻⁵	0.557	6.99x10 ⁻¹⁰
15918	2.31x10 ⁻⁵	0.544	

PY27			
<i>t</i> min	<i>n</i> mol	<i>P</i> atm	<i>r</i> mol/m ² sec
2	1.12x10 ⁻⁷	1.000	
5	1.86x10 ⁻⁷	1.000	1.55x10 ⁻⁸
10	2.98x10 ⁻⁷	0.999	1.64x10 ⁻⁸
15	4.46x10 ⁻⁷	0.999	1.46x10 ⁻⁸
26	6.32x10 ⁻⁷	0.998	9.46x10 ⁻⁹
29	6.69x10 ⁻⁷	0.998	1.24x10 ⁻⁸
43	9.30x10 ⁻⁷	0.998	1.49x10 ⁻⁸
132	2.49x10 ⁻⁶	0.994	9.03x10 ⁻⁹
169	2.98x10 ⁻⁶	0.993	1.01x10 ⁻⁸
281	4.61x10 ⁻⁶	0.989	9.60x10 ⁻⁹
629	8.93x10 ⁻⁶	0.978	7.08x10 ⁻⁹
816	1.10x10 ⁻⁵	0.973	7.60x10 ⁻⁹
1449	1.76x10 ⁻⁵	0.957	5.94x10 ⁻⁹
1544	1.84x10 ⁻⁵	0.955	

PY41			
<i>t</i> min	<i>n</i> mol	<i>P</i> atm	<i>r</i> mol/m ² sec
3	8.89x10 ⁻⁷	0.998	
9	3.23x10 ⁻⁷	0.999	
20	5.25x10 ⁻⁷	0.999	8.60x10 ⁻⁹
33	6.46x10 ⁻⁷	0.998	3.77x10 ⁻⁸
24	8.08x10 ⁻⁷	0.998	6.20x10 ⁻⁹
85	9.69x10 ⁻⁷	0.998	2.31x10 ⁻⁹
97	1.13x10 ⁻⁶	0.997	8.00x10 ⁻⁹
158	1.78x10 ⁻⁶	0.996	6.44x10 ⁻⁹
268	2.75x10 ⁻⁶	0.993	5.51x10 ⁻⁹
378	3.68x10 ⁻⁶	0.991	5.31x10 ⁻⁹
524	4.81x10 ⁻⁶	0.988	5.05x10 ⁻⁹
1297	9.53x10 ⁻⁶	0.977	3.23x10 ⁻⁹
1375	9.86x10 ⁻⁶	0.976	3.31x10 ⁻⁹
1498	1.05x10 ⁻⁵	0.974	3.54x10 ⁻⁹
1846	1.23x10 ⁻⁵	0.970	3.34x10 ⁻⁹
2901	1.72x10 ⁻⁵	0.958	2.73x10 ⁻⁹
3244	1.86x10 ⁻⁵	0.955	2.70x10 ⁻⁹
4215	2.24x10 ⁻⁵	0.945	

PY31			
<i>t</i> min	<i>n</i> mol	<i>P</i> atm	<i>r</i> mol/m ² sec
4	7.86x10 ⁻⁸	1.000	
34	7.07x10 ⁻⁷	0.998	1.13x10 ⁻⁸
85	1.53x10 ⁻⁶	0.996	1.08x10 ⁻⁸
138	2.51x10 ⁻⁶	0.994	1.10x10 ⁻⁸
204	3.53x10 ⁻⁶	0.991	9.72x10 ⁻⁹
356	5.54x10 ⁻⁶	0.986	7.73x10 ⁻⁹
466	6.79x10 ⁻⁶	0.983	9.41x10 ⁻⁹
888	1.23x10 ⁻⁵	0.970	5.06x10 ⁻⁹
1406	1.41x10 ⁻⁵	0.966	2.40x10 ⁻⁹
1449	1.46x10 ⁻⁵	0.964	

PY54			
<i>t</i> min	<i>n</i> mol	<i>P</i> atm	<i>r</i> mol/m ² sec
18	1.40x10 ⁻⁷	1.000	
35	2.44x10 ⁻⁷	0.999	4.66x10 ⁻⁹
57	4.19x10 ⁻⁷	0.999	5.93x10 ⁻⁹
76	6.28x10 ⁻⁷	0.998	6.68x10 ⁻⁹
98	8.38x10 ⁻⁷	0.998	5.87x10 ⁻⁹
155	1.29x10 ⁻⁶	0.997	5.00x10 ⁻⁹
215	1.75x10 ⁻⁶	0.996	4.66x10 ⁻⁹
299	2.30x10 ⁻⁶	0.994	4.12x10 ⁻⁹
385	2.83x10 ⁻⁶	0.993	3.92x10 ⁻⁹
447	3.21x10 ⁻⁶	0.992	3.86x10 ⁻⁹
515	3.59x10 ⁻⁶	0.991	3.64x10 ⁻⁹
682	4.47x10 ⁻⁶	0.989	3.43x10 ⁻⁹
1319	7.33x10 ⁻⁶	0.982	2.54x10 ⁻⁹
1435	7.78x10 ⁻⁶	0.981	2.64x10 ⁻⁹
1607	8.48x10 ⁻⁶	0.979	2.49x10 ⁻⁹
1725	8.90x10 ⁻⁶	0.978	2.48x10 ⁻⁹
1856	9.42x10 ⁻⁶	0.977	2.48x10 ⁻⁹
2079	1.02x10 ⁻⁵	0.975	2.48x10 ⁻⁹
2413	1.15x10 ⁻⁵	0.972	2.17x10 ⁻⁹
2888	1.29x10 ⁻⁵	0.969	1.90x10 ⁻⁹
3117	1.36x10 ⁻⁵	0.967	2.05x10 ⁻⁹
3449	1.46x10 ⁻⁵	0.964	1.80x10 ⁻⁹
4225	1.66x10 ⁻⁵	0.960	1.55x10 ⁻⁹
5862	2.01x10 ⁻⁵	0.951	1.36x10 ⁻⁹
7039	2.26x10 ⁻⁵	0.945	8.16x10 ⁻¹⁰
9006	2.40x10 ⁻⁵	0.941	

APPENDIX 2: PITZER EQUATIONS

In order to generate the values for $a_{\text{H}_2\text{O}}$ at different concentrations of ferrous sulfate and/or sulfuric acid, we used the equations developed by (Pitzer, 1973). This method approximates the osmotic coefficient of water and single-ion activity coefficients by estimating the excess Gibbs free energy (G^{ex}) due to the interaction between ions in solution. This method builds on the earlier work of Debye and Hückel (1923), who considered osmotic and activity coefficients to be primarily a function of ionic strength. In addition to the Debye-Hückel limiting slope, Pitzer considered short-range binary interaction between cation-anion, cation-cation, and anion-anion pairs and ternary interactions involving cation-cation-anion and anion-anion-cation. The ion pair interaction are modeled using the second virial coefficients B and ϕ , which are a function of ionic strength, and the ternary interactions are modeling using the third virial coefficients C and Ψ , which are independent of ionic strength (Pitzer, 1991). The general equation for calculating the osmotic coefficient of water is:

$$(\phi - 1) = \left(\frac{2}{\sum_i m_i} \right) \left\{ -A_\phi I^{3/2} / (1 + b\sqrt{I}) \right\} + \left\{ \sum_c \sum_a m_c m_a (B_{ca}^\phi + ZC_{ca}) \right\} \\ + \left\{ \sum_{c>c'} \sum_c m_c m_{c'} (\Phi_{cc'}^\phi + \sum_a m_a \Psi_{cc'a}) \right\} + \left\{ \sum_{a>a'} \sum_a m_a m_{a'} (\Phi_{aa'}^\phi + \sum_c m_c \Psi_{aa'c}) \right\}$$

The symbol m_{ca} refers to the molal concentration of cations (c) or anions (a). In the system, $\text{FeSO}_4\text{-H}_2\text{SO}_4\text{-H}_2\text{O}$, there are two cations (Fe^{+2} , and H^+) and two anions (HSO_4^- , and SO_4^{2-}). The general Pitzer equation can then be evaluated for this system in the following manner:

$$(\phi - 1) = \frac{2}{m_{\text{Fe}} + m_{\text{H}} + m_{\text{SO}_4} + m_{\text{HSO}_4}} \left[\begin{aligned} & \left(-A_\phi I^{3/2} / (1 + b\sqrt{I}) \right) \\ & + \left(\{m_{\text{Fe}} m_{\text{SO}_4} (B_{\text{FeSO}_4}^\phi + ZC_{\text{FeSO}_4})\} + \{m_{\text{Fe}} m_{\text{HSO}_4} (B_{\text{FeHSO}_4}^\phi + ZC_{\text{FeHSO}_4})\} \right) \\ & + \left(\{m_{\text{H}} m_{\text{SO}_4} (B_{\text{H,SO}_4}^\phi + ZC_{\text{H,SO}_4})\} + \{m_{\text{H}} m_{\text{HSO}_4} (B_{\text{H,HSO}_4}^\phi + ZC_{\text{H,HSO}_4})\} \right) \\ & + \left(m_{\text{Fe}} m_{\text{H}} [\Phi_{\text{Fe,H}}^\phi + \{(m_{\text{SO}_4} \Psi_{\text{Fe,H,SO}_4}) + (m_{\text{HSO}_4} \Psi_{\text{Fe,H,HSO}_4})\}] \right) \\ & + \left(m_{\text{SO}_4} m_{\text{HSO}_4} [\Phi_{\text{SO}_4,\text{HSO}_4}^\phi + \{(m_{\text{Fe}} \Psi_{\text{SO}_4,\text{HSO}_4,\text{Fe}}) + (m_{\text{H}} \Psi_{\text{SO}_4,\text{HSO}_4,\text{H}})\}] \right) \end{aligned} \right]$$

At 25°C, A_ϕ has value of 0.3915 and b a universal constant at all temperatures equal to 1.2. The symbols B^ϕ , C , I , and Z are functions that are defined by the following equations:

$$B_{\text{FeSO}_4}^\phi = \beta_{\text{FeSO}_4}^{(0)} + \beta_{\text{FeSO}_4}^{(1)} e^{(-1.4\sqrt{I})} + \beta_{\text{FeSO}_4}^{(2)} e^{(-12\sqrt{I})} \\ B_{\text{H,SO}_4}^\phi = \beta_{\text{H,SO}_4}^{(0)} + \beta_{\text{H,SO}_4}^{(1)} e^{(-1.4\sqrt{I})} \\ B_{\text{Fe,HSO}_4}^\phi = \beta_{\text{Fe,HSO}_4}^{(0)} + \beta_{\text{Fe,HSO}_4}^{(1)} e^{(-1.4\sqrt{I})} \\ B_{\text{H,HSO}_4}^\phi = \beta_{\text{H,SO}_4}^{(0)} + \beta_{\text{H,HSO}_4}^{(1)} e^{(-1.4\sqrt{I})} \\ C_{\text{MX}} = \frac{C_{\text{MX}}^\phi}{2|z_M z_x|^{1/2}}$$

$$I = \frac{1}{2} \sum_i m_i z_i^2 = \frac{1}{2} (m_{\text{Fe}} z_{\text{Fe}}^2 + m_{\text{H}} z_{\text{H}}^2 + m_{\text{SO}_4} z_{\text{SO}_4}^2 + m_{\text{HSO}_4} z_{\text{HSO}_4}^2)$$

$$Z = \sum_i m_i |z_i| = m_{\text{Fe}} |z_{\text{Fe}}| + m_{\text{H}} |z_{\text{H}}| + m_{\text{SO}_4} |z_{\text{SO}_4}| + m_{\text{HSO}_4} |z_{\text{HSO}_4}|$$

The parameters β_{MX}^ϕ , C_{MX}^ϕ , ϕ_{MX} , and ψ_{MX} were determined experimentally by Pitzer et al. (1977), Harvie et al. (1984), and Reardon and Beckie (1987).

By including the functions defined above into the equation for the osmotic coefficient, we obtained the following expression:

$$(\phi - 1) = \frac{2}{m_{\text{Fe}} + m_{\text{H}} + m_{\text{SO}_4} + m_{\text{HSO}_4}} \times$$

$$\left[\begin{aligned} & \left(-A_\phi \frac{\left(\frac{1}{2} (m_{\text{Fe}} z_{\text{Fe}}^2 + m_{\text{H}} z_{\text{H}}^2 + m_{\text{SO}_4} z_{\text{SO}_4}^2 + m_{\text{HSO}_4} z_{\text{HSO}_4}^2) \right)^{3/2}}{1 + b \sqrt{\frac{1}{2} (m_{\text{Fe}} z_{\text{Fe}}^2 + m_{\text{H}} z_{\text{H}}^2 + m_{\text{SO}_4} z_{\text{SO}_4}^2 + m_{\text{HSO}_4} z_{\text{HSO}_4}^2)}} \right) \\ & + \left(m_{\text{Fe}} m_{\text{SO}_4} \left\{ \begin{aligned} & \left[\beta_{\text{FeSO}_4}^{(0)} + \beta_{\text{FeSO}_4}^{(1)} \exp^{-1.4 \sqrt{\frac{1}{2} (m_{\text{Fe}} z_{\text{Fe}}^2 + m_{\text{H}} z_{\text{H}}^2 + m_{\text{SO}_4} z_{\text{SO}_4}^2 + m_{\text{HSO}_4} z_{\text{HSO}_4}^2)}} \right] \\ & + \beta_{\text{FeSO}_4}^{(2)} \exp^{-12 \sqrt{\frac{1}{2} (m_{\text{Fe}} z_{\text{Fe}}^2 + m_{\text{H}} z_{\text{H}}^2 + m_{\text{SO}_4} z_{\text{SO}_4}^2 + m_{\text{HSO}_4} z_{\text{HSO}_4}^2)}} \right] \\ & + C_{\text{FeSO}_4} \{ m_{\text{Fe}} |z_{\text{Fe}}| + m_{\text{H}} |z_{\text{H}}| + m_{\text{SO}_4} |z_{\text{SO}_4}| + m_{\text{HSO}_4} |z_{\text{HSO}_4}| \} \end{aligned} \right\} \\ & + m_{\text{Fe}} m_{\text{HSO}_4} \left\{ \begin{aligned} & \left[\beta_{\text{Fe,HSO}_4}^{(0)} + \beta_{\text{Fe,HSO}_4}^{(1)} \exp^{-1.4 \sqrt{\frac{1}{2} (m_{\text{Fe}} z_{\text{Fe}}^2 + m_{\text{H}} z_{\text{H}}^2 + m_{\text{SO}_4} z_{\text{SO}_4}^2 + m_{\text{HSO}_4} z_{\text{HSO}_4}^2)}} \right] \\ & + C_{\text{Fe,HSO}_4} \{ m_{\text{Fe}} |z_{\text{Fe}}| + m_{\text{H}} |z_{\text{H}}| + m_{\text{SO}_4} |z_{\text{SO}_4}| + m_{\text{HSO}_4} |z_{\text{HSO}_4}| \} \end{aligned} \right\} \\ & + \{ m_{\text{H}} m_{\text{SO}_4} \left\{ \begin{aligned} & \left[\beta_{\text{H,SO}_4}^{(0)} + \beta_{\text{H,SO}_4}^{(1)} \exp^{-1.4 \sqrt{\frac{1}{2} (m_{\text{Fe}} z_{\text{Fe}}^2 + m_{\text{H}} z_{\text{H}}^2 + m_{\text{SO}_4} z_{\text{SO}_4}^2 + m_{\text{HSO}_4} z_{\text{HSO}_4}^2)}} \right] \\ & + C_{\text{H,SO}_4} \{ m_{\text{Fe}} |z_{\text{Fe}}| + m_{\text{H}} |z_{\text{H}}| + m_{\text{SO}_4} |z_{\text{SO}_4}| + m_{\text{HSO}_4} |z_{\text{HSO}_4}| \} \end{aligned} \right\} \\ & + \{ m_{\text{H}} m_{\text{HSO}_4} \left\{ \begin{aligned} & \left[\beta_{\text{H,HSO}_4}^{(0)} + \beta_{\text{H,HSO}_4}^{(1)} \exp^{-1.4 \sqrt{\frac{1}{2} (m_{\text{Fe}} z_{\text{Fe}}^2 + m_{\text{H}} z_{\text{H}}^2 + m_{\text{SO}_4} z_{\text{SO}_4}^2 + m_{\text{HSO}_4} z_{\text{HSO}_4}^2)}} \right] \\ & + C_{\text{H,HSO}_4} \{ m_{\text{Fe}} |z_{\text{Fe}}| + m_{\text{H}} |z_{\text{H}}| + m_{\text{SO}_4} |z_{\text{SO}_4}| + m_{\text{HSO}_4} |z_{\text{HSO}_4}| \} \end{aligned} \right\} \right\} \\ & + (m_{\text{Fe}} m_{\text{H}} [\Phi_{\text{Fe,H}}^\phi + \{ (m_{\text{SO}_4} \Psi_{\text{Fe,H,SO}_4}) + (m_{\text{HSO}_4} \Psi_{\text{Fe,H,HSO}_4}) \}]) \\ & + (m_{\text{SO}_4} m_{\text{HSO}_4} [\Phi_{\text{SO}_4,\text{HSO}_4}^\phi + \{ (m_{\text{Fe}} \Psi_{\text{SO}_4,\text{HSO}_4,\text{Fe}}) + (m_{\text{H}} \Psi_{\text{SO}_4,\text{HSO}_4,\text{H}}) \}]) \end{aligned} \right]$$

Substituting the values for the parameters β_{MX}^ϕ , C_{MX}^ϕ , ϕ_{MX} , and ψ_{MX} , and the charge on the iron, the equation to define the osmotic coefficient as a function of concentration of ferrous sulfate and sulfuric acid becomes:

$$(\phi - 1) = \frac{2}{m_{\text{Fe}} + m_{\text{H}} + m_{\text{SO}_4} + m_{\text{HSO}_4}} \times \left[\left(\frac{-0.3915 \left(\frac{1}{2} (4m_{\text{Fe}} + 1m_{\text{H}} + 4m_{\text{SO}_4} + 1m_{\text{HSO}_4}) \right)^{\frac{3}{2}}}{\left(1 + 1.2 \sqrt{\frac{1}{2} (4m_{\text{Fe}} + 1m_{\text{H}} + 4m_{\text{SO}_4} + 1m_{\text{HSO}_4})} \right)} \right) \right. \\
+ \left(m_{\text{Fe}} m_{\text{SO}_4} \left\{ \begin{array}{l} 0.2568 + 3.063 \exp^{-1.4 \sqrt{\frac{1}{2} (4m_{\text{Fe}} + 1m_{\text{H}} + 4m_{\text{SO}_4} + 1m_{\text{HSO}_4})}} \\ -42 \exp^{-12 \sqrt{\frac{1}{2} (4m_{\text{Fe}} + 1m_{\text{H}} + 4m_{\text{SO}_4} + 1m_{\text{HSO}_4})}} \\ + (0.0209) \{ 2m_{\text{Fe}} + 1m_{\text{H}} + 2m_{\text{SO}_4} + 1m_{\text{HSO}_4} \} \end{array} \right\} \right) \\
+ m_{\text{Fe}} m_{\text{HSO}_4} \left(\left\{ 0.4273 + 3.48 \exp^{-1.4 \sqrt{\frac{1}{2} (4m_{\text{Fe}} + 1m_{\text{H}} + 4m_{\text{SO}_4} + 1m_{\text{HSO}_4})}} \right\} + 0 \right) \\
+ \{ m_{\text{H}} m_{\text{SO}_4} (0.0280 + 0.0411 \{ 2m_{\text{Fe}} + 1m_{\text{H}} + 2m_{\text{SO}_4} + 1m_{\text{HSO}_4} \}) \} \\
+ \{ m_{\text{H}} m_{\text{H,SO}_4} \left(\left\{ 0.2106 + 0.5320 \exp^{-1.4 \sqrt{\frac{1}{2} (4m_{\text{Fe}} + 1m_{\text{H}} + 4m_{\text{SO}_4} + 1m_{\text{HSO}_4})}} \right\} + 0 \right) \} \\
+ (m_{\text{Fe}} m_{\text{H}} [(m_{\text{HSO}_4} \times 0.0143)]) + 0 \left. \right]$$

The activity of water ($a_{\text{H}_2\text{O}}$) can be determined from the osmotic coefficient using the following equation:

$$\ln a_{\text{H}_2\text{O}} = -\frac{W}{1000} \left(\sum_i m_i \right) \phi$$

where W is the molecular weight of water (18.016) and $\sum_i m_i$ is the sum of the molar concentrations of ferrous iron, hydrogen ion, sulfate, and bisulfate.

**Chapter 3 : EFFLORESCENT IRON SULFATE MINERALS:
PARAGENESIS, RELATIVE STABILITY, AND ENVIRONMENTAL IMPACT.**

ABSTRACT

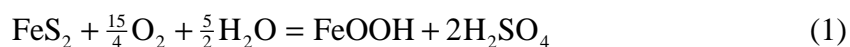
This study of a pyrrhotite-dominated massive sulfide deposit in the Blue Ridge province in southwestern Virginia shows that sulfate minerals formed by the oxidation of the pyrrhotite transform from one to another by a combination of oxidation, dehydration, and neutralization reactions. Significant quantities of sulfate minerals were found in two areas: in the underground adits (area I) and under overhangs along the high sidewall (area II). Samples from this site were analyzed in the laboratory to determine mineralogy, equilibrium relative humidity, chemical composition, and acid generation potential.

In the rock, pyrrhotite oxidizes to marcasite + melanterite, which eventually oxidizes to melanterite + sulfuric acid. Melanterite is extruded from the rocks as a result of the ΔV_r and accumulates in piles where halotrichite, copiapite, and fibroferrite form. In the rock by area II, the melanterite dissolves, and migrates to an exposed pit face where rozenite forms from the evaporating solutions. The rozenite falls into a pile at the base of the wall where melanterite, copiapite, and halotrichite are found. The observed paragenesis can be explained using the $\log a_{\text{O}_2} - \log a_{\text{H}_2\text{O}}$ diagram we developed from published thermodynamic data and observations of coexisting phases.

Dissolution experiments showed that fibroferrite-rich samples had the highest acid producing potential, followed by copiapite-rich samples and then halotrichite-rich samples. The most abundant metals in solutions produced by dissolving the salts were magnesium, aluminum, zinc, copper, calcium, and lead. The molar concentrations of the metals varied with mineralogy. However, all of these minerals release metals and acid when they dissolve and therefore represent a significant environmental threat.

INTRODUCTION

Acid mine drainage (AMD) environments provide of a rich tapestry of mineralogy and geochemistry. Some AMD minerals such as pyrite, goethite, and copiapite, are common and well known, while others like osarizawaite ($\text{PbCuAl}_2(\text{SO}_4)_2(\text{OH})_6$) are obscure and rare. Although the heterogeneity and complexity of AMD systems can make their study difficult, we expect them to show a systematic pattern of mineral paragenesis. Knowledge of this paragenesis is important for quantifying the environmental impact of the minerals, predicting the evolution of AMD sites, and identifying efficient AMD remediation methods. The problem is best addressed by considering only reactions involving the most important elements in AMD: iron, sulfur, oxygen, and hydrogen. The important acid mine drainage minerals can be grouped in three types: iron sulfides, iron sulfates, and iron oxyhydroxides. The overall AMD process begins with the oxidation of iron sulfides and ends with the precipitation of iron oxyhydroxides and the release of sulfuric acid to receiving waters. For pyrite and marcasite, the overall reaction is:



and for pyrrhotite the overall reaction is:



Iron sulfide and iron oxyhydroxide geochemistry have been well studied (see Nordstrom and Alpers, 1999, and references therein for a review), but the equally important iron sulfate phases are less well understood. The object of this study is to establish the paragenesis of some important iron sulfate minerals found in AMD environments.

Numerous hydrated iron sulfate minerals are reported to occur in AMD environments (Table 1) and their mineralogy and geochemistry are included in a recent review by Jambor et al. (2000). Efflorescent iron sulfate minerals are common in base metal deposits, coal deposits, and tailings and waste rock piles where they frequently are associated with oxidizing iron sulfide

minerals. Because of their high solubility, most iron sulfate minerals only persist under rock overhangs and similar sheltered sites where they are protected from dissolution during rain events. They can also form in the open during drier times as sulfate-rich solutions migrate to the surface and evaporate.

Sulfate minerals form when iron sulfate-sulfuric acid rich solutions evaporate. The evolution from ferrous sulfate minerals to iron oxyhydroxide minerals occurs by a series of oxidation, dehydration, and neutralization reactions. The mineralogy that develops at any particular site will be controlled by the relative rates of each of these types of reactions. Although all of the minerals in Table 1 (and more) have been observed, we can predict the order in which the minerals are likely to form by examining their stoichiometries in light of these three reaction types. The axes of Figure 1, based on the atomic ratios of chemical constituents, are designed to show how the minerals are related by oxidation, neutralization, and dehydration reactions. The oxidation axis expresses the amount of positive charge provided by ferric iron divided by the total cationic charge. This number increases when ferrous iron oxidizes to ferric iron. The neutralization axis expresses the ratio of anionic charge provided by hydroxide to the total charge provided by all anions. This number increases as minerals incorporate hydroxide from solution or as sulfate is lost to solution as H_2SO_4 . The dehydration axis expresses the number of moles of water molecules per total moles of positive charge. This ratio decreases as water is lost by dehydration. The heavy arrow shows the general trend of compositions as ferrous sulfates evolve to iron oxyhydroxides. The diagram explains why minerals like lausenite (lau) are relatively rare because they only form in very acid environments. More common minerals, like copiapite (cop), fall near the most direct path leading from melanterite (mel) to goethite (goe). By examining the geochemistry, mineralogy, and occurrence of these phases, we can begin to map out the important reactions that result in the overall transformation processes.

Table 3-1. Minerals that occur in the system Fe-S-O-H and are found in acid mine drainage environments. The abbreviations are used in subsequent figures and tables in this paper. The assessment of the relative abundance of each phase is based on the Authors' observation and literature reviews.

Name and Abbreviation		Formula	Relative Abundance
Hematite	hem	$\text{Fe}^{\text{III}}_2\text{O}_3$	common
Goethite	goe	$\text{Fe}^{\text{III}}\text{OOH}$	common
Ferrihydrite	ff	$\text{Fe}^{\text{III}}(\text{OH})_3$	common
Quenstedtite	quen	$\text{Fe}^{\text{III}}_2(\text{SO}_4)_3 \cdot 10\text{H}_2\text{O}$	somewhat common
Coquimbite	coq	$\text{Fe}^{\text{III}}_2(\text{SO}_4)_3 \cdot 9\text{H}_2\text{O}$	somewhat common
Paracoquimbite	pcoq	$\text{Fe}^{\text{III}}_2(\text{SO}_4)_3 \cdot 9\text{H}_2\text{O}$	rare
Kornelite	korn	$\text{Fe}^{\text{III}}_2(\text{SO}_4)_3 \cdot 7\text{H}_2\text{O}$	rare
Lausenite	laus	$\text{Fe}^{\text{III}}_2(\text{SO}_4)_3 \cdot 6\text{H}_2\text{O}$	rare
Hohmannite	hoh	$\text{Fe}^{\text{III}}_2(\text{SO}_4)_2(\text{OH})_2 \cdot 7\text{H}_2\text{O}$	rare
Metahohmannite	mhoh	$\text{Fe}^{\text{III}}_2(\text{SO}_4)_2(\text{OH})_2 \cdot 3\text{H}_2\text{O}$	rare
Fibroferrite	fib	$\text{Fe}^{\text{III}}(\text{SO}_4)(\text{OH}) \cdot 5\text{H}_2\text{O}$	somewhat common
Amarantite	amar	$\text{Fe}^{\text{III}}(\text{SO}_4)(\text{OH}) \cdot 3\text{H}_2\text{O}$	rare
Butlerite	but	$\text{Fe}^{\text{III}}(\text{SO}_4)(\text{OH}) \cdot 2\text{H}_2\text{O}$	rare
Parabutlerite	pbut	$\text{Fe}^{\text{III}}(\text{SO}_4)(\text{OH}) \cdot 2\text{H}_2\text{O}$	rare
Bilinite	bil	$\text{Fe}^{\text{II}}\text{Fe}^{\text{III}}_2(\text{SO}_4)_4 \cdot 22\text{H}_2\text{O}$	very rare
Römerite	röm	$\text{Fe}^{\text{II}}\text{Fe}^{\text{III}}_2(\text{SO}_4)_4 \cdot 14\text{H}_2\text{O}$	rare
Copiapite	cop	$\text{Fe}^{\text{II}}\text{Fe}^{\text{III}}_4(\text{SO}_4)_6(\text{OH})_2 \cdot 20\text{H}_2\text{O}$	common
Ferricopiapite	fcop	$\text{Fe}^{\text{III}}_5\text{O}(\text{SO}_4)_6\text{OH} \cdot 20\text{H}_2\text{O}$	common
Melanterite	mel	$\text{Fe}^{\text{II}}\text{SO}_4 \cdot 7\text{H}_2\text{O}$	common
Ferrohexahydrite	fhex	$\text{Fe}^{\text{II}}\text{SO}_4 \cdot 6\text{H}_2\text{O}$	very rare
Siderotil	sid	$\text{Fe}^{\text{II}}\text{SO}_4 \cdot 5\text{H}_2\text{O}$	very rare
Rozenite	roz	$\text{Fe}^{\text{II}}\text{SO}_4 \cdot 4\text{H}_2\text{O}$	common
Szomolnokite	szo	$\text{Fe}^{\text{II}}\text{SO}_4 \cdot \text{H}_2\text{O}$	somewhat common
Rhomboclase	rhom	$\text{H}_3\text{OFe}^{\text{III}}(\text{SO}_4)_2 \cdot 3\text{H}_2\text{O}$	somewhat common
Borgstromite	borg	$\text{H}_3\text{OFe}^{\text{III}}_3(\text{SO}_4)_2(\text{OH})_6$	somewhat common
Schwertmannite	sch	$\text{Fe}^{\text{III}}_{16}\text{O}_{16}(\text{OH})_{12}(\text{SO}_4)_2$	somewhat common

A knowledge of the sulfate mineralogy and its progression at an AMD site is important because different sulfate minerals carry different amounts of trace elements and produce different amounts of acid upon dissolution. The dissolution of iron sulfate minerals during rain events can dramatically affect aquatic ecosystems. Dagenhart (1980) showed a very clear relationship between stream discharge and stream chemistry during rain events (Fig. 2). His data show that during the initial phase of a rain event, there was a marked decrease in pH and an increase in dissolved solids as iron sulfate minerals dissolved and the acid sulfate solutions were carried by overland flow into the stream. With time, the pH rises and the dissolved solids decline as the water draining the sulfate rich area is diluted by cleaner water from upstream. During a later storm event, no significant change in water chemistry is observed because the soluble sulfates have been washed away by earlier events. Bayless and Olyphant (1993) and Alpers et al. (1994) observed changes in sulfate mineral chemistry as a result of wet and dry periods. Keith et al. (1999) and Keith et al. (2001) reported that iron sulfate minerals accumulate during dry periods and that their rapid dissolution during the first rain in the wet season released high concentrations of metals into local streams. In addition, they noted that the degree of trace element and acid release could be related to the mineralogy of the iron sulfates. Stewart et al. (1997) observed similar effects using leaching column in a laboratory setting. They found that coal wastes with a 4% pyritic sulfur content produced enhanced acidity, and iron and sulfate concentrations when the columns were leached after long periods of drying and efflorescent salts had formed. These laboratory and field studies provide evidence that the dissolution of iron sulfate phases can rapidly contribute acid and metals to receiving waters upon dissolution.

Another effect of the dissolution of iron sulfate minerals is the promotion of pyrite oxidation. Ferric iron oxidizes pyrite faster in aqueous systems than does dissolved oxygen (McKibben and Barnes, 1986; Williamson and Rimstidt, 1994). However, at low pH, the

oxidation rate of ferrous iron is slow (Singer and Stumm, 1970). The dissolution of ferric-rich sulfate minerals near the top of the waste piles can release ferric iron solutions that will infiltrate the wastes where they will cause pyrite oxidation at deep levels where oxygen cannot penetrate. Therefore, the dissolution of ferric sulfate minerals creates a positive feedback mechanism for the further generation of acid mine drainage (Cravotta, 1994).

Because of the importance of iron sulfates minerals in AMD, there have been a number of field and laboratory studies of their paragenesis (Bandy, 1938; Bol'shakov and Ptushko, 1971; Zodrow et al., 1979; Nordstrom and Alpers, 1999). Generally, phases have been observed to 1) evolve from all ferrous iron to mixed ferrous/ferric iron to all ferric iron phases and 2) dehydrate via the loss of structural water. Jambor and others (2000) have compared the results of some field and laboratory paragenetic sequences as summarized in Table 2.

Table 3-2. Observed paragenesis of sulfate minerals (from Jambor et al., 2000)

	Alcaporrosa, Chile	Laboratory	Iron Mountain, CA
	Bandy 1938	Buurman, 1975	Nordstrom & Alpers 1999
<i>early</i>	pyrite	pyrite	pyrite
		melanterite	
		siderotil	
		rozenite	rozenite
	szomolnokite	szomolnokite	szomolnokite
	römerite	rhomboclase	copiapite
	quenstdtite		römerite
	coquimbite	coquimbite	coquimbite
	pickeringite	römerite	kornelite
	copiapite		rhomboclase
	parabutlerite	voltaire	voltaite
<i>late</i>	jarosite		halotrichite-billinite

We are building on the results of previous studies of the paragenesis of sulfate minerals and their environmental impact. The purpose of this paper is to report our analysis of the

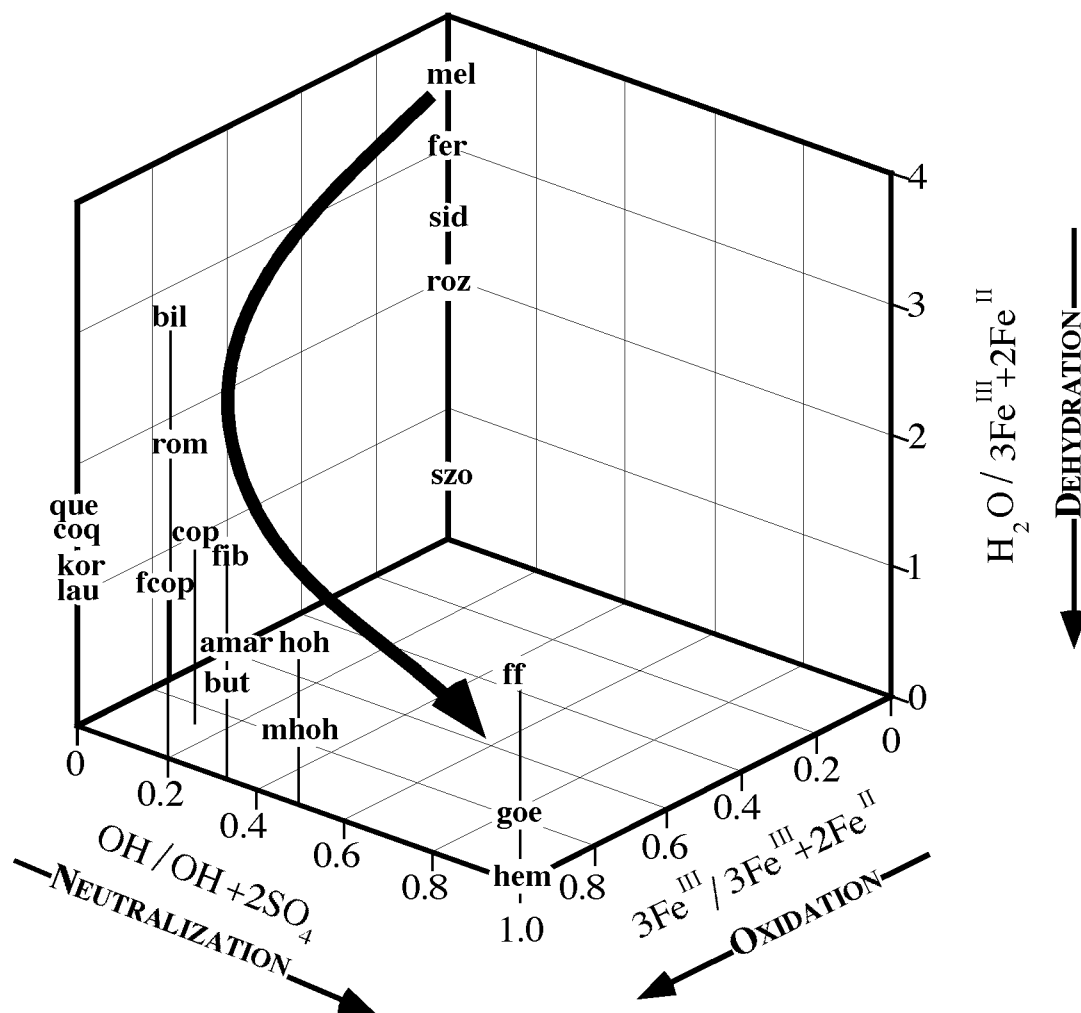


Figure 3-1. The stoichiometry of iron sulfate and iron oxide minerals found in acid mine drainage environments are directly related to the reactions that transform one phase into another. Mineral abbreviations are given in Table 1. Changes in the ratio along the axes correspond to processes observed in acid mine drainage environments, specifically (z) dehydration, (y) neutralization, and (x) oxidation. The bold line shows a generalized reaction path involving these three processes that converts ferrous sulfates to iron oxyhydroxides. Minerals that plot close to the line are commonly found in acid mine drainage areas whereas those with extreme ratios are likely to be uncommon to rare.

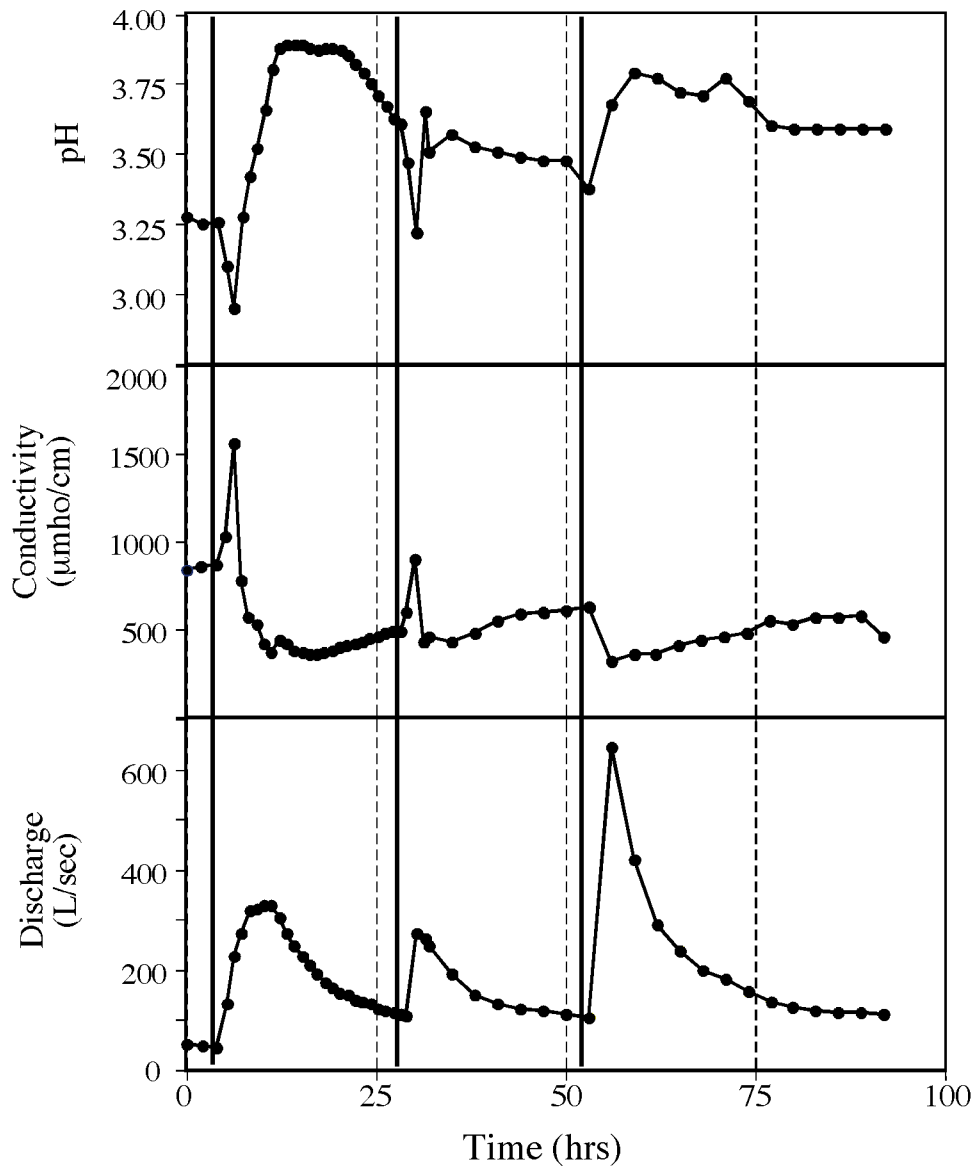


Figure 3-2. Hydrograph of Contrary Creek, VA showing the relationship between stream discharge and stream chemistry for rain events in June, 1978 (Dagenhart, 1980). The bold vertical lines represent rain events. Runoff from the first storm event dissolved sulfate minerals and carried the resulting acidic, sulfate-rich solution to the stream, causing an increase in acidity and conductivity. After a short time, relatively fresher water from upstream diluted the stream. Later storm events produce smaller excursions in conductivity and pH because the sulfate minerals had been previously washed away.

paragenesis of sulfate minerals occurring at a pyrrhotite-dominated massive sulfide deposit based on our interpretation of the relative stability of the iron sulfate minerals. In addition, we evaluate some aspects of the environmental impact of the minerals found at this site.

METHODS

Field Methods

Site Description. The field site for this study is an abandoned mine located in the Blue Ridge province in southwestern Virginia (Fig. 3). The mine is located at the southern end of the Great Gossan Lead, which is a 28 km-long discontinuous mineralized zone that trends to the northwest from a point approximately 6 km north of Galax, VA to 10 km north of Hillsville, VA. The Gossan Lead consists of irregular pod and veinlike bodies of massive pyrrhotite, the long dimensions of which are approximately parallel to the NNE-SSW foliation of the host rocks (Stose and Stose, 1957; Henry et al., 1979). A comprehensive review of the economic geology of the Gossan Lead is found in Gair and Slack (1984).

The Gossan Lead is located in the Precambrian Ashe formation. The primary mineralogy consists of fine-grained sulfidic metagraywaske, gritty metagraywacke, and sulfidic to graphitic phyllite (Rankin et al., 1973). In addition, a petrologic study by Staten (1976) found this part of the Ashe to be dominantly quartz-muscovite schist and gneiss with minor amounts of hornblende gneiss, hornblende amphibolite, biotite schist, chlorite schist, biotite-chlorite gneiss, biotite-chlorite schist, and calcareous rock. Gair and Slack (1984) prefer the term granofels to gneiss because the rocks in the vicinity of the massive sulfide deposits lack the typical layering of high grade metamorphic rocks. The primary sulfide minerals are pyrrhotite (over 90% of the sulfide mass) with minor sphalerite and chalcopyrite (Staten, 1976; Craig et al., 1978; Henry et al., 1979; Craig, 1980). Henry et al. (1979) identified the pyrrhotite to be the intermediate hexagonal variety ($\text{Fe}_{0.9}\text{S}$). Pyrite is very rare to absent in most of the Gossan Lead, but increases in

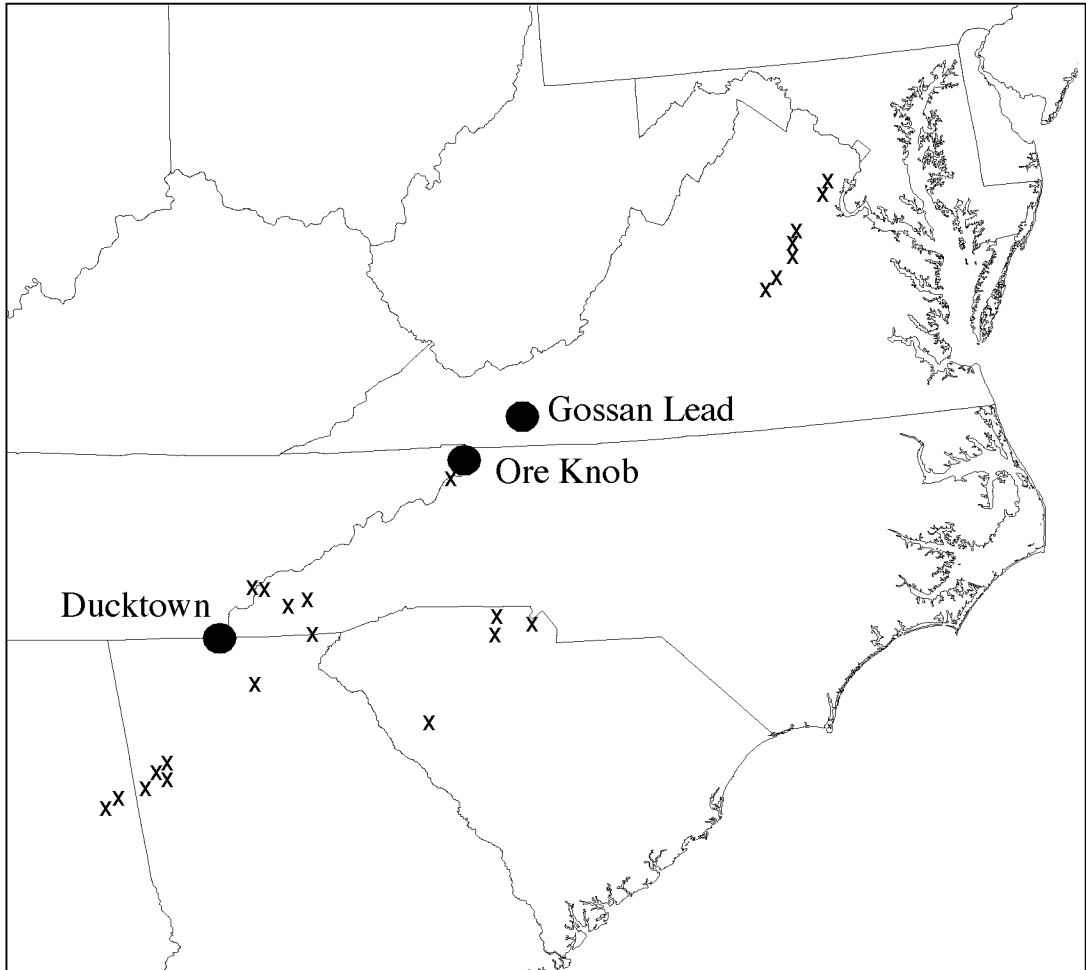


Figure 3-3. Location of the Gossan Lead in Southwestern Virginia. Also shown are the locations of other major (circle) and minor (x) massive sulfide deposits.

abundance towards the Betty Baker Mine in the northeast. Additional ore minerals reported by Henry et al. (1979) include trace amounts of galena, arsenopyrite, cubanite, macakinawite, tetrahedrite, stannite, native bismuth, rutile, ilmenite, and graphite. The samples and field observations made for this study were from the Bumbarger-Iron King deposit in Iron Ridge segment of the Great Gossan Lead. Iron Ridge is located at the southwestern end of the Lead, approximately 6 km north of Galax, VA. The Iron Ridge segment was the only area of the Gossan Lead that was mined for primary sulfides and the only deposits to have been mined since 1908 (Gair and Slack, 1984). This segment is 2 km long and contains three major deposits: the Huey, the Gossan Howard, and the Bumbarger-Iron King.

In 1998, the entrance to the Bumbarger was regraded and some of the tailings were removed. However, the main pit and underground adits have not been remediated and therefore the most of the mine was accessible. We chose to sample from the Bumbarger-Iron King mine because 1) we could gain access, 2) the mining history, ore mineralogy, and economic geology of the area has been documented (Stose and Stose, 1957; Henry et al. 1979; Gair and Slack, 1984), and 3) there is a great abundance of sulfate minerals available for study. The Bumbarger-Iron Ridge mine was mapped and described by Gair and Slack (1984) and is shown in Figure 4. The Bumbarger was first mined by open pit methods. The pit is oblong, approximately 100 meters long, 60 meters across, and 40 meters deep. A crowfoot-shaped bench divides the pit into three sections. In 1935, mining extended underground to the Iron King portion of the deposit (Henry et al., 1979). The openings of the underground portions are large adits. They are dark, cool, and damp. Drifts extend underground from the large front opening but were not explored during this study. Direct hydrologic communication is likely among the various drifts.

The water content of the pit varies by season. The average precipitation for the area is approximately 7.6 cm/month and the average temperature highs and lows are 28°/-6°C, respectively. Two pools of AMD occur on the floor of the Bumbarger Pit. One is ephemeral and

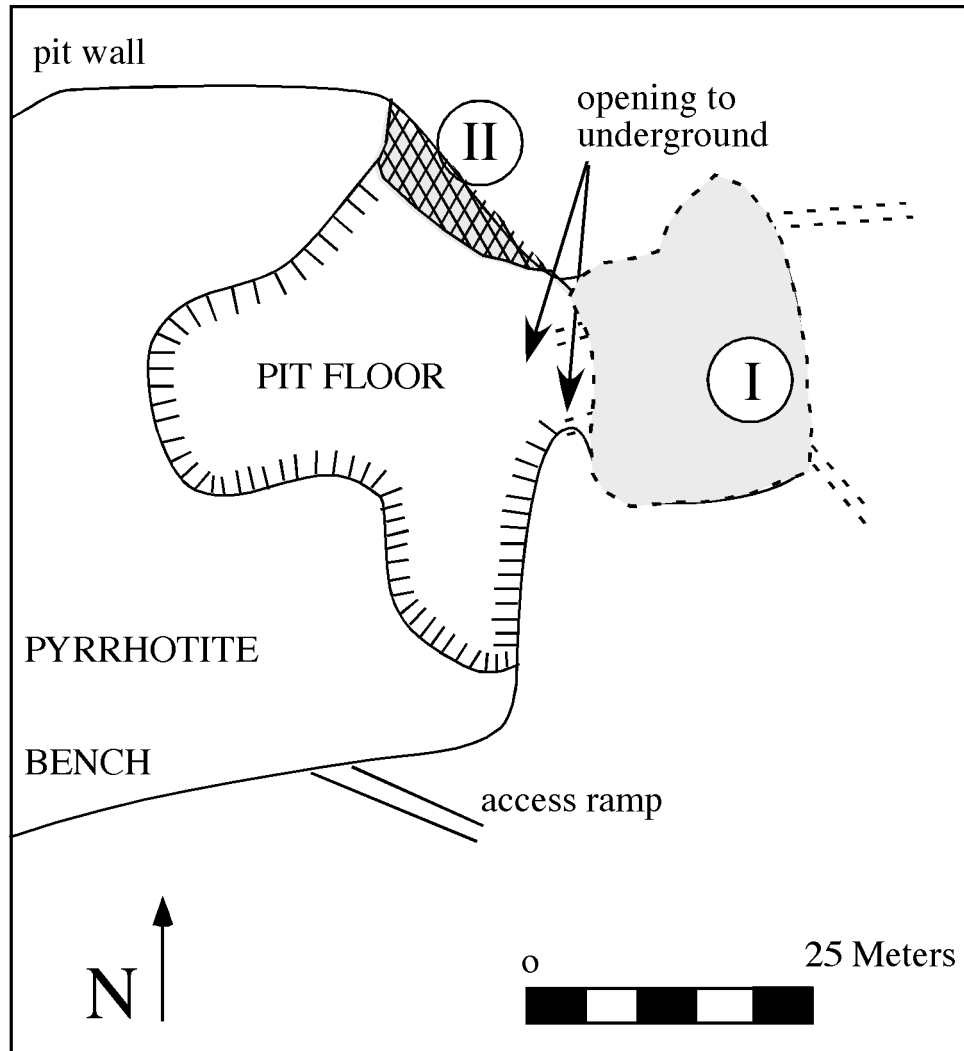


Figure 3-4. Map of a portion of the Bambarger-Iron King mines in the Iron Ridge segment of the Gossan Lead. The two sampling areas, I and II, are indicated on the map. The dashed line around area I indicates the boundary of the underground workings. The crosshatching at area II indicates the overhang of the side-wall.

one permanent. The permanent pool is present in the deepest part of the pit near an underground opening. The underground adits have a higher relative humidity than the open area of the mine. Water drips from the roof of the adits year-round, but there is not sufficient water flow through these areas to dissolve the sulfate minerals that are present.

Sampling Protocol Significant quantities of sulfate minerals were found in two areas: in the underground adits (Area I) and under overhangs along the high sidewall (Area II). Sampling locations for areas I and II are indicated on Figure 4. At each site, trenches were made through representative piles. Samples were collected from the wall or roof, the surface the pile, and at various depths in each trench. Samples were collected during several trips during the summer of 2001.

Laboratory Methods

Samples brought back to the laboratory were analyzed to determine mineralogy, equilibrium relative humidity, chemical composition, and acid generation potential. Samples were stored in air tight bags and analyses commenced soon after collection to assure that the samples did not change in response to the environmental conditions in the laboratory.

Mineralogical Analysis. Each sample was subsampled based on visual differences, primarily color, using a binocular microscope. In most cases, the samples were very fine grained, and it was nearly impossible to isolate to pure individual phases. However, using this method, the subsamples consisted of a few predominant phases.

The mineralogy of the subsamples was identified using X-ray diffraction (XRD) with Cu K-alpha radiation. Samples were ground in an agate mortar and pestle, suspended in benzene, and mounted on zero-background quartz plates. Each sample was scanned between 4 and 80 degrees 2Θ at a scan rate of 1° per minute. Selected samples were reanalyzed to determine if the mineralogy changed upon sample aging. Minerals were identified by comparing the diffraction pattern of the unknown against patterns for known minerals published by JCPDS (PDF, 2000).

In addition to XRD analysis on the mineral separates, bulk samples and insoluble fractions were analyzed in powder mounts. These analyses were also performed using the same XRD conditions as the mineral separates. These patterns were compared to the mineral separate patterns to better refine the identification.

In many cases, interpretation of the X-ray diffraction pattern was difficult because of the chemical complexity of samples from this site and the high degree of alteration of the sulfide and silicate phases. In addition, the complex structure of the sulfate phases yield numerous peaks. Mixtures of even two or three of these phases create a very complex diffraction pattern. Therefore, microscopic techniques (both petrologic and scanning electron) were used to assist with phase identification. The morphology and some chemistry of the minerals was determined with scanning electron microscopy (SEM) and the chemical composition of selected phases was determined with energy dispersive spectroscopy (EDS). Both traditional and field emission SEMs were used in this study.

Humidity Buffer Method. Most iron sulfate minerals contain waters of hydration in their crystal structure. The number of waters of hydration, and therefore the mineralogy, of the phase is sensitive to changes in environmental relative humidity and temperature. We performed experiments to determine the equilibrium relative humidity of selected subsamples. To do this, we used a modified version of the humidity buffer method of Chou et al. (2002). In this method, samples were placed in humidity buffered chambers and changes in sample weight were recorded over time.

Humidity buffers were based on various saturated salt solutions (Table 3), which were prepared by placing 30 g of the salt and 5 g of water into a plastic vial. In all cases, this amount was sufficient to create a saturated solution with some solid present.

Table 3-3. Salts used to make saturated solution for humidity buffer method (Young, 1967; Greenspan, 1977). The relative humidity values are reported for 25°C.

Saturated Solution	Buffered Relative Humidity
CuSO ₄ ·5H ₂ O	97.20%
BaCl ₂ ·2H ₂ O	90.30%
(NH ₄) ₂ SO ₄	80.20%
SnCl ₂ ·6H ₂ O	70.85%
CoCl ₂	64.92%
NaBr·2H ₂ O	58.20%
Mg(NO ₃) ₂ ·6H ₂ O	52.82%

When solutes are added to water the $a_{\text{H}_2\text{O}}$ is reduced from a value of 1.0 (pure water) and the partial pressure of water in the vapor phase decreases proportionally to $a_{\text{H}_2\text{O}}$ in solution. In this paper, we use pure liquid water as a reference state ($a_{\text{H}_2\text{O}}=1.0$) so that the relative humidity (100%) can be directly compared with the activity of water in solution (relative humidity = $a_{\text{H}_2\text{O}} \times 100\%$). Note that Chou et al. (2002) use ideal water vapor at 1 bar pressure as a reference state. These two reference states are related through the reaction:



which has a $\log K = 1.49$. The partial pressure of pure water at 25°C is 0.0031691 bar. For example, for saturated solutions of CuSO₄·5H₂O at 298K, $a_{\text{H}_2\text{O}}=0.972$ and $P_{\text{H}_2\text{O}}=(0.972)(0.0031691)$ bar so that $a_{\text{H}_2\text{O}}=0.972$ for the pure liquid water reference state that we use corresponds to an $a_{\text{H}_2\text{O}}=0.0030804$ in the ideal water vapor at 1 bar reference state that Chou et al. (2002) uses. At saturation, the concentration of the salt is fixed and therefore, the $a_{\text{H}_2\text{O}}$ in each of these solutions is fixed. Hence, the activity of water in the solution is known and the relative humidity (partial pressure of water) in the vapor phase inside the cell is also known.

Two grams each of the field samples that contained a sulfate phase of interest were placed inside a preweighed glass vial (Fig. 5). The glass vial was then placed inside a second glass vial in the humidity buffer container. The second glass vial kept the sample vial from

contacting the saturated salt solution. The container was sealed and placed in a constant temperature bath set at 25°C. The sample was removed from the cell and reweighed after 7-10 days, when the weight change pattern for the minerals had been established.

Graphs of the weight change versus the buffered relative humidity for each sample showed whether samples had gained weight by absorbing water from the atmosphere inside the sealed container or lost weight as the sample dehydrated. The point at which the sample neither gained nor lost weight was selected as the sample's equilibrium relative humidity, i.e. the point on the graph where the weight change curve crossed the x-axis.

For example, Figure 6 shows a graph of weight change versus relative humidity for the sample that was dominantly fibroferrite. At high relative humidity (97%), the sample absorbed water from the atmosphere and deliquesced. At lower relative humidities (all buffers lower than 80%), the sample lost weight from drying of the adhering iron sulfate-sulfuric acid solution. At a relative humidity of 88%, the sample neither gained nor lost weight. Therefore, fibroferrite and the coexisting iron sulfate-sulfuric acid solution are stable in atmospheres that have a relative humidity at or near 88%.

Acid Generation Potential and Chemical Composition of Sulfate Mineral Samples.

Previous workers noted that the dissolution of the sulfate minerals during rain events can produce acidic, trace-element-enriched sulfate solutions that can dramatically degrade receiving waters (Dagenhart 1980; Bayless and Olyphant, 1993; Jerz, 1998). We performed dissolution experiments of field gathered specimens to determine the acid generation and metal release potential of some of the mineral samples collected from our field site.

For each experiment, a known weight of sample was dissolved in a known volume of deionized water in preweighed, acid washed centrifuge tubes. Specific water:mineral ratios varied depending on the amount of sample available, but were typically 100 mL:15 g. The

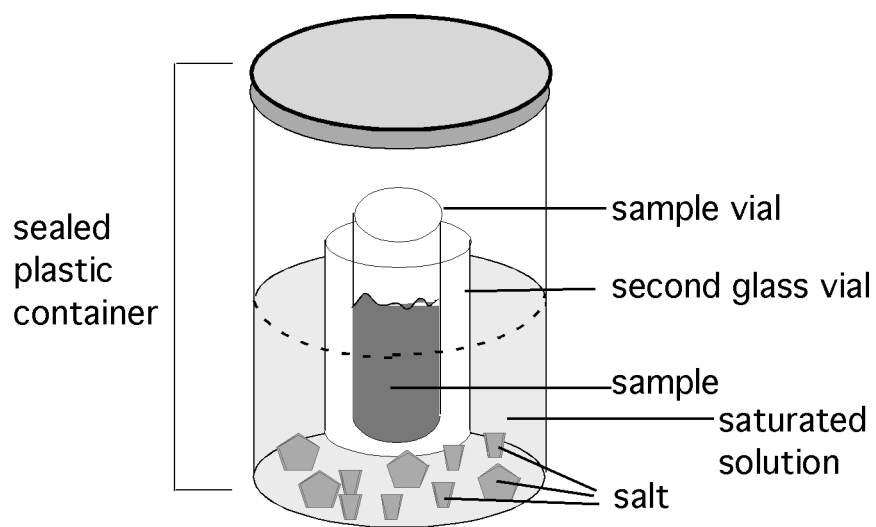


Figure 3-5. Schematic of humidity buffer method. The relative humidity ($a_{\text{H}_2\text{O}}$) in the sealed container is buffered by the saturated salt solutions listed in Table 3. Field samples were placed in a glass vial inside the chamber.

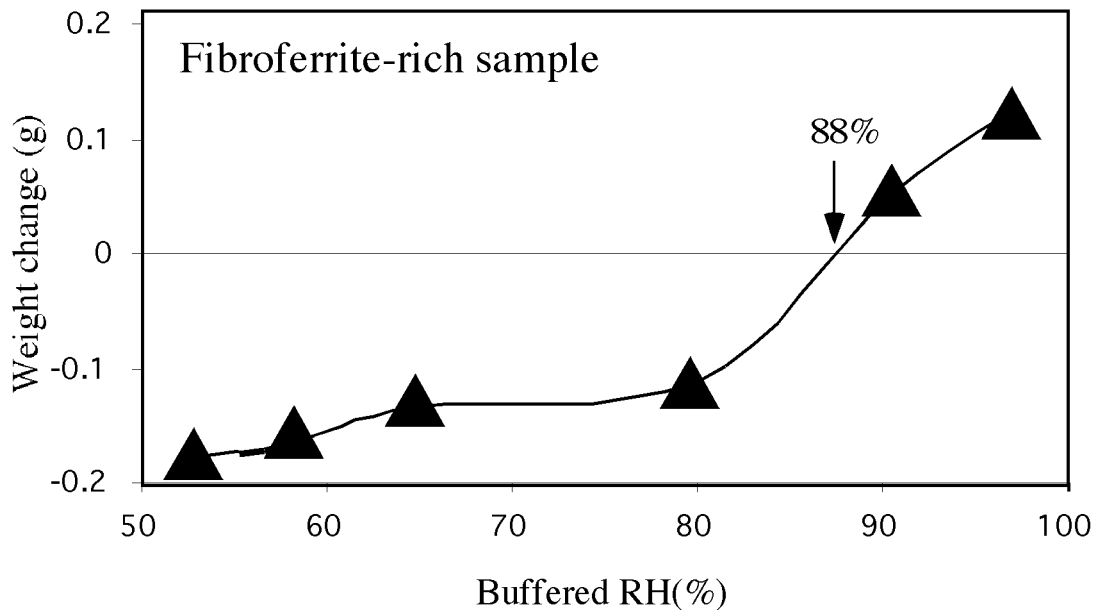


Figure 3-6. Example of the data collected with the humidity buffer method. The change in the weight of the a 2-gram fibroferrite sample equilibrated with a vapor phase of fixed RH for 7 days was plotted versus the relative humidity. Samples that gained weight absorbed water from the vapor phase; samples that lost weight dehydrated and released water to the vapor phase. The intersection of the line with x-axis (change in weight = 0) is the relative humidity at which the sample is stable.

solutions were stirred for 1 minute before the tubes were centrifuged at 158x g for 10 minutes and decanted into an acid washed beaker. The residium was dried and weighed to determine the amount of insoluble material in each sample. A 10 mL aliquot was removed from the supernatent diluted 5:1 in a 50 mL volumetric flask before the pH of the supernatant was measured. The pH meter had been previously calibrated at pH = 2 and 4. A 10-mL aliquot of the secondary solution was removed before the pH was measured. The third 10-mL aliquot was diluted 5:1 in another volumetric flask and the above process repeated for a total of 10 dilutions. Half of the most dilute sample was acidified with HCl and saved for ICP-AES analysis. All the solutions were allowed to sit open to the atmosphere for 24 hours and the pH was measured again.

Similar dissolution experiments were performed to determine the metal concentrations of the samples. Known weights of samples were allowed to dissolve in 50 mL of dionized water for 30 minutes before the samples was centrifuged at 158x g for 10 minutes and decanted into an acid washed beaker . The residium was dried and weighed to determine the amount of dissolved material. The concentration of Na, Mg, Si, P, S, K, Ca, Cr, Mn, Fe (total), Co, Ni, Cu, Zn, Pb, Cd, and Al was measured by ICP-AES within a week of their extraction. We assumed that all of the sulfur detected was in the form of sulfate. Ferrous or ferric iron content was estimated by assuming charge balance.

RESULTS

Field Observations

Area I is in a large, cavernous adit. The roof is 7+ meters above the adit floor near the opening from the pit and slopes to a height of approximately 3 meters at the back wall, although it is lower in some places. It is approximately 35 meters across and 20 meters from the opening from the pit to the back wall, although several narrow tunnels extend much further. The surface

of the adit floor is hummocky and most of the floor is covered by sulfate minerals, either in piles or in a veneer. In a few places there is standing water or desiccation cracks in an iron oxide mud, suggesting that pools of water have evaporated. Rarely, bedrock is exposed on the floor. In several places, iron oxyhydroxide stalactites hang from the roof, mostly above areas of standing water.

There are several piles of sulfate minerals in area I (Fig. 7). These appear to have formed beneath pyrrhotite rich zones or pods in the roof. The piles range in size from a meter or less across to several meters across and up to a 1.5 meters deep. The sulfate minerals in the piles are moist to wet. The particles in the piles range in grain size from a few centimeters in diameter to mostly less than a millimeter. In addition, large pieces (>20 cm) of wall rock have fallen and been buried in the piles. The mineralogy of the piles is highly heterogeneous, consisting of mixed sulfate, silicate, sulfide, and iron oxyhydroxide phases. Efflorescent blooms of sulfate minerals occur around the bases of most piles. These blooms are moist and in some cases appear to contain some flow structure. The color of these blooms has fluctuated during our numerous visits to this site, suggesting that the mineralogy changes with environmental conditions.

Area II is located on the sidewall of the pit, a few meters to the northeast of the opening to area I. It has good sun exposure and is usually warm and dry. Sulfate minerals occur beneath an overhang in the side-wall. The sulfate minerals are distinctly different at area II. The sulfate minerals at the surface occur as encrustations or efflorescent blooms. The blooms are usually dry and porous. Many fine "hair salts" coat the surfaces of exposed rocks on the ground or the sulfate blooms. Underneath the top layer, minerals are highly friable and fine grained. Fine grained sulfate minerals also occur on the surface of the side wall. We have also observed the color of the sulfate minerals at area II to fluctuate between visits.



Figure 3-7. Large pile of predominantly sulfate minerals from field site. The dimensions of the pile are approximately 2.5 meters long, 1.5 meters wide, and 1.25 meters deep.

Mineralogy

The minerals identified from the field site and a description and the location of each are listed in Table 4. Most of the samples consisted of a mixture of phases. Our efforts were focused on identifying the dominant sulfate minerals present in the samples. The minerals are not pure, end-member phases. In addition to sulfate phases, we were able to identify some other mineral types, but a detailed mineralogical investigation of the paragenesis of the silicate phases was not a goal of this study.

Table 3-4. Description of the minerals found at the Bumbarger-Iron King mine. The abbreviation I indicates that a mineral was found at area I and II indicates that a mineral was found at area II.

Mineral	Description	Location
Melanterite	Elongate, curved blue green crystals	I: in roof and pile II: bottom of trench
Rozenite	Very fine grained, white crystals	II: along sidewall, in pile
Halotrichite	Fibrous, white masses of (area I) or single (area II) crystals	I: in pile II: at surface
Copiapite	Pale yellow to orange efflorescent blooms; moist and waxy in area I, dry in area II.	I: in pile; along the sides of pile II: at surface
Fibroferrite	Moist, yellow brown efflorescent blooms; some times masses appeared to contain flow structure	I: along the side of pile
Other sulfates	minor jarosite, romerite possible	
Sulfides	Altered pyrrhotite with bird's-eye texture; fine grained pyrite, marcasite, and chalcopyrite	I&II: several places at site
Silicates	Altered actinolite, mica, quartz	I&II: several places at site
Iron oxides	Earthy; amorphous and fine grained	I&II: several places at site

Relative humidity data

Field samples were used in these experiments. Although the samples were selected so they contained predominantly one mineral, other sulfate, silicate, and oxyhydroxide phases were present. Furthermore, some of the samples were damp because of the presence of ferrous

sulfate-sulfuric acid solutions. The results presented here represent the equilibrium relative humidity where each of these complex samples would be stable relative to hydration/dehydration reactions. The equilibrium relative humidity over the pure, end-member minerals is likely to be different than reported for these samples.

The results of the humidity buffer experiment are shown in Figure 8. The fibroferrite-rich sample was found to deliquesce at relative humidities greater than 88%. The halotrichite-rich sample was found to deliquesce at relative humidities greater than 90%. The copiapite-rich sample was found to deliquesce at a relative humidity greater than 80%. Copiapite was found to be stable (i.e. not dehydrate) to a relative humidity of 65%. The melanterite-rich sample was found to deliquesce at relative humidities greater than 82%. Note that this relative humidity is less than the stable relative humidity above a saturated pure water-melanterite solution (96%) (Apelblat, 1993).

Dissolution of minerals

The acid producing potential of each field sample was determined from graphs of pH versus weight percent sample dissolved (Fig. 9). Fibroferrite-rich samples had the highest acid producing potential, followed by copiapite-rich samples and then halotrichite-rich samples. Melanterite-rich samples had the lowest acid producing potential.

Pie charts showing the concentration of some important elements in selected samples is shown in Figure 10. The pie charts were made by dividing the molar concentration of each metal by the sum of the molar concentrations of all metals. For most samples, iron was found to be the dominant metal released upon dissolution. However, the charts show that up to several percent of other metals are released along with iron. For all samples, concentrations of Na, P, Si, K, were found to be insignificant. Concentrations of Pb, Ni, Cr, and Ni were low compared to other metals, but were measurable in almost all samples.

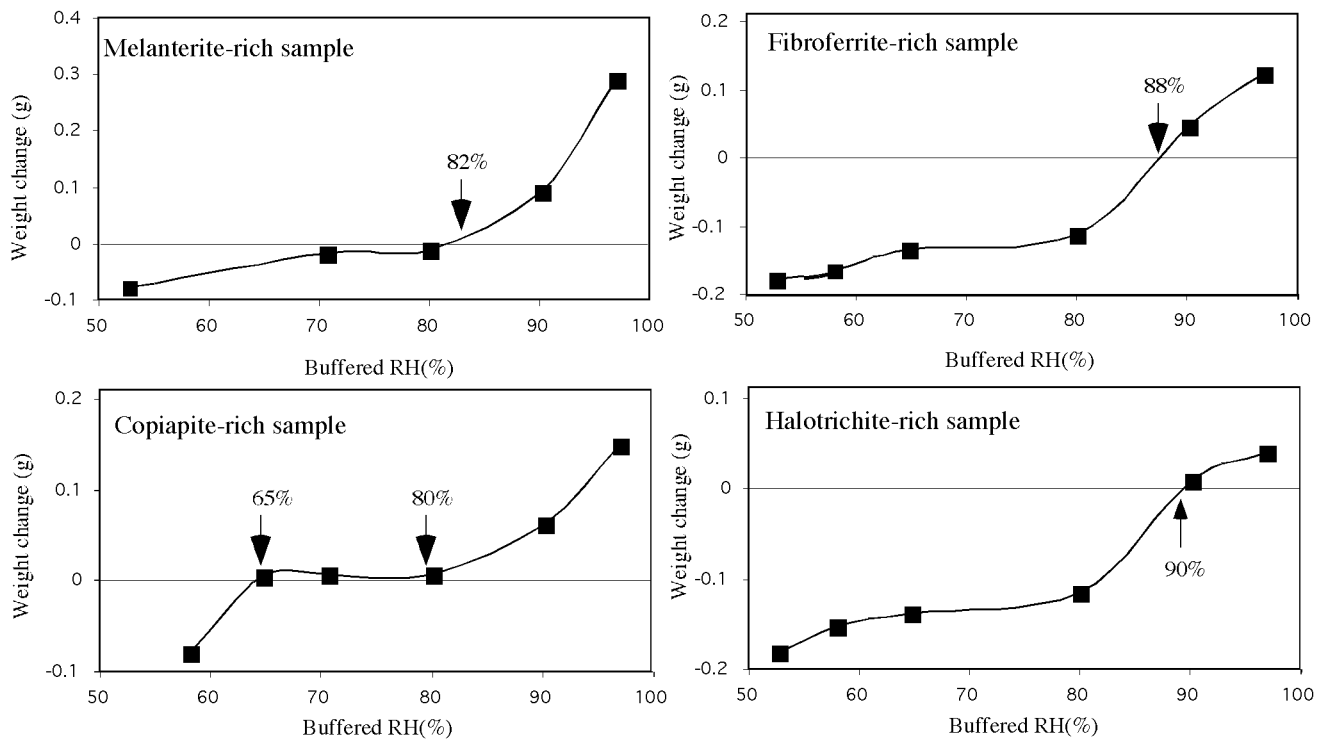


Figure 3-8. Results from humidity buffer method. The melanterite, halotrichite and fibroferrite samples were damp (as collected from the field). Therefore, part of the weight loss for these samples in the low RH experiments is due to the evaporation of these solutions. Each square represents one of the relative humidity buffers listed in Table 3.

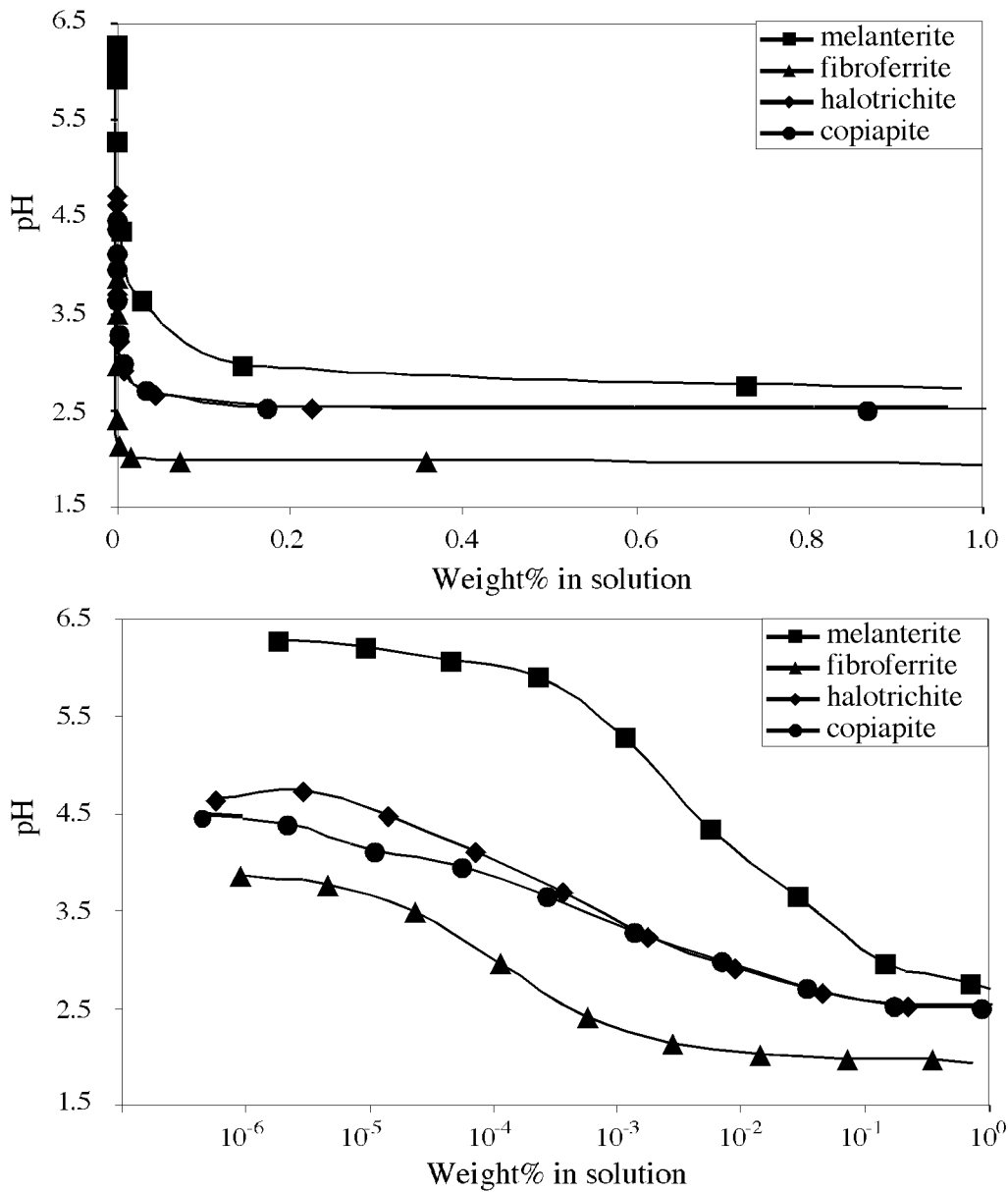
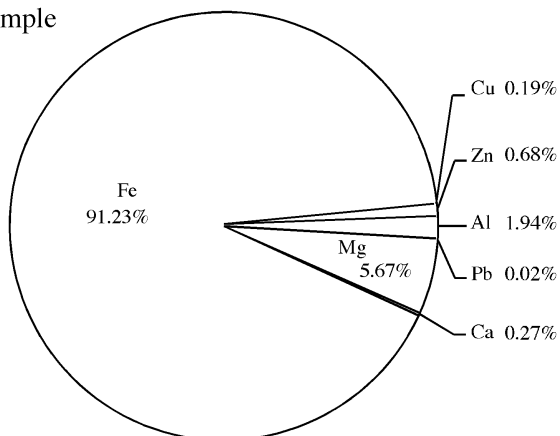
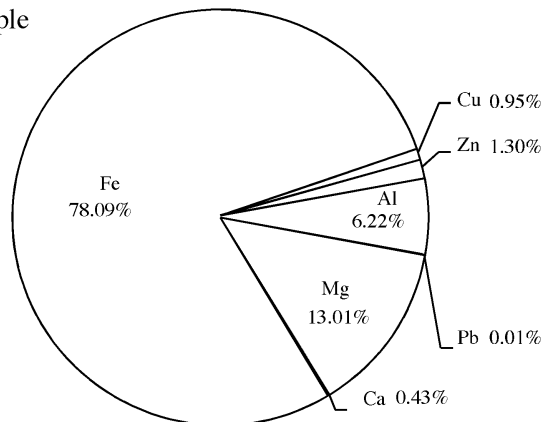


Figure 3-9. Graphs of pH versus mineral weight percent dissolved in solution for selected field samples (dominant mineralogy listed in the legends). The x axis on the lower graph is presented in log scale to magnify the differences in very dilute solutions.

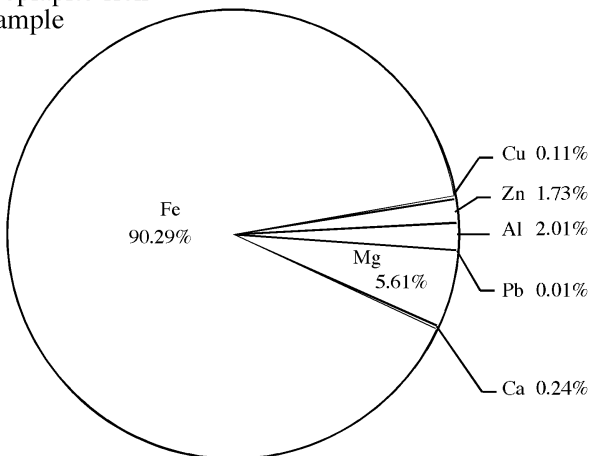
Melanterite-rich sample



Fibroferrite-rich sample



Copiapite-rich sample



Halotrichite-rich sample

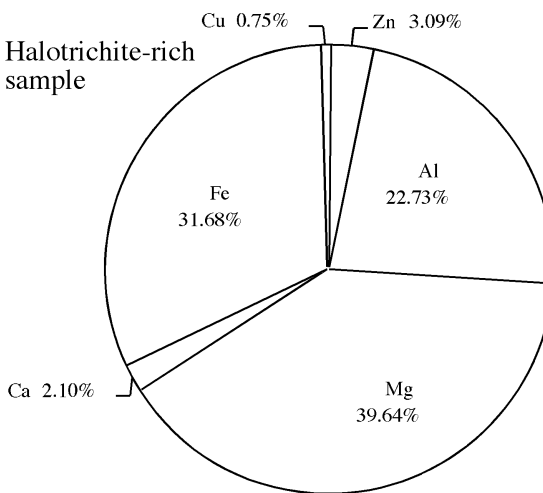


Figure 3-10. The relative cation abundances in solutions produced by dissolving the field samples. Concentrations are in mol % of total metals.

The relative dissolution rates of the sulfate minerals were estimated by weighing the dried, residual material left in the centrifuge tubes after the dissolution experiments. Melanterite, copiapite, and halotrichite had relatively high dissolution rates, and the dissolution rate of fibroferrite was slower.

DISCUSSION

Our observation of the iron sulfate mineralogy at our field site provides a reference case that can be used to understand the paragenesis of sulfate minerals from pyrrhotite-dominated massive sulfide deposits. The paragenesis that we observed is consistent with the stability of various sulfate phases and can be best understood using a $\log a_{\text{O}_2} - \log a_{\text{H}_2\text{O}}$ diagram that we created on the basis of published thermodynamic values and the results of our experiments. Our knowledge of this paragenesis sets the stage for understanding the environmental impact of iron sulfate minerals because the evolving sulfate mineralogy affects the acid and trace element load of runoff solutions.

Paragenesis of Sulfate Phases

The paragenesis of the iron sulfate minerals at each field site can be broken down into three steps (Fig. 11). The temperature and relative humidity of the two sites are different so that the paragenesis path at each site is different. However, we can combine the observations from both sites to create a general paragenesis model for the pyrrhotite dominant system.

At area I, the first step in the paragenesis is the oxidation of pyrrhotite in the roof rocks to create melanterite and sulfuric acid.



In addition, some marcasite forms from the oxidative leaching of pyrrhotite. Some of the sulfuric acid reacts with surrounding silicate or other sulfide minerals to release other cations (e.g. Al^{3+} , Zn^{2+}) into solution. Melanterite produced by this reaction has a much larger molar

volume than pyrrhotite ($V_m(\text{po}) = 16.88 \text{ cm}^3/\text{mol}$, $V_m(\text{mel}) = 146.56 \text{ cm}^3/\text{mol}$) (Robie and Hemmingway, 1995). The melanterite crystals found in the roof were curved and anhedral, which is consistent with the idea that they were extruded into available pore space as they formed. In the second step, the extruded melanterite along with silicate minerals and unreacted sulfide minerals fall to the floor and accumulate into piles. The melanterite continues to oxidize and ferric iron precipitates resulting in a thin film of $\text{Fe}^{\text{II}}\text{-Fe}^{\text{III}}\text{-H}^+\text{-SO}_4^{2-}$ solution on the grains in the pile. In the third step, ferrous sulfate-sulfuric acid solutions drip from the roof onto the pile and this solution combines with the solution film on the grains and migrates to areas where evaporation causes new minerals to grow as efflorescent blooms. These blooms were identified as copiapite, fibroferrite, or halotrichite. The specific mineral that forms is a function of relative humidity and degree of oxidation. Fibroferrite was found when the relative humidity was high, whereas copiapite occurred under drier conditions. Halotrichite was found both in the pile and buried in the material that covered the floor of the adit. In our laboratory experiments, halotrichite was found to be stable at high relative humidities. However, it may precipitate at late stages in the paragenesis because the activity of aluminum becomes high relative to iron as the dissolved iron is removed by the formation of iron sulfate minerals.

At area II, most of the primary material had been oxidized and fresh pyrrhotite was not exposed at the surface of exposed rock. However, we did find essentially unaltered pyrrhotite on the inside of grains in polished section. We believe that the first step of the paragenesis at this site is when meteoric water and oxygen react with the pyrrhotite inside the rocks. The predominantly ferrous sulfate solution produced by pyrrhotite oxidation migrates to the surface of the pit wall where rozenite forms. In the second step, the very fine-grained rozenite falls to the ground where it accumulates in piles. In the pile, some ferrous iron oxidizes to ferric iron. Finally, during wet times, some $\text{Fe}^{\text{II}}\text{-Fe}^{\text{III}}\text{-H}_2\text{SO}_4$ solution forms and migrates to sites of evaporation where copiapite grows as efflorescent blooms. During dry times, the reactions at

area II are probably slow. Halotrichite forms on top of copiapite as thin hair-like salts during very dry times. This reaction is probably driven by the high Al:Fe ratios that develop in the evaporating solutions as iron sulfate minerals form.

We have found that the mineral transformations described here involve oxidation reactions, hydration/dehydration reactions, and acidification/neutralization reactions. Of these, the first two reaction types seem to be the most important in controlling the evolution of the mineralogy. The third process, acidification/neutralization is driven by the production and consumption of sulfuric acid. For example, oxidation of pyrrhotite creates sulfuric acid (eqn. 2), albeit less than the oxidation of pyrite (eqn. 1), and subsequently sulfuric acid concentrations increase as ferrous sulfate-sulfuric acid rich solution evaporate. Sulfuric acid is created or consumed in subsequent transformation of sulfate phases and is important in the stability of the phases so sulfuric acid is also an important component of this system.

Log a_{O_2} -log a_{H_2O} Diagram

One way to visualize the relationships of the phases that we found at the Iron Ridge site is with a $\log a_{O_2} - \log a_{H_2O}$ diagram (Fig. 12). This diagram shows the chemical relationships of the phases that were identified in the field. The axes of this diagram ($\log a_{O_2} - \log a_{H_2O}$) were chosen to represent the two dominant reaction types controlling the iron sulfate paragenesis, oxidation and hydration/dehydration.

The chemical reaction that corresponds to each line on the diagram is listed in Table 5. In some cases, the position of the line could be calculated from published literature data. These continuous lines are shown as heavy lines on the diagram. In other cases, thermodynamic properties of the phases are not known so that the exact location of the line on the diagram could not be ascertained. However, the slopes of the lines are controlled by the stoichiometry of the reaction and their position can be constrained using the field or laboratory observations made in

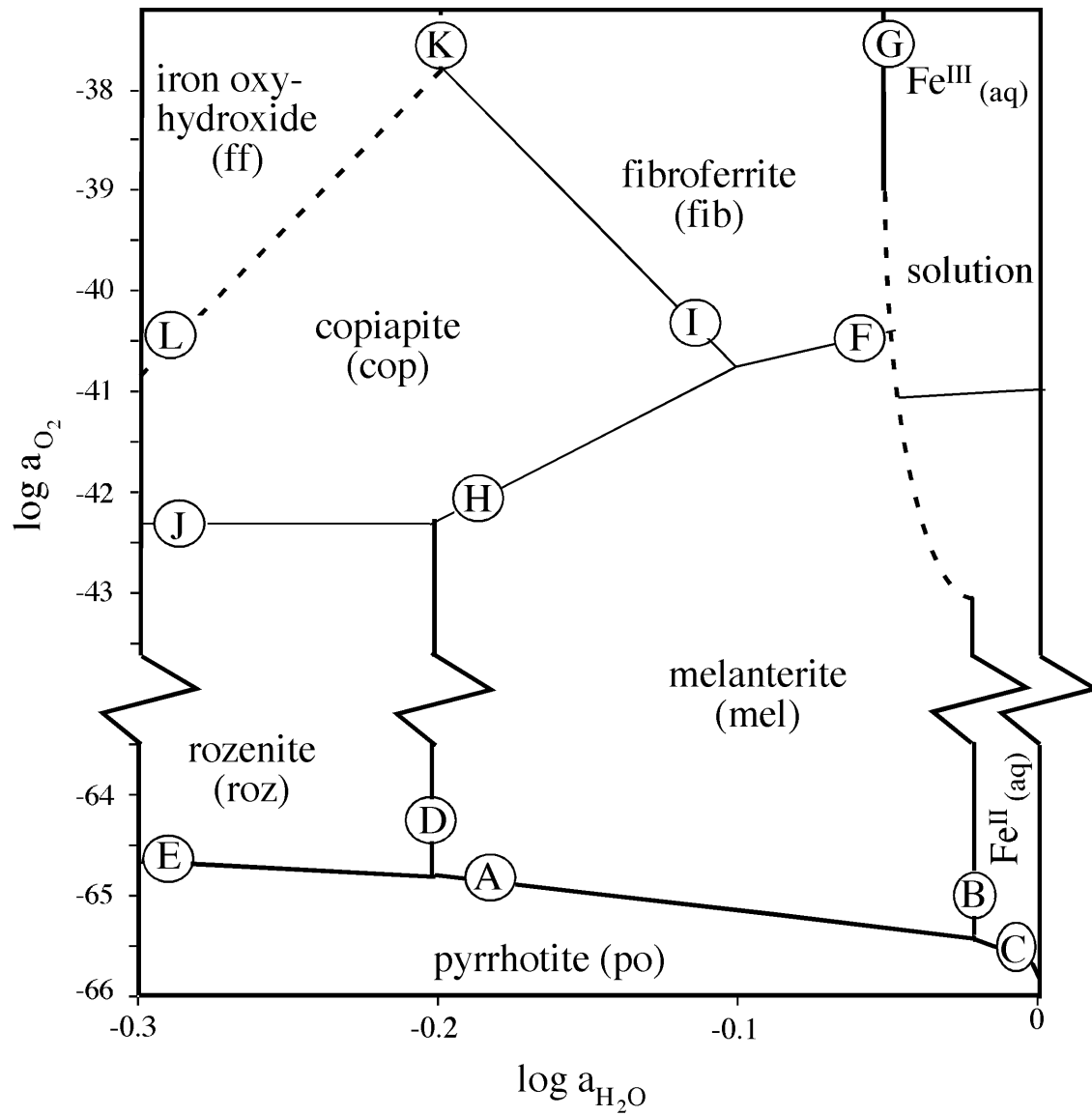


Figure 3-12. Log a_{O_2} -log a_{H_2O} diagram shows the relative stability of iron sulfide, sulfate, and oxyhydroxide phases. Numbered lines correspond to reactions in Table 5.

Table 3-5. Chemical reactions and equations used to construct the $\log a_{\text{O}_2} - \log a_{\text{H}_2\text{O}}$ (Fig. 12) and $\log a_{\text{H}_2\text{SO}_4} - \log a_{\text{H}_2\text{O}}$ (Fig. 13) diagrams. The slopes of all lines are shown in the equations and the intercepts are included when the equilibrium constant is known or can be calculated. The activity of sulfuric acid ($a_{\text{H}_2\text{SO}_4}$) on the $\log a_{\text{O}_2} - \log a_{\text{H}_2\text{O}}$ is 0. Phases that involve sulfuric acid are projections onto the $\log a_{\text{O}_2} - \log a_{\text{H}_2\text{O}}$ diagram from an unknown $a_{\text{H}_2\text{SO}_4}$. Changes in $a_{\text{H}_2\text{SO}_4}$ will change the position of the lines when it is a product or reactant but will not change the slope.

#	Balanced Reaction	Equation of Line
A	$\text{FeS (po)} + 2\text{O}_2 + 7\text{H}_2\text{O}$ $= \text{FeSO}_4 \cdot 7\text{H}_2\text{O (mel)}$	$\log a_{\text{O}_2} = \frac{-7}{2} \log a_{\text{H}_2\text{O}} - 65.5$
B	$\text{FeSO}_4 \cdot 7\text{H}_2\text{O (mel)}$ $= \text{Fe}^{2+} + \text{SO}_4^{2-} + 7\text{H}_2\text{O}$	$\log a_{\text{H}_2\text{O}} = -0.018$
C	$\text{FeS (po)} + 2\text{O}_2$ $= \text{Fe}^{2+} + \text{SO}_4^{2-}$	$\log a_{\text{O}_2} = -64.4 + 0.5 \log a_{\text{FeSO}_4}$
D	$\text{FeSO}_4 \cdot 7\text{H}_2\text{O (mel)}$ $= \text{FeSO}_4 \cdot 4\text{H}_2\text{O (roz)} + 3\text{H}_2\text{O}$	$\log a_{\text{H}_2\text{O}} = -0.666/3$
E	$\text{FeS} + 2\text{O}_2 + 4\text{H}_2\text{O}$ $= \text{FeSO}_4 \cdot 4\text{H}_2\text{O (roz)}$	$\log a_{\text{O}_2} = 2 \log a_{\text{H}_2\text{O}} - 65.18$
F	$\text{FeSO}_4 \cdot 7\text{H}_2\text{O (mel)} + 1/4\text{O}_2$ $= \text{Fe(OH)(SO}_4 \cdot 5\text{H}_2\text{O (fib)} + 3/2\text{H}_2\text{O}$	$\log a_{\text{O}_2} = 6 \log a_{\text{H}_2\text{O}} - 4 \log K$
G	$2\text{Fe(OH)(SO}_4 \cdot 5\text{H}_2\text{O (fib)} + 1/2\text{H}_2\text{SO}_4$ $= 2\text{Fe}^{3+} + 3\text{SO}_4^{2-} + 7\text{H}_2\text{O}$	$\log a_{\text{H}_2\text{O}} = -0.056$
H	$5\text{FeSO}_4 \cdot 7\text{H}_2\text{O (mel)} + \text{H}_2\text{SO}_4 + \text{O}_2$ $= \text{FeFe}_4(\text{SO}_4)_6(\text{OH})_2 \cdot 20\text{H}_2\text{O (cop)} + 15\text{H}_2\text{O}$	$\log a_{\text{O}_2} = 15 \log a_{\text{H}_2\text{O}} - \log K - \log a_{\text{H}_2\text{SO}_4}$
I	$\text{FeFe}_4(\text{SO}_4)_6(\text{OH})_2 \cdot 20\text{H}_2\text{O (cop)} + 1/4 \text{O}_2$ $+ 15/2 \text{H}_2\text{O} = 5\text{Fe(OH)(SO}_4 \cdot 5\text{H}_2\text{O (fib)} +$ H_2SO_4	$\log a_{\text{O}_2} = -30 \log a_{\text{H}_2\text{O}} - 4 \log K + 4 \log a_{\text{H}_2\text{SO}_4}$
J	$5\text{FeSO}_4 \cdot 4\text{H}_2\text{O (roz)} + \text{H}_2\text{SO}_4 + \text{O}_2$ $= \text{FeFe}_4(\text{SO}_4)_6(\text{OH})_2 \cdot 20\text{H}_2\text{O (cop)}$	$\log a_{\text{O}_2} = -\log K + \log a_{\text{H}_2\text{SO}_4}$
K	$\text{FeFe}_4(\text{SO}_4)_6(\text{OH})_2 \cdot 20\text{H}_2\text{O (cop)} + 1/4 \text{O}_2$ $= 5\text{Fe(OH)}_3 \text{ (ff)} + 6\text{H}_2\text{SO}_4 + 15/2\text{H}_2\text{O}$	$\log a_{\text{O}_2} = 30 \log a_{\text{H}_2\text{O}} - 4 \log K + 20 \log a_{\text{H}_2\text{SO}_4}$
L	$\text{FeSO}_4 \cdot 4\text{H}_2\text{O (roz)} + 1/4\text{O}_2$ $= \text{FeOOH (goe)} + \text{H}_2\text{SO}_4 + 5/2\text{H}_2\text{O}$	$\log a_{\text{O}_2} = 10 \log a_{\text{H}_2\text{O}} - 4 \log K$
M	$\text{FeS (po)} + \text{H}_2\text{SO}_4$ $= \text{FeS}_2 \text{ (py)} + 3/2\text{O}_2 + \text{H}_2\text{O}$	$\log a_{\text{H}_2\text{SO}_4} = \log a_{\text{H}_2\text{O}} + \frac{3}{2} \log a_{\text{O}_2} + 78.83$
N	$\text{FeS}_2 + 7/2\text{O}_2 + 8\text{H}_2\text{O}$ $= \text{FeSO}_4 \cdot 7\text{H}_2\text{O (mel)} + \text{H}_2\text{SO}_4$	$\log a_{\text{H}_2\text{SO}_4} = 8 \log a_{\text{H}_2\text{O}} + \frac{7}{2} \log a_{\text{O}_2} + 210.0$
O	$\text{FeS}_2 \text{ (py)} + 7/2\text{O}_2 + \text{H}_2\text{O}$ $= \text{FeSO}_4 + \text{H}_2\text{SO}_4$	$\log a_{\text{H}_2\text{SO}_4} = \log a_{\text{H}_2\text{O}} + \frac{7}{2} \log a_{\text{O}_2}$ $- 208.82 - \log a_{\text{FeSO}_4}$
P	$\text{FeS (po)} + 2\text{O}_2 + 7\text{H}_2\text{O}$ $= \text{FeSO}_4 \cdot 7\text{H}_2\text{O (mel)}$	$\log a_{\text{H}_2\text{O}} = -18.73 - \frac{2}{7} \log a_{\text{O}_2}$

this study. These lines are continuous but thin. Dashed lines are used for the reactions where the slopes are known but we have very poor constraints on the actual position of the line.

Line A: Pyrrhotite&Melanterite The equilibrium between pyrrhotite and melanterite was calculated using ΔG_f° for troilite, oxygen, liquid water, and melanterite published in Robie and Hemingway (1995). Stoichiometric iron sulfide (troilite) is the most reduced form of pyrrhotite. Using other free energies of formation for pyrrhotite would shift the line to a slightly higher a_{O_2} , although not noticeably at the scale of this diagram. The values of ΔG_f° melanterite vary slightly in the literature (DeKock (1982) $\Delta G_f^\circ = -2509.902$, Robie and Hemingway (1995) $\Delta G_f^\circ = -2509.5$, Wagman, et. al (-2509.87). We used the value from Robie and Hemingway for the sake of internal consistency.

Line B: Melanterite & Solution. The dissolution of melanterite is independent of a_{O_2} and therefore plots as a vertical line on the diagram. Melanterite has been shown to deliquesce at an $a_{H_2O} = 0.952$ (Linke, 1958) or $a_{H_2O} = 0.958$ (Apelblat, 1993). We used Apelblat's value in our calculations. The difference between these values is too small to be seen on our diagram. However, the activity of water at melanterite saturation was used in other calculations.

The equilibrium between melanterite and solution was used to determine the placement of other lines on the diagram. Many studies of melanterite solubility, summarized by Linke (1958), have shown that the ferrous sulfate solution becomes saturated with respect to melanterite at a concentration of 1.96 molal. Reardon and Beckie (1987) used Pitzer equations to revise the data of Oykova and Balarew (1974) and determine the osmotic coefficient (used to determine the activity of water) and mean activity coefficient of $FeSO_4$ for various ferrous sulfate solution (Table 6). At 25°C, the mean activity coefficient of ferrous sulfate at saturation is 0.048. We used this value to determine the a_{FeSO_4} at saturation, as described by Nordstrom and Munoz (p. 192, 1994) and combined with the updated value of a_{H_2O} at saturation to determine the equilibrium constant for reaction B:

$$K_B = \frac{a_{\text{Fe}} a_{\text{SO}_4} a_{\text{H}_2\text{O}}^7}{a_{\text{melanterite}}} = \frac{\left(m_{\pm_{\text{FeSO}_4}} \gamma_{\pm_{\text{FeSO}_4}}\right)^2 a_{\text{H}_2\text{O}}^7}{a_{\text{melanterite}}} = \frac{((1.96)(0.048))^2 (0.958)^7}{1} = 10^{-2.183} \quad (5)$$

Table 3-6. Osmotic and mean ionic activity coefficients for various concentrations of ferrous sulfate solutions. Activity coefficients are used to calculate activity of ferrous sulfate (line B) and the osmotic coefficients are used to calculate activity of water (line C) (Reardon and Beckie, 1987).

m_{FeSO_4}	ϕ	$\gamma_{\pm_{\text{FeSO}_4}}$
0.1	0.556	0.161
0.2	0.515	0.115
0.3	0.511	0.093
0.4	0.509	0.081
0.5	0.519	0.073
0.6	0.521	0.067
0.7	0.527	0.062
0.8	0.532	0.059
0.9	0.542	0.056
1.0	0.547	0.054
1.1	0.557	0.052
1.2	0.562	0.051
1.3	0.574	0.050
1.4	0.584	0.049
1.5	0.598	0.048
1.6	0.617	0.047
1.7	0.636	0.047
1.8	0.657	0.047
1.9	0.685	0.048
2.0	0.705	0.049

Line C: Pyrrhotite & Solution. The dissolution of pyrrhotite creates a ferrous sulfate solution and the activity of water decreases non-linearly as a function of the activity of the ferrous sulfate in solution, which is why the line is curved. The curve was calculated by first determining a_{O_2} where melanterite, pyrrhotite, and ferrous sulfate solutions coexist. To determine this value, the log equilibrium constants for the reactions for lines A and B were added together to determine the equilibrium constant for line C. Using this value ($\log K_c = -64.9$), the equilibrium expression was solved to determine the $\log a_{\text{O}_2}$ as a function of $\log a_{\text{FeSO}_4}$.

$$\log a_{\text{O}_2} = -64.4 + 0.5 \log a_{\text{FeSO}_4} \quad (6)$$

This reaction it is not represented by a horizontal line because the activity of water varies with the activity of ferrous sulfate in the solution. Using the activity coefficient of ferrous sulfate listed in Table 6, we calculated the activity of ferrous sulfate component in solution at various concentrations. Then, using the osmotic coefficient also listed in Table 6, we can calculate the activity of water using the following equation:

$$\log a_{\text{H}_2\text{O}} = \frac{-vmW_A}{2303} \Phi \quad (7)$$

where v is the number of ions in the electrolyte, m is the concentration of the ferrous iron solution (mol/kg solvent), W_A is the molecular weight of the solvent (18.0 g/mol for water) and ϕ is the osmotic coefficient (Robinson and Stokes, 1955). The above equations were simultaneously used to determine the a_{O_2} and $a_{\text{H}_2\text{O}}$ in equilibrium with ferrous iron solutions as the concentration decreased away from melanterite saturation. The results of these calculations are listed in Table 7.

Table 3-7. The activity of oxygen and activity of water at various activities of ferrous sulfate solution

log activity FeSO₄	log activity O₂	activity H₂O
-1.793	-64.5	0.998
-1.495	-64.7	0.993
-1.318	-65.1	0.985
-1.124	-65.4	0.976
-1.018	-65.4	0.965
-1.027	-65.4	0.952

Line D: Melanterite & Rozenite. This reaction is independent of a_{O_2} and therefore is a vertical line on the diagram. We have used a value of activity of water in equilibrium with

melanterite and rozenite, which is equal to 0.5998 based on the results reported by Chou et al. (2002).

Line E: Pyrrhotite & Rozenite. The equilibrium between rozenite and pyrrhotite was determined by adding the log equilibrium constants for reactions A and D.

Line F: Melanterite & Fibroferrite. The ΔG_f° of fibroferrite is unknown. Therefore, the equilibrium constant for this reaction cannot be determined. However, the slope of the line between these two phases is constrained by reaction stoichiometry to be 6.

In addition, we know that because fibroferrite contains only ferric iron and melanterite contains only ferrous iron, the melanterite/fibroferrite boundary must occur near a $\log a_{O_2}$ where the solution has nearly equal amounts of ferrous and ferric iron. We can calculate the equilibrium constant for the oxidation of ferrous to ferric iron in solution and plot a line on the diagram where the two activities of the two species are equal. This line, shown as a thin, sub-horizontal line in the solution field on the diagram, has a slope of one and is pH dependent. At a pH of 2.5, $\log a_{O_2}$ equals -42 . Therefore, we believe that this reaction occurs near $\log a_{O_2}$ of -42 as well.

Line G: Fibroferrite & Solution. Neither the ΔG_f° of fibroferrite nor the activity of the ferric iron in the saturated solution at equilibrium is known. So, we cannot calculate an equilibrium constant for this reaction. However, we can determine where the line is located on the diagram. As previously discussed, we determined that fibroferrite deliquesces at a relative humidity of 88% ($\log a_{H_2O}$ of -0.055). This reaction is independent of oxygen and therefore plots as a vertical line of the diagram.

Line H: Melanterite & Copiapite. The ΔG_f° of copiapite is unknown. However, we can calculate that the slope of the phase boundary between copiapite and melanterite is $+15$. In addition, we measured the equilibrium relative humidity of copiapite plus solution to be 80% ($\log a_{H_2O}$ of -0.1) using the humidity buffer method. Therefore, the copiapite field cannot lie to

the right of this line. Furthermore, copiapite, fibroferrite, and melanterite were observed to coexist in the field. Therefore, the triple point between these three phases was placed at $\log a_{\text{H}_2\text{O}}$ of -0.01 and a $\log a_{\text{O}_2}$ of -42.

Line I: Copiapite & Fibroferrite The ΔG_f° for these minerals are not known. However, they were observed to coexist at field area I, suggesting that copiapite can oxidize to fibroferrite under humid conditions. We can write a reaction (I) and calculate the slope of the line that describes this equilibrium. In addition, we can constrain the placement of this line on the diagram. Because we know that copiapite deliquesces at relative humidities higher than 80%, the line must fall to the left $a_{\text{H}_2\text{O}} = 0.8$. Also, we observed melanterite, copiapite, and fibroferrite coexisting in the field. As previously discussed (line H), copiapite probably forms around the $\log a_{\text{O}_2}$ where concentrations of ferrous and ferric iron are equal in solution. This constrains the triple point between melanterite, copiapite, and fibroferrite. The line between copiapite and fibroferrite will extend from this point with a slope of 6.

Line J: Copiapite & Rozenite. Without the free energy of formation of copiapite, this equilibrium constant cannot be calculated. However, the line representing the reaction between copiapite and rozenite can be constrained by other considerations. The $a_{\text{H}_2\text{O}}$ for melanterite and rozenite equilibrium has been carefully determined by Chou et. al (2002). We have already discussed the constraints on the line representing the reactions between melanterite and copiapite. By adding reaction D and H, we can calculate the slope of the line between copiapite and rozenite (0), which plots as a horizontal line that extends from the triple point between melanterite-rozenite-copiapite.

Line K: Fibroferrite and Iron Oxyhydroxide The iron oxyhydroxide phases found in the field were primarily amorphous. Therefore, we show the reaction between fibroferrite and ferrihydrite ($\text{Fe}(\text{OH})_3$). This reaction does not involve any oxidation and therefore is a vertical line on the diagram. However, we do not know the activity of water where this transformation

will take place, and therefore we cannot constrain the placement on the diagram. It is reasonable to assume that iron oxyhydroxide phases will eventually convert to goethite, the thermodynamically stable phase at $a_{\text{H}_2\text{O}}$ greater than 0.41 (Langmuir, 1997).

Line L: Copiapite and Iron Oxyhydroxide. Neither the activity of oxygen nor the activity of water at which copiapite oxidizes and dehydrates to iron oxyhydroxides is known. Therefore, it is very difficult to constrain the placement of this line. All we can presume is that it occurs at relatively high oxygen partial pressures and under low relative humidity.

Stability of other sulfate phases. The $\log a_{\text{O}_2} - \log a_{\text{H}_2\text{O}}$ diagram is constructed for the pure iron-sulfur system. Therefore, phases that contain other elements like Al (halotrichite) or K (jarosite) do not plot on the diagram. We know that these phases must exist as projections on to the diagram. We assume that halotrichite would occupy approximately the same field as melanterite, because they both contain ferrous iron and are fairly hydrous phases.

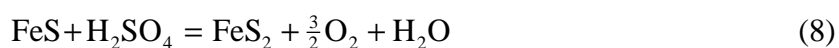
In addition, there is some evidence that other mixed valence iron phases may be present in the field. These probably project into the field that we have designated as copiapite. Copiapite is by far the most abundant mixed valence state phase found at our field site. Therefore, it is reasonable to conclude that it is stable over a range of $a_{\text{O}_2} - a_{\text{H}_2\text{O}}$ conditions. Other phases probably exist, but their stability fields will be much smaller. The copiapite field is projected from an unknown activity of sulfuric acid onto the $\log a_{\text{O}_2} - \log a_{\text{H}_2\text{O}}$ diagram.

Role of sulfuric acid. Sulfuric acid also plays an important role in the paragenesis of iron sulfate minerals. For example, the solubility of melanterite is reduced in H_2SO_4 solutions, and many of the reactions that form sulfate minerals that occur on the right hand side of Figure 1 involve consumption of sulfuric acid while the formation of iron oxyhydroxides produces sulfuric acid.

A good example of the role of sulfuric acid is its effect on the transformation of pyrrhotite to marcasite \pm pyrite to melanterite. Reflected light observations of partly oxidized

pyrrhotite show that an iron sulfide phase structurally similar to marcasite forms at the surface of the pyrrhotite grains (Blowes and Jambor, 1990). Craig and Vaughan (1994) describe this characteristic, fine-grained mixture of iron sulfide phases as a “birds-eye” texture. The “birds-eye” texture in the pyrrhotite grains collected from the Gossan Lead show that this process of forming iron disulfide by the partial oxidation of pyrrhotite occurs at our field site. Pyrrhotite, FeS₂, and melanterite coexist in these samples.

The oxidation of troilite to iron disulfide consumes sulfuric acid



Note that the ferrous sulfide phases are stable under reducing conditions when the partial pressure of oxygen is very low. The oxygen in equation 8 is present so that these phases can be described as a function of oxygen fugacity; we do not believe that this reaction will occur in nature. The oxidation of iron disulfide to melanterite produces sulfuric acid



Therefore, although the net reaction (reaction A) appears to be independent of sulfuric acid, it can also proceed step-wise as described by equations 8 and 9.

Figure 14 shows the stability of troilite, iron disulfide, melanterite, and solution as functions of the activity of sulfuric acid and the activity of water where the partial pressure of oxygen ranges from 10⁻⁶⁷ to 10⁻⁶³. The lines on the diagram correspond to the reactions listed in Table 5. Equilibrium constants were calculated from free energy data compiled by Robie and Hemingway (1995) except for the free energy of sulfuric acid. We used a 1.0 molal ideal solution for the reference state of sulfuric acid ($\Delta G_f^\circ = -744.53$) (Wagman et al., 1982). For reactions involving iron disulfide, we used the free energy of formation for marcasite because it is likely that the phase is composed primarily of marcasite. Using the free energy of formation of pyrite instead would cause an imperceptible increase the size of the FeS₂ field. The activity of water in a ferrous sulfate-sulfuric acid solution at melanterite saturation was calculated using the

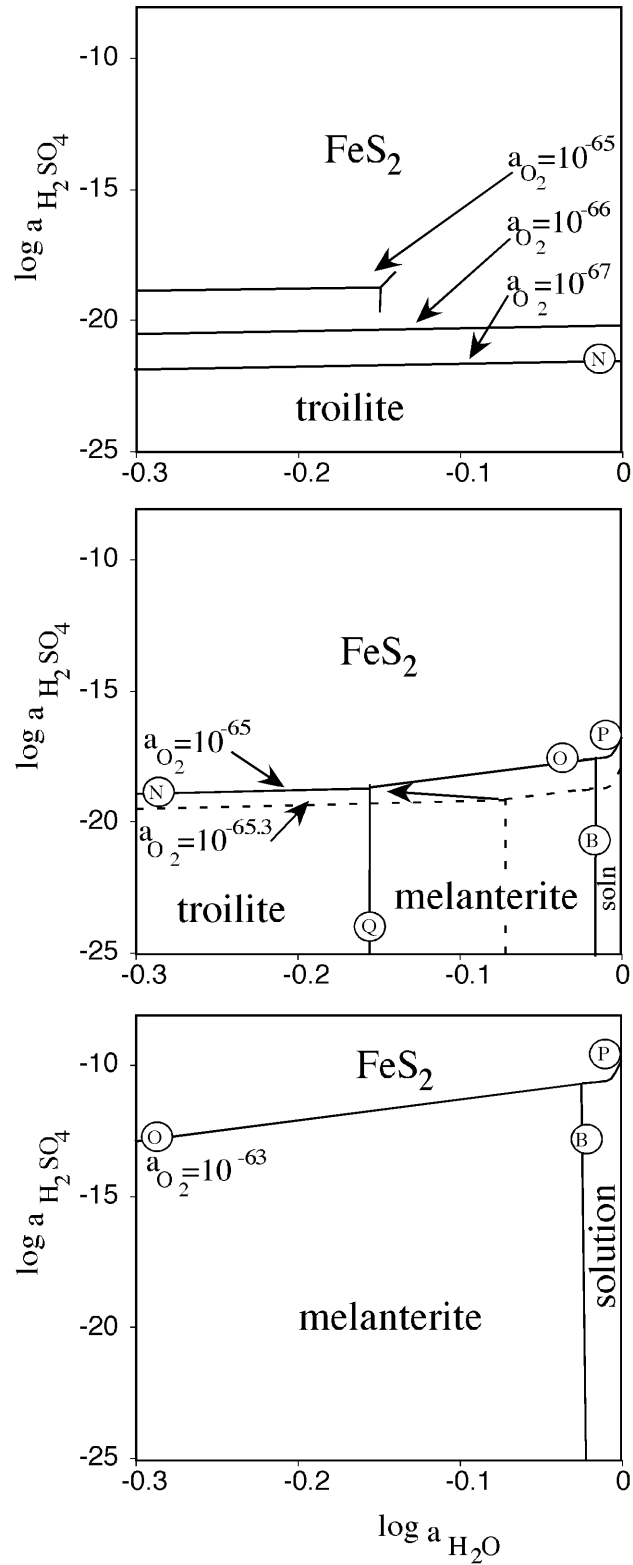
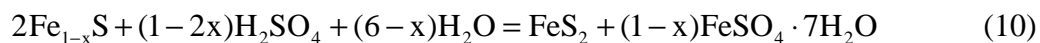


Figure 3-13. $\log a_{\text{H}_2\text{SO}_4}$ - $\log a_{\text{H}_2\text{O}}$ diagram shows the relative stability of troilite, marcasite, melanterite, and solution with increasing partial pressure of oxygen. The lines correspond to reactions in Table 5.

Pitzer method. The activity of H_2SO_4 is too low in these solutions to affect the $a_{\text{H}_2\text{O}}$. The activity of ferrous sulfate solution was calculated using the parameters in Table 6.

At very low oxygen partial pressures (10^{-67} - 10^{-65}), only troilite and iron disulfide are stable and no ferrous sulfate solution is present (Fig. 13a). When $\log a_{\text{O}_2}$ increases to -65 , the equilibrium between troilite and iron disulfide moves towards higher activities of sulfuric acid. When $\log a_{\text{O}_2} = -65.3$, the ferrous sulfate solution and melanterite fields begin to grow out of the troilite field (Fig. 13b). The equilibrium activity of water set by the troilite to melanterite reaction decreases with increasing $\log a_{\text{O}_2}$. This can also be seen on the $\log a_{\text{O}_2} - \log a_{\text{H}_2\text{O}}$ diagram (Fig. 12). With further increases of a_{O_2} , the triple point between troilite, iron disulfide, and melanterite moves up and to the left on Figure 13b. When the partial pressure of oxygen has risen to 10^{-63} , troilite is no longer present on the diagram and the equilibrium between melanterite and marcasite has risen to higher activities of sulfuric acid (Fig. 13c). Further increase in a_{O_2} will cause melanterite to grow at the expense of FeS_2 until the entire diagram consists of either melanterite or solution.

At the field site, we found pyrrhotite rather than troilite so the reaction that produces FeS_2 is slightly modified because $a_{\text{H}_2\text{SO}_4}$ is not set externally, but rather the H_2SO_4 comes from the oxidation of the pyrrhotite. When pyrrhotite oxidizes, some sulfuric acid is generated along with melanterite because there is excess sulfur relative to iron (eqn. 4). This sulfuric acid reacts with pyrrhotite to generate FeS_2 and melanterite (eqn. 10):



Oxidation of FeS_2 to melanterite also generates sulfuric acid for reaction 10. These reactions occur at the triple point between pyrrhotite, FeS_2 , and melanterite (Fig. 13b). With increasing a_{O_2} , this triple point migrates to lower $a_{\text{H}_2\text{O}}$ and higher $a_{\text{H}_2\text{SO}_4}$.

Sulfuric acid is also important for reactions involving ferric-bearing sulfate minerals on the $\log a_{\text{O}_2} - \log a_{\text{H}_2\text{O}}$ diagram. For example, the formation of copiapite from melanterite (reaction H, Table 5) consumed H_2SO_4 . Unfortunately, neither the free energy of formation of the minerals nor the thermodynamic properties of ferric sulfate-sulfuric acid solutions are known. A change in the activity of sulfuric acid will cause the stability fields of ferric-bearing sulfate minerals to change as well. The fields shown at high $\log a_{\text{O}_2}$ on the $\log a_{\text{O}_2} - \log a_{\text{H}_2\text{O}}$ diagram (Fig. 12) are estimated from our field observations. We know that some H_2SO_4 is present, so the stability field of copiapite is a projection onto the $\log a_{\text{O}_2} - \log a_{\text{H}_2\text{O}}$ surface from $a_{\text{H}_2\text{SO}_4} > 0$.

Field Reaction Path

We can combine our paragenesis observation (Figs. 11) with the $\log a_{\text{O}_2} - \log a_{\text{H}_2\text{O}}$ diagram (Fig. 12) to create a reaction path that explains our observations at the sites. At area I, reaction pathway moves from the pyrrhotite-melanterite-solution triple point, through the melanterite field, into the copiapite field near the triple point between melanterite-copiapite-fibroferrite, then into the fibroferrite field, and finally into the iron oxyhydroxide field. At area II, the reaction path moves from the pyrrhotite-melanterite-solution triple point, into the melanterite field, and then into the rozenite field, before moving into the copiapite field and finally into the iron oxyhydroxide field.

These paths reflect the differing field conditions, which control the rate of transformation of the minerals. For example, the relative humidity of area I is consistently high. Therefore, we expect that oxidation reactions proceed faster than dehydration reactions. By contrast, in the low relative humidity of area II, minerals dehydrate faster than they oxidize. Oxidation may proceed more rapidly in area II during rain events or times of higher ambient relative humidity.

Water Quality Effects

Results from the dissolution experiments show that all the sulfate mineral samples will release acid and trace metals upon dissolution. However, the impact of each phase is different. Phases bearing trivalent cations (fibroferrite, copiapite, halotrichite) release the most acid due to the extensive hydrolysis of ferric iron and/or aluminum. Ferrous iron also undergoes hydrolysis, but to a lesser extent so that melanterite solutions are less acidic. However, when aqueous ferrous iron oxidizes to ferric iron, further hydrolysis will occur. Therefore, ferrous iron bearing phases (melanterite, rozenite, copiapite, halotrichite), produce some immediate acidity and some latent acidity. The difference between the acid producing potential of sulfate minerals is most marked in very dilute solutions. In moderately concentrated solutions (>1 wt %), the pH of the leachate solutions was less than 3.0 for all minerals from the site.

All the field samples contained metals besides iron. The most abundant metals were magnesium, aluminum, zinc, copper, calcium, and lead. The molar concentrations of the metals varied with mineralogy. The melanterite-rich sample contained the least amount of substituted metals, although it did contain the most lead. Magnesium was the second most abundant metal after iron in the leachate of all the field samples except halotrichite. In the halotrichite-rich field sample, magnesium was the most important cation, followed by iron, then aluminum. Not surprisingly, halotrichite contained a high proportion of aluminum (23% of all metals on a molar basis). Our field samples probably lie within the solid solution between halotrichite and pickeringite, the magnesium end-member. Fibroferrite also contained a significant amount of aluminum (6 mol% of all metals). Halotrichite, copiapite, and fibroferrite contained between 1-3 mol% zinc and up to 1 mol% copper. All samples contained some measurable lead. Lead concentrations in the resulting solutions will depend on the water:rock ratio of the dissolution, but in these experiments where the ratio was approximately 20:1, they were up to 500 ppb. Of

the all iron phases, fibroferrite contained the lowest percentage of iron and therefore contained the most trace elements to make up for this iron deficiency.

The fibroferrite-rich sample released the most acid upon dissolution and contains the most substituted trace metals of the sulfate phases found at the field site. However, it has a slower dissolution rate than the other phases. The halotrichite-rich sample also released significant acid and the most aluminum upon dissolution and has a higher dissolution rate. These two phases have the highest potential to impact the quality of receiving waters at this site. Copiapite produces a lot of acid, but does not contain as many potentially toxic metals as the other two minerals. Melanterite produced the least amount of acid and contains the least amount of trace metals. Therefore, of the minerals at the site, melanterite appears to be the most benign. However, all of these minerals can release metals and acid when they dissolve and therefore represent significant environmental threats.

CONCLUSIONS

Descriptions of sulfate mineral assemblages and paragenesis in acid mine drainage environments have been mostly site specific. The methodology described in this paper provides a more generalized view of the paragenesis of sulfate minerals and allows us to understand the environmental conditions under which the various minerals are stable. Our findings allowed us to construct a $\log a_{\text{O}_2} - \log a_{\text{H}_2\text{O}}$ diagram that shows the relative stability of the minerals as a function of relative humidity and oxygen partial pressure and activity of H_2SO_4 . Because each of the iron sulfate minerals will have a different trace element load and will produce different amount of acidity upon dissolution, this knowledge of the stability and paragenesis of iron sulfate minerals provides key information about their role in environmental degradation.

ACKNOWLEDGEMENTS

We appreciate the help of Jane Hammarstrom and Nadine Piatak in the identification of the sulfate minerals. In addition, our interpretations were aided by discussions with Jane. We are also grateful for the assistance of Heather Shannon in the field, with the humidity cell experiments, and with the acid generation experiments. This manuscript benefited from the comments of James Craig, Patricia Dove, Lee Daniels, and Kirk Nordstrom. This project was funded by a grant from the NSF (EAR-0003364), the Waste Policy Institute at Virginia Tech, and the Graduate Student Association at Virginia Tech.

REFERENCES

- Alpers, C.N., Nordstrom, D.K., and Thompson, J.M. (1994) Seasonal Variations of Zn/Cu Ratios in Acid Mine Water from Iron Mountain, California. In C.N. Alpers, and D.W. Blowes, Eds. 204th National Meeting of the American Chemical Society, p. 324-344. American Chemical Society, Washington, DC, Washington DC.
- Apelblat, A. (1993) The vapour pressure of saturated aqueous solution of potassium bromide, ammonium sulfate, copper(II) sulfate, iron(II) sulfate, and manganese(II) dichloride, at temperatures from 283 K to 308 K. *Journal of Chemical Thermodynamics*, 25, 1513-1520.
- Bandy, M.C. (1938) Mineralogy of three sulphate deposits of northern Chile. *The American Mineralogist*, 23, 669-760.
- Bayless, E.R., and Olyphant, G.A. (1993) Acid-generating salts and their relationship to the chemistry of groundwater and storm runoff at an abandoned mine site in southeastern Indiana, USA. *Journal of Contaminant Hydrology*, 12, 313-328.
- Blowes, D.W., and Jambor, J.L. (1990) The pore-water geochemistry and the mineralogy of the vadoze zone of sulfide tailings, Waite-Amulet, Quebec, Canada. *Applied Geochemistry*, 5, 327-346.

- Bol'shakov, A.P., and Ptushko, L.I. (1971) Alteration products of melanterite from Nikitov mercury ore deposits. *International Geology Review*, 13(6), 849-854.
- Buurman, P. (1975) In vitro weathering products of pyrite. *Geol. Mijnbouw*, 54, 101-105.
- Chou, I.-M., Seal, R.R., and Hemingway, B.S. (2002) Determination of melanterite-rozenite and chalcantite-bonattite equilibria humidity measurements at 0.1 MPa. *American Mineralogist*, 87, 108-114.
- Craig, J.R. (1980) Stratiform sulfide mineralization in the central U.S. Appalachians. *Norges Geol. Undersøkelse*, no. 360, 57-84.
- Craig, J.R., and Vaughan, D.J. (1994) *Ore Microscopy and Ore Petrography*. 434 p. John Wiley & Sons, Inc., New York.
- Cravotta, C.A.I. (1994) Secondary Iron-Sulfate Minerals as Sources of Sulfate and Acidity. In C.N. Alpers, and D.W. Blowes, Eds. 204th National Meeting of the American Chemical Society, p. 345-364. American Chemical Society, Washington DC.
- Dagenhart, T.V. (1980) The acid mine drainage of Contrary Creek, Louisa County, Virginia: Factors causing variations in stream water chemistry. University of Virginia.
- Gair, J.E., and Slack, J.F. (1984) Deformation, Geochemistry, and Origin of Massive Sulfide Deposits, Gossan Lead District, Virginia. *Economic Geology*, 79, 1483-1520.
- Greenspan, L. (1977) Humidity Fixed Points of Binary Saturated Aqueous Solutions. *Journal of Research of the National Bureau of Standards-A. Physics and Chemistry*, 81A, 89-96.
- Henry, D.K., Craig, J.R., and Gilbert, M.C. (1979) Ore mineralogy of the Great Gossan Lead, Virginia. *Economic Geology*, 74, 645-656.
- Jambor, J.J., Nordstrom, D.K., and Alpers, C.N. (2000) Metal-sulfate Salts from Sulfide Mineral Oxidation. In C.N. Alpers, J.L. Jambor, and D.K. Nordstrom, Eds. *Sulfate Minerals: Crystallography, Geochemistry, and Environmental Significance*, 40, p. 303-350. Mineralogical Society of America and Geochemical Society, Washington, D.C.
- Jerz, J.K. (1998) Mechanisms of Acid and Metal Release from a Fluvial Tailings Deposit. *Geochemistry*, p. 133. Colorado School of Mines, Golden, Colorado.

- Keith, D.C., Runnells, D.D., Esposito, K.J., Chermak, J.A., Levy, D.B., Hannula, S.R., Watts, M., and Hall, L. (2001) Geochemical models of the impact of acidic groundwater and evaporative sulfate salts on Boulder Creek at Iron Mountain, California. *Applied Geochemistry*, 16, 947-961.
- Keith, D.C., Runnells, D.D., Esposito, K.J., Chermak, J.A., and Hannula, S.R. (1999) Efflorescent sulfate salts--Chemistry, mineralogy, and effects of ARD streams. The Sixth International Conference on Tailings and Mine Waste '99, p. 573-579. Balkema, Rotterdam, Fort Collins, CO.
- Langmuir, D. (1997) *Aqueous Environmental Geochemistry*. 600 p. Prentice Hall, Upper Saddle River, NJ.
- Linke, W.F. (1958) SO₄ Ferric Sulfate Fe₂(SO₄(SO₄)₃). *Solubilities: Inorganic and Metal-Organic Compounds*, 1, p. 1058-1064. D. Van Nostrand Company, Inc, Princeton.
- McKibben, M.A., and Barnes, H.L. (1986) Oxidation of pyrite in low temperature acidic solutions: rate laws and surface textures. *Geochimica et Cosmochimica Acta*, 50, 1509-1520.
- Nordstrom, D.K., and Alpers, C.N. (1999) Geochemistry of Acid Mine Waters. In G.S. Plumlee, and M.J. Logsdon, Eds. *The Environmental Geochemistry of Mineral Deposits*, 6A, p. 131-160. Society of Economic Geologists, Inc., Littleton, CO.
- Oykova, T.G., and Balarew, C. (1974) Thermodynamic study of magnesium sulfate-ferrosulfate-water system at 25°C. *Comptes Rendus de l'Academie Bulgare des Sciences*, 27, 1211-1214.
- Rankin, D.W., Espenshade, G.H., and Shaw, K.W. (1973) Stratigraphy and structure of the metamorphic belt in the northwestern North Carolina and southwestern Virginia: A study from the Blue Ridge across the Brevard zone to the Sauratown Mountains anticlinorium. *American Journal of Science*, 273-A, 1-40.
- Reardon, E.J., and , and Beckie, R.D. (1987) Modeling chemical equilibria of acid mine-drainage: The FeSO₄-H₂SO₄-H₂O system. *Geochimica et Cosmochimica Acta*, 51(9), 2355-2368.

- Robie, R.A., and Hemmingway, B.S. (1995) *Thermodynamic Properties of Minerals and Related Substances at 298.15 K and 1 Bar (10⁵ Pascals) Pressure and at Higher Temperatures*. U.S. Geological Survey, Washington D.C.
- Singer, P.C., and Stumm, W. (1970) Acidic mine drainage: The rate-determining step. *Science*, 163, 1121-123.
- Staten, W.T. (1976) A chemical study of the silicate minerals of the Gossan Lead and surrounding rocks in southwestern Virginia. *Geological Sciences*, p. 110. Virginia Polytechnic Institute and State University, Blacksburg. Virginia.
- Stewart, B.R., Daniels, W.L., Jackson, M.L. (1997) Evaluation of leachate quality from the co-disposal of coal fly ash and coal refuse. *Journal of Environmental Quality*, 26, 1417-1424.
- Stose, A.J., and Stose, G.W. (1957) *Geology and Mineral Resources of the Gossan Lead District and Adjacent Areas in Virginia*. Virginia Division of Mineral Resources, Charlottesville, Virginia.
- Wagman, D.D., Evans, W.H., Parker, V.B., Schumm, R.H., Halow, I., Bailey, S.M., Churney, K.L., and Nuttal, R.L. (1982) The NBS tables of chemical thermodynamic properties Selected values for inorganic and C₁ and C₂ organic substances in SI unites. *Journal of Physical and Chemical Reference Data*, 11(Supplement No. 2), 2-58.
- Williamson, M.A., and Rimstidt, J.D. (1994) The kinetics and electrochemical rate-determining step of aqueous pyrite oxidation. *Geochimica et Cosmochimica Acta*, 58, 5443-5454.
- Young, J.F. (1967) Humidity Control in the Laboratory Using Salt Solutions-A review. *Journal of Applied Chemistry*, 17, 241-245.
- Zodrow, E.L., Wiltshire, J., and McCandlish, K. (1979) Hydrated sulfates from Sydney Coalfield, Cape Breton Island, Nova Scotia. II. Pyrite and its alteration products. *Canadian Mineralogist*, 17, 63-70.

APPENDIX 3 DATA FROM THE DISSOLUTION EXPERIMENTS

Table A3-1. Acid generation potential data. The water:mineral ratios of the most concentrated solution (used in the first measurement) is shown below each mineral. Subsequent pH measurements were collected on 5:1 serial dilutions from the initial solution.

Fibroferrite (7.98 g :97 mL)		Melanterite (17.63 g :97 mL)		Halotrichite (5.07 g :90 mL)		Copiapite (3.91 g :90 mL)	
wt % in soln	pH	wt % in soln	pH	wt % in soln	pH	wt % in soln	pH
1.79	1.88	3.64	2.38	5.63	2.42	4.34	2.46
3.59 x10 ⁻⁰¹	1.97	7.27 x10 ⁻⁰¹	2.74	1.13	2.52	8.69 x10 ⁻⁰¹	2.49
7.17 x10 ⁻⁰²	1.97	1.45 x10 ⁻⁰¹	2.95	2.25 x10 ⁻⁰¹	2.52	1.74 x10 ⁻⁰¹	2.51
1.43 x10 ⁻⁰²	2.01	2.91 x10 ⁻⁰²	3.64	4.51 x10 ⁻⁰²	2.65	3.48 x10 ⁻⁰²	2.7
2.87 x10 ⁻⁰³	2.12	5.82 x10 ⁻⁰³	4.34	9.01 x10 ⁻⁰³	2.91	6.95 x10 ⁻⁰³	2.97
5.74 x10 ⁻⁰⁴	2.41	1.16 x10 ⁻⁰³	5.28	1.80 x10 ⁻⁰³	3.22	1.39 x10 ⁻⁰³	3.28
1.15 x10 ⁻⁰⁴	2.96	2.33 x10 ⁻⁰⁴	5.91	3.61 x10 ⁻⁰⁴	3.7	2.78 x10 ⁻⁰⁴	3.64
2.30 x10 ⁻⁰⁵	3.49	4.65 x10 ⁻⁰⁵	6.07	7.21 x10 ⁻⁰⁵	4.11	5.56 x10 ⁻⁰⁵	3.95
4.59 x10 ⁻⁰⁶	3.75	9.31 x10 ⁻⁰⁶	6.19	1.44 x10 ⁻⁰⁵	4.47	1.11 x10 ⁻⁰⁵	4.11
9.18 x10 ⁻⁰⁷	3.85	1.86 x10 ⁻⁰⁶	6.26	2.88 x10 ⁻⁰⁶	4.72	2.22 x10 ⁻⁰⁶	4.38
1.84 x10 ⁻⁰⁷	4.06			5.77 x10 ⁻⁰⁷	4.63	4.45 x10 ⁻⁰⁷	4.46

Table A3-2. Elemental concentrations from the ICP. The water:mineral ratio of the solute for each sample is shown below the mineral. The atomic emission of each element was measured at the wavelength shown in the second column. All concentrations are in units of mg/kg.

	λ nm	Melanterite (0.41 g: 100 mL)	Fibroferrite (0.49 g: 100 mL)	Halotrichite (0.44 g: 100 mL)	Copaipite (0.59 g: 100 mL)
Na	589.592	0.562	0.3248	0.542	0.4812
Mg	279.079	32.18	57.3	158	37.01
Si	288.158	0.97	0.0507	0.3348	0.0741
P	178.29	0.671	0.768	0.1463	0.1192
S	180.734	733	718	676	857
K	766.491	1.862	0.0238	0.2484	1.203
Ca	317.933	2.514	3.092	13.79	2.566
Cr	267.716	0.0276	0.0321	0.0275	0.0267
Mn	257.61	1.994	4.015	17.02	3.591
Fe	259.94	1,189	790	290	1,367
Co	228.616	0.698	1.073	1.261	1.791
Ni	352.454	0.0985	0.1217	0.689	0.2477
Cu	324.754	2.855	10.94	7.86	10.97
Zn	213.856	10.39	15.34	33.08	30.59
Al	167.08	18.08	45.03	149	21.81
Cd	228.802	0.0302	0.0423	0.0792	0.0817
Pb	220.353	1.067	0.2784	0.3128	0.4484